Peroxisomal calcium handling and homeostasis

Dissertation

for the award of the degree

Doctor rerum naturalium

of the Georg-August-Universität Göttingen

within the doctoral program Molecular Medicine

of the Georg-August University School of Science (GAUSS)

submitted by

Yelena Sargsyan

from Yerevan, Armenia

Göttingen, 2022

Thesis committee / examination board

Prof. Dr. Sven Thoms

Department for Child and Adolescent Medicine
University Medical Center Göttingen

Department of Biochemistry and Molecular Medicine
Medical School, Bielefeld University

Prof. Dr. Silvio Rizzoli

Department of Neuro- and Sensory Physiology
University Medical Center Göttingen

PD Dr. Laura Zelarayan

Institute of Pharmacology and Toxicology
University Medical Center Göttingen

Prof. Dr. Katrin Streckfuß-Bömeke

Clinic for Cardiology and Pneumology
University Medical Center Göttingen

Institute of Pharmacology and Toxicology
Würzburg University

Prof. Dr. Thomas Meyer

Department of Psychosomatic Medicine and Psychotherapy
University Medical Center Göttingen

Prof. Dr. Michael Müller

Department of Neuro- and Sensory Physiology
University Medical Center Göttingen

Table of content

List of abbreviations

ACBD5	Acyl-CoA binding domain containing 5
ACAA1	Thiolase, or acetyl-CoA acyltransferase 1
Caf	Caffeine
CaM	Calmodulin
Cav3	Caveolin 3
CM	Cardiomyocyte
EDTA	Ethylenediaminetetraacetic acid
EGFP	Enhanced green fluorescent protein
EGTA	Ethylene glycol-bis(β-aminoethyl ether)-N,N,N',N'-tetraacetic acid
ER	Endoplasmic reticulum
FRET	Förster resonance energy transfer
GECI	Genetically encoded calcium indicators
HF	Heart failure
hiPSC	Human induced pluripotent stem cells
His	Histamine
IMM	Inner mitochondrial membrane
IP_3	Inositol 1,4,5-trisphosphate
IP_3R	IP_3 receptor
K_d	Dissociation constant
LDH	Lactate dehydrogenase
LTCC	L-type Ca^{2+} channel
LUT	Look-up table
MAMs	Mitochondria-ER associated membranes
MCS	Membrane contact sites
MCT	Monocarboxylate transporter
MCU	Mitochondrial calcium uniporter
MSP	Major sperm protein
NRCM	Neonatal rat cardiomyocytes

o.n.	Overnight
PBD	Peroxisome biogenesis disorders
PBS	Phosphate-buffered saline
PFA	Paraformaldehyde
PIP_2	phosphatidylinositol 4,5-bisphosphate
PLC	Phospholipase C
PM	Plasma membrane
PMCA	Plasma membrane calcium ATPase
PMP	Peroxisomal membrane protein
PTS	Peroxisomal targeting signal/sequence
ROI	Region of interest
ROS	Reactive oxygen species
RT	Room temperature
Ry	Ryanodine
RyR	Ryanodine receptor
SDS	Sodium dodecyl sulfate
SEM	Standard error of the mean
SERCA	Sarco/endoplasmic reticulum Ca^{2+}-ATPase
SOCE	Store operated calcium entry
SR	Sarcoplasmic reticulum
STED	Stimulated emission depletion (microscopy)
STIM1	Stromal interacting molecule 1
TCA	Tricarboxylic acid
Tg	Thapsigargin
VAPA, VAPB	Vesicle-associated membrane protein -associated proteins A and B
VDAC	Voltage-dependent anion channel
VLCFA	Very long chain fatty acids
ZS	Zellweger syndrome
ZSS	Zellweger syndrome spectrum

List of figures

List of tables

Symbols and units

α	Alpha
β	Beta
%	Percent
°C	Degree Celsius
c	Centi (10^{-2})
g	Gram
h	Hour
k	Kilo (10^{3})
b	Base
l (or L)	Liter
m	Milli (10^{-3})
µ	Micro (10^{-6})
M	Molar (mol/L)
min	Minute
n	Nano (10^{-9})
rpm	Revolutions per minute
sec	Second
V	Volt
vg	Viral genome

Abstract

Peroxisomes are ubiquitous cellular organelles in eukaryotes essential for metabolism. The close localization of peroxisomes with the sarcoplasmic reticulum and T-tubules is known from electron micrographs of rodent hearts. This association of peroxisomes with sites of excitation-contraction coupling suggests a peroxisomal role in calcium handling. However, there is little known about peroxisomal calcium and previous studies brought up extensive contradictions.

This work addresses peroxisomal Ca^{2+} handling in non-excitable HeLa cells, and in excitable cells represented by cardiomyocytes.

Using both models, it is demonstrated that peroxisomal Ca^{2+} rises in dependance of cytosolic Ca^{2+} from a steady state of 600 nM to 2.4 µM. It is also shown that over 80% of peroxisomes in cardiomyocytes are in contact with ryanodine receptors and that cardiac peroxisomes take up Ca^{2+} when intracellular Ca^{2+} stores are depleted. These results suggest that peroxisomes in cardiomyocytes may contribute to an effective excitation-contraction process. Further, we studied the mechanisms of Ca^{2+} entry to peroxisomes.

Taken together, this work provides the first evidence of peroxisomal Ca^{2+} handling taking place in cardiomyocytes and that several mechanisms to interact with it exist. Modulation of peroxisomal Ca^{2+} homeostasis may have future clinical application in cases of impaired cellular Ca^{2+} handling, such as certain types of arrhythmias.

1. Introduction

1.1 Peroxisomes

Peroxisomes are single membrane-bound organelles originally identified as sites for production and degradation of hydrogen peroxide, and fatty acid metabolism (Titorenko and Rachubinski, 2001). β-Oxidation of fatty acids in yeast is exclusively a peroxisomal process, whereas in mammals it occurs in both, peroxisomes and mitochondria (Waterham et al., 2016). Very long chain fatty acids (VLCFA) are solely processed in peroxisomes (Reddy and Hashimoto, 2001), but mammalian peroxisomes can only shorten fatty acid chains providing intermediates for further mitochondrial β-oxidation (Reddy and Hashimoto, 2001). Peroxisomes and mitochondria share the same principle of fatty acid chain shortening through the sequence of dehydrogenation, hydration, dehydrogenation, and thiolytic cleavage reactions (Waterham et al., 2016). Peroxisomal fatty acid β-oxidation requires three enzymes: acyl-CoA oxidase (ACOX) for the first dehydrogenation step, a bifunctional enzyme for hydration and dehydrogenation, and acetyl-Coenzyme A acyltransferase 1 (ACAA1 or thiolase) for thiolytic cleavage (Reddy and Hashimoto, 2001). The $FADH_2$ produced in the first reaction is directed to the electron transport chain in mitochondria, whereas in peroxisomes it reacts with O_2 producing H_2O_2 (Waterham et al., 2016). H_2O_2 is then degraded by peroxisomal catalase into H_2O and O_2.

Peroxisomes are ~100 nm in diameter (Soliman et al., 2018). For their surprisingly small size, they contain over 130 proteins participating in a large variety of metabolic pathways far beyond fatty acid and hydrogen peroxide metabolism (Karnati and Baumgart-Vogt, 2008). They play crucial roles in ether lipid and bile acid biosynthesis, the metabolism of D-amino acids and of reactive oxygen species (ROS), degradation of purines, polyamines and L-pipecolic acid in mammals (Wanders and Waterham, 2006; Sargsyan and Thoms, 2020). Virtually all peroxisomal metabolic pathways require intimate communication of peroxisomes with other organelles (Sargsyan and Thoms, 2020).

1.2 Zellweger syndrome spectrum disorders

Partial or complete defects of peroxisome biogenesis due to mutations affecting *PEX* genes result in pathological conditions termed peroxisome biogenesis disorders (PBD)

(Steinberg et al., 1993). PBD are divided into two subtypes: the Zellweger syndrome spectrum (ZSS) and the rhizomelic chondrodysplasia punctate. ZSS is a group of rare, genetic multisystem diseases that can present with a range of mild and severe symptoms (Klouwer et al., 2015). Neurological deficits, hypotonia, hepatic dysfunction, hearing loss and impaired vision are common occurrences (Braverman et al., 2016). For the diagnosis of ZSS, clinical, biochemical and genetic confirmation of biallelic pathogenic variant of one of 13 ZSS-associated *PEX* genes is required (Steinberg et al., 1993).

The treatment of PBD is supportive and includes symptomatic measures such as nutritional support, application of hearing aids, surgical ophthalmologic interventions, and treatment of seizures (Braverman et al., 2016). A diet low in phytanic acid, oral bile acid and plasmalogen supplementation among other experimental therapies are sometimes applied (Braverman et al., 2016).

1.3 Zellweger syndrome

Zellweger syndrome (ZS) is the most severe form of ZSS with an onset and presentation in the newborn period and a lethal outcome within the first year of life (Steinberg et al., 2006). 2% of ZS cases are linked to pathogenic gene variants of *PEX5* (Ebberink et al., 2011). The PEX5 protein recognizes C-terminal peroxisomal targeting signal 1 (PTS1) of cargo proteins and mediates the PTS1-dependent protein import into the peroxisomal matrix (Fransen et al., 1995). Inactivation of ZS-causative *PEX* genes in mice results in impaired brain development without other major phenotypic changes known from human patients (Baes and Van Veldhoven, 2006). Both, patient- and *PEX5* knockout mice-derived fibroblasts show peroxisomal remnants known as peroxisomal ghosts (Santos et al., 1988; Baes et al., 1997). Peroxisomal ghosts are “empty” membrane structures with peroxisomal membrane proteins but devoid of peroxisomal matrix proteins and are larger in size than peroxisomes (Santos et al., 1988).

Yet not all mutations in *PEX* genes result in a complete absence of peroxisomal protein import. PEX2, PEX10 and PEX12 are zinc-binding RING (“really interesting new gene”) domain-containing peroxins involved in PEX5 (mono-)ubiquitination. In this manner, they regulate the peroxisomal protein import through PEX5 receptor (Platta et al., 2016). The mutation in the membrane-spanning segments of PEX2 results in complete absence of

catalase-positive peroxisomes, mutations in the RING-finger structure, however, in mosaicism with peroxisomal ghosts in some cells and catalase-positive peroxisomes in the others (Shimozawa et al., 2000). The inhomogeneity in the cellular and clinical presentation is also described in *PEX10* patients. In severe ZS cases, patient fibroblasts contain only non-functional peroxisome ghosts (Warren et al., 1998). Whereas the patients with later onset of cerebellar ataxia and higher life expectancy show cellular mosaicism (Régal et al., 2010; Yamashita et al., 2017).

1.4 Peroxisomal pore-forming proteins

PEX11 protein family is involved in peroxisome proliferation, peroxisome size regulation and growth (Thoms and Erdmann, 2005). Patient with pathogenic variant of *PEX11β* presents with mild PBD phenotype (Ebberink et al., 2012). In yeast, Pex11 is reported to form a membrane channel with an estimated size of 0.6 nm (Mindthoff et al., 2016). It is a non-selective channel for solutes with molecular weight lower than 300-400 Da (Mindthoff et al., 2016). Highly conserved protein sequence of PEX11 between yeast and human suggests that PEX11 may be a pore-forming protein also in human peroxisomes (Chornyi et al., 2021).

PXMP2 is reported to be an unspecific peroxisomal channel-forming protein with permeability to organic solutes smaller than 300 Da in *in vitro* experiments on artificial membranes (Rokka et al., 2009). It has a week cation selectivity and an estimated pore diameter of 1.4 nm (Rokka et al., 2009). PXMP2 knock-out female mice have reduced ductal system in the mammary gland, with otherwise normal phenotype (Vapola et al., 2014).

For both, Pex11 and PXMP2 the channel-forming function was identified and characterized by multiple channel recordings and single channel analysis using artificial lipid bilayer systems with recombinant proteins inserted (Rokka et al., 2009; Mindthoff et al., 2016). The electrolyte composition of buffers during these measurements is different from the physiological intracellular situation. The only *in vivo* study on PXMP2 and PEX11 as channels examined their role on hydrogen peroxide transport across peroxisomal membrane (Lismont et al., 2019). Judging from the molecular weight of the hydrogen peroxide it could freely pass both through the PXMP2 and PEX11. Nonetheless, using a

fluorescent biosensor for H_2O_2 in PXMP2- and/or PEX11- deficient cells, neither PXMP2 nor PEX11 were identified as essential for H_2O_2 trafficking across the peroxisomal membrane (Lismont et al., 2019). Moreover, as the peroxisome permeability to D-alanine is a prerequisite for H_2O_2 production in the experimental setup, PXMP2 and PEX11 are also not essential for D-alanine import to peroxisomes (Lismont et al., 2019).

1.5 Protein transport to peroxisomes

Peroxisomes possess dedicated machineries for import of matrix proteins and insertion of membrane proteins (Kim and Hettema, 2015). Most of peroxisomal matrix proteins are targeted to peroxisomes through their C-terminal localized peroxisomal targeting signal 1 (PTS1). The PTS1 is recognized by the receptor Pex5, which mediates the PTS1-dependent protein import into the peroxisomal matrix (Fransen et al., 1995). Some matrix proteins possess PTS2 located in their N-terminus. PEX7 is the receptor for PTS2-bearing proteins (Rehling et al., 1996).

Peroxisomal membrane proteins (PMPs) reach peroxisomes either directly or through the ER (Kim and Hettema, 2015). The direct targeting is mediated through PEX19 which is a receptor for freshly synthesized PMPs (Sacksteder et al., 2000). The indirect targeting of PMPs to peroxisomes through the endoplasmic reticulum (ER) is linked to the *de novo* formation of peroxisomes from the ER (Hoepfner et al., 2005; Kim et al., 2006; Aranovich et al., 2014).

1.6 Calcium homeostasis

Calcium is an intracellular messenger that plays an essential role in a variety of cellular processes ranging from early embryonic events to muscle contraction and neuron excitability (Berridge et al., 2000). The main sites of calcium entry to the cell and intracellular calcium signal regulation are plasma membrane (PM) and ER as the major intracellular calcium store. Upon stimulation of G-protein coupled receptors on the cell surface, phospholipase C (PLC) cascade activation results in hydrolysis of phospholipid phosphatidylinositol 4,5-bisphosphate (PIP_2) into inositol 1,4,5-trisphosphate (IP_3) and diacylglycerol. IP_3 binds the IP_3 receptor (IP_3R) on the ER membrane, triggering calcium store release through IP_3R channel (*Figure 1*).

ER calcium is released either into the cytosol, or through specialized compartments and membrane contact sites to the juxtaposed organelles (Paupe and Prudent, 2018). This initiates the store operated calcium entry (SOCE) to the non-excitable cells.

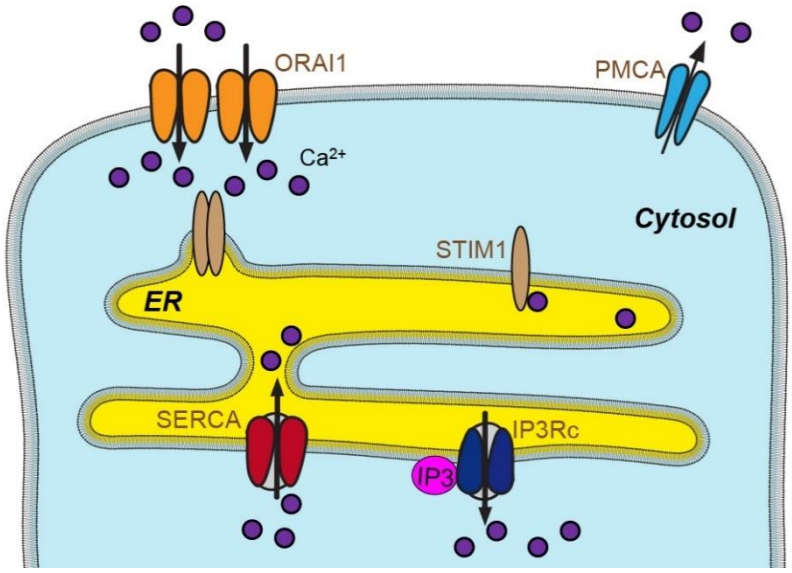

Figure 1. Store-operated calcium entry in non-excitable cells. IP3 binds the IP3 receptor (IP3R) on the ER membrane, triggering Ca^{2+} release from the ER. Upon decrease in Ca^{2+} concentration in ER, Ca^{2+} dissociates from STIM1 molecule enabling its oligomerization and localization to ER-PM interface. Here, it activates ORAI1 channels for Ca^{2+} import.

When ER Ca^{2+} concentration falls, Ca^{2+} dissociates form the ER-resident Stromal interacting molecule 1 (STIM1) allowing its oligomerization and relocalization at ER-PM contact sites. Here, STIM1 activates ORAI1 channels that are the main Ca^{2+} entry channels on the PM in non-excitable cells. At the same time, cytosolic calcium is constantly pumped back to the ER through sarco/endoplasmic reticulum Ca^{2+}-ATPase (SERCA) or exits the cell by the plasma membrane calcium ATPase (PMCA) (Raffaello et al., 2016).

1.7 Calcium signaling in cardiomyocytes

Cell depolarization is the main stimulus for the initiation of Ca^{2+} signaling in cardiomyocytes (CMs). In the plateau phase of the action potential voltage-gated L-type Ca^{2+} channels (LTCC, $Ca_v1.2$) in T-tubules open (Chapman, 1979; Bootman et al., 2002)

and small amounts of Ca^{2+} enter the cell, activating ryanodine receptors (RyR) on the sarcoplasmic reticulum (SR) membrane. The activation of RyR releases Ca^{2+} from the stores (Clapham, 2007). This is known as Ca^{2+}-induced Ca^{2+} release that initiates cardiac muscle contraction. The transfer of electrical events on the plasma membrane (action potential) to muscle contraction is known as excitation-contraction coupling (Sandow, 1952). During relaxation of the heart muscle, SERCA and NCX (sodium-calcium exchanger) pump Ca^{2+} back to the ER and extrude it out of the cell, respectively (Clapham, 2007). LTCC interact with caveolin-3 (Cav3) (Balijepalli et al., 2006). Caveolins are core structure proteins of caveolae that are cholesterol- and sphingolipid-rich plasma membrane pits (Parton, 2018). In mouse ventricular cardiomyocytes Cav3 is essential for normal organization of T-tubules and effective excitation-contraction process (Bryant et al., 2018). Mutations of LTCC (Kamp and Hell, 2000), RyR (Thomas et al., 2006), SERCA (Bachar-Wikstrom et al., 2020) and CAV3 (Vatta et al., 2006; Catteruccia et al., 2009) in humans are implicated in various cardiac diseases.

1.8 Peroxisomes and the heart

Heart function is fine-tuned by the energy it can synthetize through mitochondrial oxidation and the constant work it performs to meet the blood supply demands of its own and the whole body (Brown et al., 2017). Due to its constant work, the heart does not have energy storage capacity (Ventura-Clapier et al., 2004). Though being metabolic omnivore and being able to utilize all classes of metabolic substrates, the preference for one or the other substrate is highly dependent on the developmental stage and the health status of the organism (Ventura-Clapier et al., 2004; Huss and Kelly, 2005). Glycolysis is the main energy source of the fetal heart, but the adult heart relies preferentially on fatty acid β-oxidation (Huss and Kelly, 2005). A metabolic shift from fatty acid utilization back to carbohydrate consumption is observed in hypertrophied and failing myocardium (Huss and Kelly, 2005).

On the other side, fatty acid accumulation in the myocardium itself is often associated with heart failure and linked to mitochondrial dysfunction, uncoupling of mitochondrial respiration, increase of reactive oxygen species (ROS) production as well as oxidative stress (Colasante et al., 2015).

Patients with milder forms of ZSS present with cardiac arrhythmias, cardiomyopathy and heart failure resulting in death (Wanders and Komen, 2007). It can be assumed that heart is also affected in other forms of ZSS. Yet, the cardiac phenotype in those cases is masked by the severe and preceding neurological and developmental impairment of the affected patients (Colasante et al., 2015). One of the reasons of cardiac dysfunction can be the metabolic incompetence of peroxisomes, resulting in accumulation of phytanic acid, which in turn results in oxidative stress (Grings et al., 2012; Colasante et al., 2015). At the same time, the absence of functional peroxisomes in mice with global *PEX5* knockout results in abnormal mitochondrial respiratory complex I activity and severely affects mitochondrial morphology in the heart, suggesting that normal functional peroxisomes are a prerequisite of adequate mitochondrial function and redox equilibrium in the heart (Baumgart et al., 2001).

The cardiotoxic anti-cancer drug, dual tyrosine kinase inhibitor lapatinib results in decrease of many peroxisomal membrane proteins and enzymes in the induced pluripotent stem cell derived CMs, which in turn induces the metabolic shift towards glycolysis (Wang et al., 2019), further emphasizing the role of peroxisomes in the adult heart well-being.

The exact mechanisms and pathways of the interrelation of peroxisome-mitochondria and peroxisome-heart function still remain elusive.

1.9 Peroxisomes and calcium

In electron micrographs from rodent hearts peroxisomes are in immediate vicinity of T-tubules and with junctional SR (Hicks and Fahimi, 1977) (*Figure 2*). T-tubule and SR interaction sites are the main determinants of excitation-contraction coupling and effective Ca^{2+} handling in the CMs. The localization of peroxisomes at these sites gives the first hint that peroxisomes may take up Ca^{2+} and be part of Ca^{2+} homeostasis in CMs.

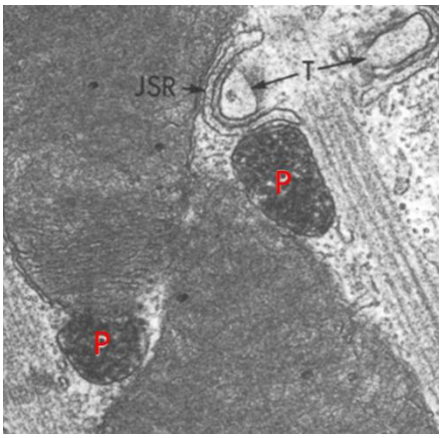

Figure 2. Peroxisomes (P) in the rodent hearts are associated with T-tubules (T) and junctional SR (JSR). Modified from Hicks and Fahimi (1977).

Two articles published back to back have analyzed peroxisomal Ca^{2+} in non-excitable cells. Drago et al. (2008) found peroxisomal Ca^{2+} concentration to be similar to cytosolic Ca^{2+} concentration. The authors also state that peroxisomal Ca^{2+} rises slowly when cytosolic Ca^{2+} is rising. In contrast, Lasorsa et al. (2008) report peroxisomal Ca^{2+} being 20 folds higher than cytosolic levels and a rapid increase up to 100 µM upon stimulation.

1.10 Membrane contact sites

Membrane contact sites (MCS) are defined as the functional, tethered proximity (usually ranging from 10 to 80 nm) between two membrane bound organelles (Scorrano et al., 2019). MCS have a defined proteome or lipidome composition, which is required for their functional and structural integrity (Scorrano et al., 2019). MCS enhance the communication between organelles by facilitating metabolite, substrate or signal exchange between them (Sargsyan and Thoms, 2020).

1.11 ER-peroxisome contact sites

The net-like structure of the ER that expands throughout the cell is the basis of the organelle interactome (Valm et al., 2017). The first identified MCS were ER-mitochondria contacts. ER-mitochondria contact sites are also called mitochondria-associated membranes (MAMs) (Vance, 2014). MAMs play an essential role in cell survival, functional integrity of mitochondria and substrate trafficking between ER and mitochondria (Vance, 2014).

ER-resident vesicle-associated membrane protein (VAMP)-associated proteins A and B (VAPA and VAPB) are components of many types of ER MCS (Loewen et al., 2003; Phillips and Voeltz, 2016). Their major sperm protein (MSP) domain interacts with FFAT (two phenylalanines (FF) in an acidic tract) and FFAT-like motif containing proteins (Loewen et al., 2003).

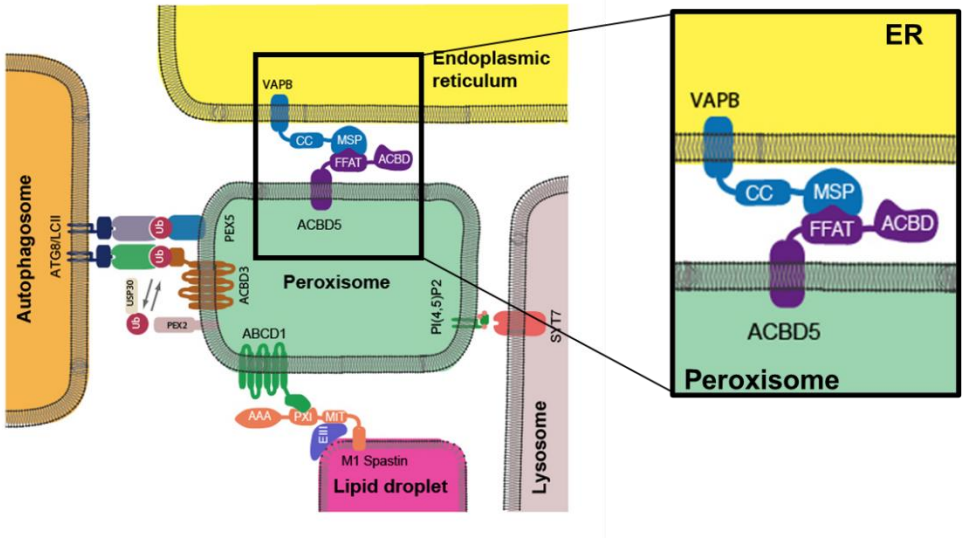

Figure 3. Peroxisomal contact sites. ER and peroxisomes maintain membrane contact through ACBD5-VAPB communication. Adapted from Sargsyan and Thoms (2020).

ACBD5 and its paralogue ACBD4 on the peroxisome are binding VAPB on the ER (Costello et al., 2017a, 2017b; Hua et al., 2017) (*Figure 3*). The tail-anchored proteins ACBD4 and ACBD5 contain the name-giving Acyl-Coenzyme A-binding domain at the N-terminus, the VAPB-binding FFAT motif, a coiled-coil region, and a single transmembrane domain at the C-terminus (Costello et al., 2017a). ACBD5 binds VLCFA as CoA esters and is involved in their transport to peroxisomes and peroxisomal β-oxidation (Ferdinandusse et al., 2017; Hua et al., 2017; Yagita et al., 2017). The ACBD5-VAPB tether is also important for peroxisome growth and stabilization of peroxisome position in the cells (Costello et al., 2017a; Hua et al., 2017). ACBD5 deficiency in patients results in severe neurological impairment, white matter disease and retinal dystrophy (Abu-Safieh et al., 2013; Ferdinandusse et al., 2017; Bartlett et al., 2021). ACBD5-deficient mice largely represent the human phenotype (Darwisch et al., 2020). A detailed lipidomic profiling of ACBD5-deficient mice revealed tissue-specific changes of lipid metabolism,

suggesting the specific role of ER-peroxisome contact depending on the tissue-type (Darwisch et al., 2020).

Recently, VPS13D was found to bind peroxisomes through interaction with GTPase Miro1v4 (peroxisomal transcript variant of mitochondrial outer membrane protein Miro1), and ER through interaction with VAPs (Guillén-Samander et al., 2021). Miro1 and Miro1v4 have two canonical EF-hand with Ca^{2+} binding properties (Klosowiak et al., 2013; Guillén-Samander et al., 2021). The EF-hand is essential for ER-mitochondria and ER-peroxisome MCS formation through VPS13D (Guillén-Samander et al., 2021).

Another peroxisome-ER MCS was suggested from Xiao et al. (2019) to be formed by $PI(4,5)P_2$ on the peroxisomal membrane and extended synaptotagmins on the ER. This MCS is supposed to be the site of cholesterol trafficking between the participating organelles (Xiao et al., 2019). The used methodology and conclusions on this MCS are, however, critically debated in the peroxisome field (Chornyi et al., 2021).

Additional ER-peroxisome MCS can be stimulated pharmacologically with ceapins (Torres et al., 2019). The interacting partners here are ER-resident ATF6α and peroxisomal membrane protein ABCD3 (Torres et al., 2019).

1.12 Genetically encoded Ca^{2+} indicators

In vivo measurement of Ca^{2+} dynamics inside cellular organelles became possible after the development of Ca^{2+}-sensitive fluorescent proteins termed genetically encoded Ca^{2+} indicators (GECI) (Pozzan and Rudolf, 2009; Gibhardt et al., 2016). Successful measurements of ER, mitochondrial, cytosolic and lysosomal Ca^{2+} with GECIs have been described (Whitaker, 2010; McCue et al., 2013). The two groups of GECI comprise intensiometric and ratiometric sensors (Pérez Koldenkova and Nagai, 2013). The intensiometric sensors are single fluorophores, usually GFP-based GECI. The ratiometric sensors are advantageous, because they act independently of the sensor expression levels and provide more direct information about Ca^{2+} concentrations (Pérez Koldenkova and Nagai, 2013). Ratiometric pericam is a single fluorophore-based GECI that has M13 and calmodulin (CaM) as Ca^{2+} binding domains and circularly permuted EYFP (cpEYFP) as fluorophore (Nagai et al., 2001) (*Figure 4*). cpEYFP shows a bimodal excitation spectrum (~420 nm and ~505 nm) and emission in the YFP range (peak at 530 nm) (Nagai

et al., 2001). The 505/420 ratio is a measure of Ca^{2+} concentration, as in the presence of Ca^{2+}, the 505/420 ratio increases.

Another type of ratiometric GECI is chameleon-type based on Förster resonance energy transfer (FRET) (Palmer and Tsien, 2006; Pérez Koldenkova and Nagai, 2013) (*Figure 4*). These GECIs have a Ca^{2+} binding domain, usually CaM. Ca^{2+} binding to CaM results in a conformational change of the GECIs, that in case of FRET sensors decreases the distance between the donor (typically CFP) and acceptor (typically a YFP variant) enabling FRET (Pérez Koldenkova and Nagai, 2013). FRET can be measured as a drop in CFP emission and an increase in FRET. The FRET/donor ratio (FRET ratio) correlates with Ca^{2+} concentration.

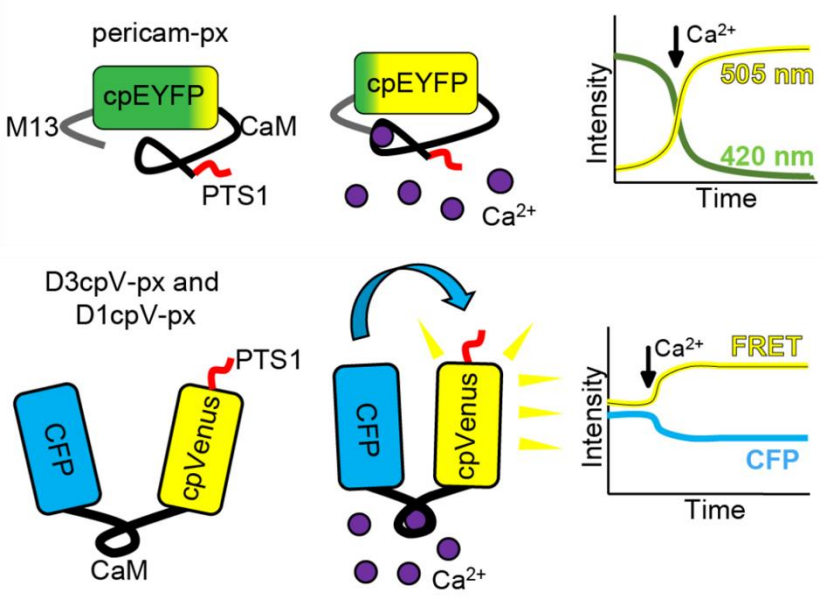

Figure 4. Peroxisomal GECIs. Pericam-px is the ratiometric pericam targeted to peroxisomes. It is a single fluorophore based GECI. Upon Ca^{2+} increase 505/420 ratio rises. D3cpv-px and D1cpV-px are FRET-based GECIs. The FRET efficiency rises in the presence of Ca^{2+}. Published also in Sargsyan et al. (2021).

1.13 Induced pluripotent stem cell-derived cardiomyocytes

Human induced pluripotent stem cells (hiPSCs) are stem cells made from somatic cell sources through cell reprogramming (Takahashi et al., 2007; Yu et al., 2007). Their

differentiation can be directed into virtually any cell type, including neurons and CMs. Highly pure CMs can be generated with small-molecule modulators of Wnt signaling by first activating and then inhibiting the Wnt pathway (Lian et al., 2013), and metabolic selection with lactate-enriched and glucose-depleted medium (Tohyama et al., 2013). hiPSC derived CMs (hiPSC-CMs) can be studied with regard to their molecular, cellular, metabolic, and electrophysiological properties and are a versatile substrate in cardiac research (Yoshida and Yamanaka, 2011). In addition, these cells are effectively used in patient-specific disease modeling ranging from arrhythmias to cardiomyopathies and heart failure (Borchert et al., 2017; Prondzynski et al., 2019).

1.14 Adeno-associated virus and CM transduction

Adeno-associated viruses (AAVs), members of *Parvovirus* family, are a widely applied tool for *in vitro* and *in vivo* gene transduction due to their safety, high transduction efficiency, and prolonged as well as relatively stable gene expression (Kimura et al., 2019). AAV serotypes differ in their tissue tropism (Hauck et al., 2003). AAV vectors have been applied for efficient expression of the Ca^{2+} sensor in mouse hearts after intravenous injection using cytomegalovirus (CMV)-enhanced myosin light chain2v promoter (Müller et al., 2006; Kaestner et al., 2014). Specificity of gene transfer here can be further increased by driving expression with a strong cardiac promoter such as the human cardiac troponin T promoter (Werfel et al., 2014). High transduction efficiency of hiPSC-CMs can be achieved with AAV serotype 6 (AAV6) (Rapti et al., 2015).

1.15 Peroxisomal lactate dehydrogenase

Lactate dehydrogenase (LDH) catalyzes the reversible conversion of pyruvate to lactate with the oxidation of NADH to NAD^+. It is a cytosolic enzyme that exists as tetramer. LDH is encoded by *LDHA*, *LDHB*, *LDHC,* and *LDHD* genes (Farhana and Lappin, 2021). As a result, various combinations of the protein products of LDHA and LDHB subunits make the five types of the enzyme (Farhana and Lappin, 2021). The *LDHB* has a highly conserved PTS1 signal after the stop codon (Schueren et al., 2014). Due to the high translational readthrough of LDHB, 2 to 8% of the total cellular LDHB is targeted to the peroxisome (Schueren et al., 2014). This form of LDHB is also called LDHBx. Peroxisomal

LDH is a catalytically active enzyme involved in the reoxidation of NADH to NAD^+ producing protons as a byproduct (Baumgart et al., 1996).

Therefore, it may be the crucial enzyme of the elusive redox shuttle system across the peroxisomal membrane that can replenish the NAD^+ pool of peroxisomes necessary for a functional β-oxidation cascade (McClelland et al., 2003) (*Figure 5*).

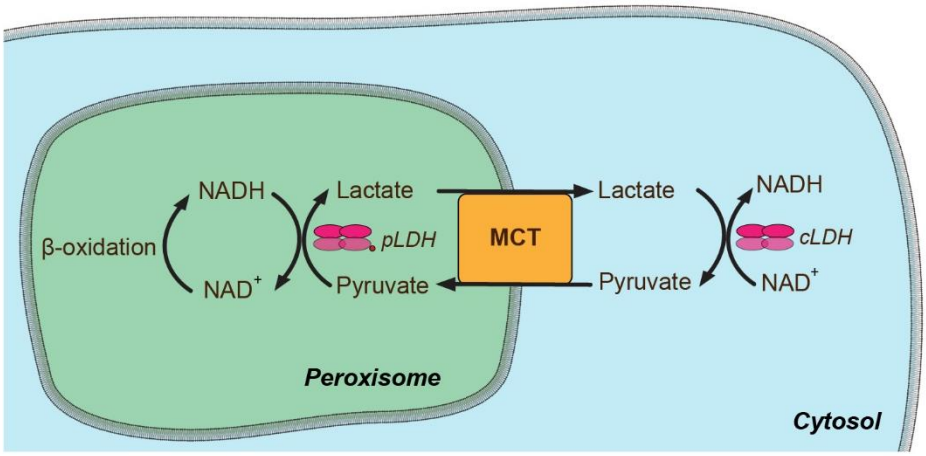

Figure 5. Peroxisomal lactate shuttle system for the re-oxidation of NADH generated by β-oxidation in peroxisomes. Cytosolic pyruvate enters peroxisome by the monocarboxylate transporter (MCT). Peroxisomal LDH (pLDH) converts it to lactate. Simultaneous re-oxidation of NADH to NAD^+ enables the β-oxidation. Lactate exits peroxisome by MCT and is converted to pyruvate by the cytosolic LDH (cLDH). Based on the model suggested by McClelland et al. (2003).

1.16 Super resolution microscopy

Conventional light microscope has a limited spatial resolution due to the diffraction of light also called Abbe's limit after the author who described it first (Abbe, 1873). The diffraction limit depends on the wavelength of the light and the numerical aperture of the objective (Huang et al., 2010). Abbe's limit results in a detection of spatially spread signal from a fluorescent point emitter. The fundamental microscope resolution of roughly 200 nm is much higher than the size of peroxisomes (Saka and Rizzoli, 2012; Soliman et al., 2018), making conventional light microscopic methods not exact for characterization of the fine structure of peroxisomes. Abbe's limit can be broken by applying super-resolution approaches exploiting state transitions of fluorophores (Huang et al., 2010). Here, either

the temporal approach to image stochastic emission (Betzig et al., 2006; Hess et al., 2006; Rust et al., 2006) or spatial modulation of the fluorescence behavior of molecules within a diffraction-limited region can be applied (Hell and Wichmann, 1994; Klar and Hell, 1999). The first method is the basis of localization-based techniques photoactivatable light microscopy (PALM) and stochastic reconstruction microscopy (STORM) where photoswitchable fluorophores are used with specific excitation schemes (Schnitzbauer et al., 2017). The spatial modulation with illumination-based approach is the basis of stimulated emission depletion (STED) microscopy, which uses two lasers (Hell and Wichmann, 1994). One laser stimulates the fluorescent molecules (excitation laser); the second laser, STED laser, eliminates the peripheral signal (Kohl et al., 2013) by depleting fluorescence emission and shaping the emitted signal to sub-diffraction scales (Schermelleh et al., 2019). T-tubule membrane and Ca^{2+} transport protein structures in CMs were resolved with STED nanoscopy at resolution of ~60 nm so that early changes of membranes after myocardial infarction could be visualized (Wagner et al., 2012; Kohl et al., 2013). Remarkably, STED in contrast to confocal microscopy resolved the hollow membrane rings of T-tubules (Wagner et al., 2012).

2 Aim of this study

Efficient and consistent Ca^{2+} measurements using GECI have been so far performed in several cellular compartments, such as the cytosol, ER, mitochondria and lysosomes, enabling detailed characterization of Ca^{2+} homeostasis in these compartments (Whitaker, 2010; Zhao et al., 2011; Matsuda et al., 2013; McCue et al., 2013; Suzuki et al., 2014). Still, peroxisomal Ca^{2+} handling remains largely enigmatic. On one hand, there are obvious contradictions about peroxisomal Ca^{2+} levels (Drago et al., 2008; Lasorsa et al., 2008), on the other, peroxisome localization close to the T-tubule – SR junction raises the questions about possible peroxisomal involvement in Ca^{2+} handling of cardiomyocytes. Finally, the presentation of PBD patients with arrhythmias in the later course of the disease may mean that peroxisomal Ca^{2+} directly contributes to excitation-contraction processes. Therefore, **the aim of this work is the study of peroxisomal Ca^{2+} import and identification of its main players**.

To reach this aim, I defined the following objectives:

- Establishment of a reliable and reproducible approach of peroxisomal Ca^{2+} measurement for the analysis of Ca^{2+} levels under resting conditions and identification of the maximal changes under near-physiological stimulation in non-excitable cells.
- Establishment of an approach to measure peroxisomal Ca^{2+} changes in cardiomyocytes when cytosolic Ca^{2+} increases.
- Identification of the possible Ca^{2+} source for peroxisomes by proximity analysis of the main cellular Ca^{2+} contributors to peroxisomes.
- Improvement of the imaging and analysis techniques of peroxisome morphology.
- Analysis of ER-peroxisome contacts and of their role in effective Ca^{2+} trafficking.
- Identification of Ca^{2+} import machinery in peroxisomes.

3 Material & Methods

3.1 Material

3.1.1 General material, devices and chemicals

Table 1. Consumables

Device	Type	Company
Chambered cover glass	8-well, #1.5H	Cellvis
Cell culture flask	50 mL, 25 cm²	Greiner bio-one
Cell culture flask	250 mL, 75 cm²	Greiner bio-one
Cell dishes	35 mm, Cell+	Sarstedt
Cell scrapers	Red, blue	Sarstedt
Conical tubes	15 mL, sterile	Falcon
Conical tubes	50 mL, sterile	Falcon
Cover glasses	Nr 1.5, 25 mm	+ RSA tec
Cryo tubes	1.8 mL	Thermo Scientific
Filter paper sheets	Blotting paper	Sartorius AG
Freezing container	Cryo 1 C, 5100-0001	Nalgene
Microplate	96-well, flat bottom	Greiner bio-One
Microscope Slides	SuperFrost® Plus, Menzel Gläser, 25 mm, #1.5	Thermo Scientific
Neubauer chamber	0.100 mm Depth, 0.0025 mm²	Assistent
Nitrocellulose blotting membrane	AmershamTM ProtranTM 0.2 µm	GE Healthcare
Nitrocellulose blotting membrane	AmershamTM ProtranTM 0.45 µm	GE Healthcare
Parafilm	M, laboratory film	Bemis
Petri dishes	92x16 mm	Sarstedt
Pipette filter tips	10 µL; 100 µL; 1000 µL	Sarstedt

Pipette tips (not sterile)	2.5 µL; 10 µL; 20 µL; 200 µL; 1000 µL	Sarstedt
Plates for cell culture	6-well, sterile, with lid	Greiner bio-one
Plates for cell culture	24-well, sterile, with lid	Greiner bio-one
PP Tube sterile	14 ml	Greiner bio-one
Reaction tubes	200 µL; 1.5 µL; 2 µL	Sarstedt
Serological pipettes	5 mL, 10 mL, 25 mL	Sarstedt

Table 2. Devices and instruments.

Device	Type	Company
Aspirator	Vacusafe	Integra
Centrifuge	Universal 320, rotor 1619	Hettich
Centrifuge	Mikro 200R, rotor 2424-B	Hettich
Centrifuge	5417R	Eppendorf AG
Centrifuge	5424	Eppendorf AG
Centrifuge	5810R	Eppendorf AG
Centrifuge	mini, FugeOne®	Starlab GmbH
Centrifuge	mini, Sprout	Biozym
Electrophoresis systems for SDS-PAGE	Mini-PROTEAN Tetra Cell	Bio-Rad Laboratories
Electrophoresis systems for agarose gels		Analytik Jena
Gel Imager	BioDocAnalyze, Software	Biometra
Hood (for cell culture)	HB2448	Lamin Air
Ice machine		Ziegra Eismaschinen
Incubator	Shaking, for bacterial cultures Memmert GmbH	Memmert

Incubator (cell culture)	Vios 160i, CO2 incubator	Hera cell, Thermo scientific
Lab gas burner (Bunsen burner)	GASI	Schütt
Magnetic stirrer	with temperature control	Heidolph Instruments
Magnetic stirrer	with temperature control, Combimag RCT	IKA-Werke
Microplate reader	BioTek Synergy Mx + power supply	BioTek Instruments
Microscope (bright field, for cell culture)	Eclipse TS100	Nikon
Microscopes (fluorescent)	D1 Observer with Zeiss Colibri 2 and Evolve 512 Delta EMCCD acquisition camera	Zeiss
	Axio Observer Z1 with Zeiss Colibri 7, Definite Focus.2, Zeiss Axiocam 702 and Apotome.2	
	Leica SP8 STED microscope	Leica Microsystems
Microwave oven	CG 820	Panasonic
pH meter	357469	Schott Geräte
Pipette controller	10 µL	Falcon, Corning
Pipette, manual, Eppendorf Research®	2.5 µL, 100 µL, 200 µL, 1000 µL	Eppendorf AG
Pipette, manual, ErgoOne®	20 µL	Starlab
Pipette, manual, Pipetman®		Gilson, Inc.

Rocking platform		GFL Gesellschaft für Labortechnik mbH
Rocking platform	Biometra Fast Blot	Biometra
Semi-dry blotting system	Nanodrop ND-1000 Software: ND-1000 V3.7.0	Biometra
Spectrophotometer	TB2m Biometra	Peqlab
Thermo block	Thermostat 5320	Biometra
Thermo block	Thermomixer compact	Eppendorf AG
Thermo block	T3	Eppendorf AG
Thermocycler	labcycler	Biometra
Thermocycler	Genie 2TM	SensoQuest
Vortex mixer	1002	Bender & Hobein
Water bath		GFL
Weight balance	LAS-4000	Sartorius AG
Western blot documentation system		Fujifilm

Table 3. Chemicals and reagents

Chemical/reagent	Product number	Manufacturer
2-Propanol	1096342500	Emsure, Merck
Acetic acid	6755	Roth
Acrylamide solution, 30% with 0.8% bisacrylamide	3029.1	Roth
Agarose	Bio-41025	Bioline
Albumin fraction V, ≥ 98%	8076.2	Roth
Ampicillin sodium salt	A9518-25G	Sigma-Aldrich
Ammonium persulfate (APS)	113H0315	Serva
Aqua ad injectibilia (also	PZN: 03113087	Braun

used as Nuclease free water)		
B-27™ Supplement (50x)	17504044	Gibco, Thermo Fisher
BCA Assay Reagent A	UP95424A	Interchim
BCA Assay Reagent B	UP95425A	Interchim
Bromophenol blue	8122-5g	Merck
Caffeine	C0750	Sigma-Aldrich
Calcium chloride, ≥ 97%	CP89.2	Roth
Citric acid monohydrate	100244	Merck
cOmplete™ Protease Inhibitor Cocktail Tablets, EDTA-free	04693116001	Roche
D(+)-Glucose	X997.2	Roth
Digitonin 5%	BN2006	Invitrogen
Dimethyl sulfoxide (DMSO)	39757	Serva Electrophoresis
Disodium phosphate (Na_2PO_4)	T877	Roth
dNTP Mix	U1511	Promega
Dulbecco's Modified Eagle Medium (DMEM), 1 g/L D-Glucose	11880-028	Gibco, Thermo Fisher
DMEM, 4.5 g/L D-Glucose	10313-021	Gibco, Thermo Fisher
Dulbecco's Phosphate Buffered Saline (PBS)	D8537-500ML	Sigma
Ethylenediaminetetraacetic acid (EDTA)	131669.1209	AppliChem, PanReac
Ethylene glycol-bis (β-aminoethyl ether)-N,N,N',N'-tetraacetic acid (EGTA), ≥ 97.0%	3054.2	Roth
Ethanol absolute	5054.2	Roth
Ethanol absolute for analysis	1.00983.2500	Emsure, Merck
Fetal Bovine Serum (FBS, FCS)	S140B-500	Biowest

GelRed	#41003	Biotium
GeneRuler DNA Ladder Mix, ready-to-use	SM0334	Thermo Scientific
Geltrex	A-14133-02	Gibco
GlutaMAX™ -I (100x)	35050-061	Gibco
Glycerol, anhydrous	A3552	Applichem
4-(2-hydroxyethyl)-1-piperazineethanesulfonic acid (HEPES), ≥ 99.5%	HN78.1	Roth
Hi-Di Formamide	4440753	Applied Biosystems, Thermo scientific
Histamine dihydrochloride, ≥ 98.5%	4017.1	Roth
Hydrochloric acid (HCl)	1003141000	Merck
Ionomycin free acid, 1 mg	sc-263405	Sigma
Lysogeny Broth (LB)-medium (Luria/Miller), powdered	X968.1	Roth
LB-Agar, powdered	X969.1	Roth
L-glutamine solution	G8540	Sigma-Aldrich
Lumi-Light Plus Western Blotting Substrate	12 015 196 001	Roche
Lumi-Light Western Blotting Substrate	12 015 200 001	Roche
Magnesium chloride hexahydrate, ≥ 99%	2189.1	Roth
Methanol	8045	J.T. Baker
Milk powder	T145.3	Roth
Monopotassium phosphate (KH_2PO_4)	3904	Roth

Nigericin, Sodium Salt, *Streptomyces hygroscopicus*	481990-5MG	Merck
N,N,N′,N′-Tetramethylethan-1,2-diamin (TEMED)	2367.1	Roth
Nonidet P (NP)-40	74385	Fluka Analytical
Opti-MEM	11058-021	Gibco
PageRuler™ Prestained Protein Ladder	26616	Thermo Fisher Scientific
Paraformaldehyde (PFA), 4% in PBS	11762.00500	Süsse Labortechnik
PBS (Dulbecco´s PBS) for cell culture	L0615-500	Biowest
Penicillin-Streptomycin	P4333-100ML	Sigma
Ponceau-S solution	P7170	Sigma-Aldrich
Potassium acetate, ≥99%		Sigma-Aldrich
Potassium chloride, ≥ 99.5%	6781.1	Roth
ProLong Gold Antifade reagent	P36934	Thermo Fisher
ProLong Gold Antifade reagent with DAPI (4′,6-diamidino-2-phenylindole)	P36935	Thermo Fisher
RNAse A	556746	Calbiochem
ROTI-Load 1 (reducing), 4x concentr.	K929.2	Roth
RPMI Medium 1640 + GlutaMAX	72400-021	Gibco
Sodium bicarbonate ($NaHCO_3$)	0965	Roth
Sodium dodecyl sulfate (SDS), 20%	1057	Roth
Sodium chloride, ≥ 99%	3957.1	Roth
Sodium hydroxide	6771.1	Emsure
Sodium L-Lactate ~98%	L7022	Sigma

Thapsigargin	BML-PE180-0001	Enzo Life Sciences
Thiazovivin	420220	Merck
Tris ≥ 99.9% p.a.	5429.3	Roth, PUFFERAN
Tris	5429.3	Roth
TritonX100	9036-19-5	Merck
0.25% Trypsin-EDTA	25200-056	Gibco
Trypsin/EDTA solution, 0.05%/ 0.02% (w/v)	L2143	Biochrom
Tween 20	8.22184.0500	Merck
Versene 1:5000	15040-033	Gibco
β-Mercaptoethanol	M3148-25ml	Sigma-Aldrich

3.1.2 Enzymes and Kits

Table 4. Enzymes and kits used for specific methods

Description / purpose	**Product / component name**	**Manufacturer**
Digestion of PCR-product and Vector	BamHI-HF	NEB Inc
	CutSmart® Buffer	NEB Inc
	DpnI	NEB Inc
	HindIII-HF	NEB Inc
	Hpa1	NEB Inc
	EcoRI-HF	NEB Inc
Effectene Transfection Reagent	Buffer EC	Qiagen
	Enhancer	Qiagen
Endoglycosidases	EndoH, 10x Glycoprotein Denaturing Buffer, 10x GlycoBuffer 3	NEB Inc

	PNGase F, 10x Glycoprotein Denaturing Buffer, 10x GlycoBuffer 2	NEB Inc
High pure PCR product purification kit	Binding buffer	Roche
	Wash buffer	Roche
Lipofectamine 3000 Transfection Reagent	Lipofectamine 3000 reagent,	Thermo Fisher
	P-3000 reagent,	Thermo Fisher
Lipofectamine LTX & PLUS Transfection Reagent	Lipofectamine LTX reagent	Thermo Fisher
	PLUS reagent	Thermo Fisher
PCR kit	5x HiFi GC with Mg	KAPA Biosystems
	KAPA HiFi HotStart DNA Polymerase	KAPA Biosystems
PCR kit	5x HiFi Buffer	BioCat
	PRECISOR High-Fidelity DNA Polymerase	BioCat
PCR clean-up, Gel extraction	Binding Buffer NTI	Roche
	Wash Buffer NT3	Roche
PCR for sequencing, Applied Biosystems	5x Sequencing buffer	Applied Biosystems, Life Technologies
	Big Dye Terminator	Applied Biosystems, Life Technologies
Plasmid DNA purification kit	Buffer RES (RNase A added beforehand)	Machery-Nagel
	Buffer LYS	Machery-Nagel
	Buffer NEU	Machery-Nagel
	Buffer EQU	Machery-Nagel
	Buffer WASH	Machery-Nagel
	Buffer ELU	Machery-Nagel

Rapid DNA Ligation Kit	T4 ligase	Thermo Scientific
	T4 ligase buffer	Thermo Scientific
Lipofectamine 3000 Transfection Reagent	Lipofectamine 3000 reagent	Thermo Fisher
	P-3000 reagent	Thermo Fisher
Lipofectamine LTX & PLUS Transfection Reagent	Lipofectamine LTX reagent	Thermo Fisher
	PLUS reagent	Thermo Fisher

3.1.3 DNA plasmids

Table 5. Constructs generated prior to this study

Construct used in this study	Bacterial resistance	Company/ provider / PST number
D3cpV-PTS1	Ampicillin	PST 1738
mito-BFP	Kanamycin	Addgene: 49151, gift from Gia Voeltz, PST 1529
EGFP-ACBD5.1	Kanamycin	Costello et al., 2017a, PST 2155
ACBD5-FLAG	Kanamycin	Costello et al., 2017a, PST 2157
pEBFP-C1-LDHBx	Kanamycin	PST 1587
pcDNA3.1myc/HIS(-)A-HsPEX11Bfl (also PEX11-myc)	Ampicillin	Soliman et al., 2018, PST 1026
pcDNA-4mtD3cpv	Ampicillin	Addgene: 36324, PST 1719
pcDNA-D3cpv	Ampicillin	Addgene: 36323, PST 1718
Ratiometric-Pericam (for mitochondria)	Ampicillin	Nagai et al., 2001 (from AG Bogeski), PST 1982
D1cpV	Ampicillin	Addgene: 37479, PST 2139
CMV-R-GECO1	Ampicillin	Zhao et al., 2011 (from AG Bogeski), Addgene: 32444, PST 2150
pEGFP-SKL	Kanamycin	PST 990

pEF DEST ACBD5 Opsin	Ampicillin	PST 1192
pEF-DEST-c-ops-FIS1	Ampicillin	PST 1330
pEF-DEST-c-ops-Pex26delta STOP (= ohne STOP)	Ampicillin	PST 1312
Pericam-PTS1	Ampicillin	PST 2170
D1cpV -PTS1	Ampicillin	PST 2169

3.1.4 Viral construct

Table 6. Viral vector

Construct ID	Volume (mL)	Titer (vg/mL)	vg total
AAV6-ssTnT-D3cpv-PTS1-(from PST1738)	2.0	6.41E+12	1.28E+13

3.1.5 Oligonucleotides

Table 7. Oligonucleotides

Oligonucleotide	Sequence
OST 2150	CTA TGT TTG GCC TGC CCC AGT GGC AGT GGG ACG GGC TGC CCT G
OST 2151	CAG GGC AGC CCG TCC CAC TGC CAC TGG GGC AGG CCA AAC ATA G
OST 2154 (for PST 2162 seq.)	CCA GAG CGA TGC CTA TGG GG
OST 2159 (intern seq. PST 2162 fw. 601)	TGG GCT GAG GAA TAT TTG GA
OST 2160 (intern seq. PST 2162 rev. 1680)	ACG AAC GCT GAG GGC AGC TG
T7 promoter, forward	TAA TAC GAC TCA CTA TAG GG

T7 terminator, reverse	GCT AGT TAT TGC TCA GCG G
BGH reverse	TAG AAG GCA CAG TCG AGG
CMV promoter	CGC AAA TGG GCG GTA GGC GTG

3.1.6 SiRNA sequences

Table 8. siRNA sequences

siRNA	Company	Sequence
Negative control siRNA (20 nmol)	**Qiagen**	UUCUCCGAACGUGUCACGUdTdT (sense)
		ACGUGACAGGUUCGGAGAAdTdT (antisense)
siACBD5, Silencer Select Pre-designed	**ambion**	GCAUUCACCAAGAUAUAAATT (sense)
		UUUAUAUCUUGGUGAAUGCAA (antisense)
siPXMP2-6, FlexiTube siRNA 20 nmol	**Qiagen**	CAGCGAGAGCAGAACCAAUTT (sense)
		AUUGGUUCUGCUCUCGCUGGG (antisense)
siPXMP2-7, FlexiTube siRNA 20 nmol	**Qiagen**	GACCGAAUUAGGAUCACAATT (sense)
		UUGUGAUCCUAAUUCGGUCCA (antisense)

3.1.7 Antibodies

Table 9. Antibodies for western blot

Antibody	Host species	Dilution	Product number	Manufacturer
Anti-PXMP2	Rabbit	1:250	24801-1-AP	Proteintech

Anti-Pex14	Rabbit	1:500	10594-1-AP	Proteintech
Anti-ACBD5	Rabbit	1:400	HPA012145-100ul	Sigma-Aldrich
Anti-ACAA1	Rabbit	1:1000	12319-2-AP	Proteintech
Anti-opsin (supernatant of hybridoma cells)	Mouse	1:100		Produced by Corinna Dickel
Anti-glyceraldehyde-3-phosphate dehydrogenase (GAPDH)	Mouse	1:10,000	G8795	Sigma-Aldrich
Anti-mouse horseradish peroxidase (HRP)-coupled	Donkey	1:10,000	715-035-150	Jackson Immuno Research
Anti-catalase	Rabbit	1:500	21260-1-AP	Proteintech
Anti-catalase	Rabbit	1:500	24316	Oxis Research
Anti-α-tubulin	Mouse	1:500	T9026	Sigma-Aldrich
Anti-rabbit horseradish peroxidase (HRP)-coupled	Goat	1:10,000	111-035-003	Jackson Immuno Research
Anti-PMP70	Mouse	1:1000	SAB4200181	Sigma-Aldrich
Anti-Myc-tag	Rabbit	1:500	2272S	Cell Signaling
Anti-VAPB	Mouse	1:500	66191-1-Ig	Proteintech

Table 10. Antibodies for immunofluorescence

Antibody	Host species	Dilution	Product number	Manufacturer
Anti-L-type Ca^{2+} channel α1C/D/F/S (D-19)	Goat	1:200	sc-103588	Santa Cruz Biotechnology
Anti-mouse IgG-Alexa Fluor® 488	Donkey	1:200	A-21202	Invitrogen
Anti-mouse IgG-Cy™3	Donkey	1:200	715-166-150	Jackson Immuno Research
Anti-goat IgG-Cy™3	Donkey	1:200	705-165-147	Jackson Immuno Research
Anti-rabbit IgG-Alexa Fluor® 488	Goat	1:500	A-11008	Life Technologies
Anti-PEX14	Rabbit	1:500	10594-1-AP	Proteintech
Anti-catalase	Rabbit	1:500	24316	Oxis Research
Anti-α-tubulin	Mouse	1:500	T9026	Sigma-Aldrich
Anti-ryanodine receptor	Mouse	1:200	MA3-916	Invitrogen
Anti-mouse IgG-Alexa Fluor® 633	Goat	1:1000	A-21053	Invitrogen
Anti-PMP70	Mouse	1:500	SAB4200181	Sigma-Aldrich
Anti-rabbit IgG-Alexa Fluor® 647	Donkey	1:1000	711-605-152	Jackson ImmunoResearch

3.1.8 Buffers and solutions

PBS

137 mM	NaCl
2.7 mM	KCl
10 mM	Na_2HPO_4
1.8 mM	KH_2PO_4
pH = 7.4	

Agar

40 g/L LB-Agar powder dissolved in distilled water, and autoclaved

LB-medium

25 g/l LB-Medium powder dissolved in distilled water, and autoclaved

Buffers for plasmid isolation

P1

50 mM	Tris/HCl pH=8.0
100 µg/mL	RNase A (fresh)

P2

200 mM	200 mM NaOH
1%	SDS

P3

3 M	Potassium acetate pH = 5.5

Cell lysis buffer

150 mM	NaCl
1%	NP-40
0.5%	Sodium deoxicholate
50 mM	Tris pH 8.0
2%	SDS

SDS-PAGE sample buffer, 4x

160 mM	Tris/HCl, pH 6.8
8%	SDS
0.01%	bromophenol blue
20%	β-mercaptoethanol or DTT
20%	Glycerol

SDS-PAGE buffer

25 mM	Tris
1%	SDS
1.92 M	Glycine

Transfer buffer for semi-dry western blot

25 mM	Tris
260 mM	Glycine
20%	Methanol

Tris-buffered saline (TBS)

50 mM	Tris/HCl, pH 7.6
150 mM	NaCl

TRIS-Acetate-EDTA (TAE) buffer

40 mM	Tris/HCl, pH 8.0
0.1%	Acetic acid
1 mM	EDTA

Buffers for cell imaging

Stock solutions

3 M	NaCl	autoclaved
1 M	KCl	autoclaved
1 M	HEPES, pH = 7.4	autoclaved
1 M	Glucose	sterile filtration
1 M	$MgCl_2$	autoclaved
1 M	$CaCl_2$	autoclaved
500 mM	EGTA	sterile filtration

Standard buffer with calcium (working buffer)

145 mM	NaCl
4 mM	KCl
10 mM	HEPES
10 mM	Glucose
2 mM	$MgCl_2$
2 mM	$CaCl_2$
pH = 7.4	Sterile filtration

EGTA buffer without calcium (working buffer)

145 mM	NaCl
4 mM	KCl

10 mM	HEPES
10 mM	Glucose
2 mM	$MgCl_2$
2 mM	EGTA
pH = 7.4	Sterile filtration

Calibration buffer (working buffer)

145 mM	NaCl
4 mM	KCl
10 mM	HEPES
10 mM	Glucose
pH = 7.2	

Histamine, working solution

200 µM (end concentration on cells 100 µM).

Thapsigargin, working solution

2 µM (end concentration on cells 1 µM)

3.1.9 Cell culture medium

HeLa culture medium

DMEM, 1.0 g/L D-glucose
10% FBS
1% L-glutamine
1% Penicillin/Streptomycin

Freezing medium for HeLa cell lines

DMEM, 1.0 g/L D-glucose
20% FBS

1% L-glutamine

1% Penicillin/Streptomycin

10% DMSO

NRCM culture medium

RPMI Medium 1640 + GlutaMAX

10% FBS

1% Penicillin/Streptomycin

iPSC-CM culture medium

RPMI Medium 1640 + GlutaMAX

B-27 Supplement

1% Penicillin/Streptomycin

iPSC-CM revival medium

RPMI Medium 1640 + GlutaMAX

B-27 Supplement

1% Penicillin/Streptomycin

20% FBS

2 µM Thiazovivin

Patient fibroblast culture medium

DMEM, 4.5 g/L D-glucose

10% FBS

1% L-glutamine

1% Penicillin/Streptomycin

Patient fibroblast freezing medium

DMEM, 4.5 g/L D-glucose

20% FBS

1% L-glutamine

1% Penicillin/Streptomycin

10% DMSO

3.1.10 Software

Table 11. Software

Software	Manufacturer/reference
Axiovision 4.8, epifluorescence microscope software	Carl Zeiss AG
Fiji, image processing software	(Schindelin et al., 2012)
GraphPad Prism 9, graphing and statistics software	GraphPad Software, Inc.
LAS-X, STED microscope software	Leica Microsystems
Mathematica 10, software for algorithm implementation	Wolfram Research (Valm et al., 2017)
ZEN, epifluorescence microscope software	Carl Zeiss AG

3.2 Methods

3.2.1 Cell biology

3.2.1.1 Cell lines for cell culture

HeLa is a human epithelial cell line derived from a cervix adenocarcinoma.

crACBD5-1 and crACBD5-5 are HeLa cells from mother cell line HeLa generated through CRISPR/Cas9 with 128dup/128dup in *ACBD5* gene.

Neonatal rat cardiomyocytes (NRCMs) are freshly isolated from newborn rats.

Human induced pluripotent stem cells (hiPSC) are reprogrammed cells from skin fibroblasts.

HiPSC derived cardiomyocytes (hiPSC-CM) are cardiomyocytes differentiated from iPSCs.

Control patient fibroblasts are skin fibroblasts from healthy donors.

Patient fibroblasts (P1) are skin fibroblasts from a patient with *PEX10* pathogenic variant.

3.2.1.2 Cell culture

Culture of HeLa cell lines and fibroblasts

Cells were thawed in a water bath at 37 °C, transferred into 20 ml culture medium and centrifuged at 800 rpm for 5 min. Cell pellets were resuspended in culture medium and seeded in culture flasks and cultured at 37 °C in a 5% CO_2 and 95% humidity atmosphere. Cells were split 1:5 or 1:10 every 3 to 5 days depending on their confluency. For that, cells were washed once with PBS and detached with 1 mL trypsin/EDTA. Detached cells were resuspended in culture medium and centrifuged at 800 rpm for 5 min. The pellet was then resuspended in culture medium and seeded into new culture flasks. For freezing purpose, cells at confluency of ~80% were washed with PBS and trypsinized with 1 mL trypsin/EDTA for 2 min at 37 °C, resuspended in 9 mL culture medium and centrifuged at 800 rpm for 5 min. The cell pellet was diluted in 1.5 mL freezing medium and transferred

into cryo tubes that were placed in freezing containers at -80°C overnight (o.n.) for slow freezing.

Culture of NRCMs

After sacrificing the rats, hearts were removed from the thoracic cavity, homogenized mechanically and digested in 1 mg/mL collagenase type II containing calcium and magnesium-free PBS at 37°C with magnetic stirring. Every 20 min the supernatant was removed and transferred to the culture medium. Cells were then centrifuged, and the pellet resuspended in fresh medium, transferred to culture dish for 45 min (37 °C, 5% CO_2 and 95% humidity). NRCMs remain in the supernatant, whereas the fibroblasts adhere. NRCMs were then seeded on glass cover slips covered by Geltrex (for 1 h at 37 °C) and cultured at 37 °C in a 5% CO_2 and 95% humidity atmosphere. For splitting, cells were washed once with PBS and detached with 1 mL accutase for 10 min. Detached cells were resuspended in culture medium, centrifuged at 800 rpm for 5 min. The cell-pellet was then resuspended in fresh culture medium and seeded into new culture dishes coated with Geltrex.

Culture of iPSC-CMs

For splitting, cells were washed once with 1 mL versene and incubated in 0.25% trypsin-EDTA for 10 min at 37 °C. The cells were then resuspended in iPSC-CM revival medium and centrifuged for 10 min at 100*g. The pellet was resuspended in iPSC-CM revival medium, transferred to culture dish coated with Geltrex, and cultured at 37 °C in a 5% CO_2 and 95% humidity atmosphere.

3.2.1.3 Transfection of cells

HeLa cells and derived cell lines were transfected with plasmid DNA using Effectene Transfection Reagent according to manufacturer's instructions (Handbook, May 2002, Qiagen). NRCMs and iPSC-CMs were transfected with plasmid DNA using Lipofectamine LTX & PLUS Reagent according to manufacturer's instructions (Lipofectamine LTX & PLUS Reagent Protocol 2013). HeLa cells were transfected with siRNA using Lipofectamine 3000 Reagent according to manufacturer's instructions (Lipofectamine 3000 Reagent Protocol 2013 and Scaling Table).

For NRCM transfection with viral construct, 300,000 freshly isolated cells in 100-200 µL medium per coverslip were seeded and incubated for 1 h at 37 °C in a 5% CO_2 and 95% humidity atmosphere for better attachment of cells. Then 3 mL medium containing $4*10^5$ vg/cell was added to the cells. The optimal expression of the protein was achieved after 72 h or 96 h incubation.

3.2.1.4 Immunofluorescence staining

For immunofluorescence staining, cells were seeded on glass coverslips or chambered cover glass. 24 h after transfection (if applicable), cells were washed once with PBS, fixed with 4% PFA for 30 min and permeabilized for 10 min using 1% Triton X-100 in PBS. The cells on the glass coverslips were then blocked for 30 min with 1% BSA in PBS at 37 °C. The blocking solution was removed, and the primary antibodies diluted in the blocking solution were added to the slides and incubated for 1 h at room temperature (RT). After the incubation, the coverslips were washed three times with PBS for 5 min before the secondary antibodies diluted in the blocking solution were added. The coverslips were incubated for 1 h at RT in the dark, then washed three times with PBS for 5 min. They were then dried shortly and put on glass slides with Prolong Gold Antifade reagent with/without DAPI and left in darkness o.n. in upright position. Immunofluorescence samples were long-term stored at 4 °C.

3.2.1.5 Analysis of peroxisome proximity to Cav3 and RyR2

Analysis and image processing were performed using Fiji (http://fiji.sc/) according to ImageJ User Guide and based on the Mathematica code for organelle-organelle contact analysis (Valm et al., 2017). Briefly, the isolated cardiomyocytes from WT mice were stained with anti-Pex14 and anti-Cav3 (caveolin 3) or anti-RyR2 antibodies. Confocal overview cell images were obtained with Leica SP8 STED microscope. The images were loaded in Fiji, the cardiomyocytes were marked, and a mask was generated by the “Create Mask” function. These masks were then used when running the Mathematica code. The code was run once per cell with no pixel dilation and the segmentation algorithm “Cluster” for all images. From the output file, the ratio of the number of peroxisomes (anti-Pex14 staining) colocalizing with Cav3 or RyR2, and the total number of peroxisomes was calculated and presented as “Fraction of peroxisomes in contact”.

3.2.1.6 Analysis of peroxisome morphology

Analysis and image processing was done using Fiji (http://fiji.sc/) according to ImageJ User Guide. All images from isolated mouse CMs were obtained with a Leica SP8 STED microscope. The images from control and patient fibroblasts were taken with an Axio Observer Z1 microscope. To count peroxisomes in isolated cardiomyocytes, auto threshold of MaxEntropy was applied on confocal cell overview images of anti-Pex14 staining. Peroxisomes were then quantified automatically in the inverted image using the built-in function Analyze Particles. Particles with size smaller than 0.03 µm², and in case of fibroblasts also bigger than 3.45 µm², were excluded from analysis. Peroxisome morphology parameters area, roundness and solidity were analyzed doing the same steps but on the five-times zoomed in confocal and STED images.

$$Roundness = 4 * [Area]/(\pi * [Major\ axis]^2)$$

$$Solidity = [Area]/[Convex\ area]$$

Residual cytosolic catalase was calculated by dividing the inverted image by 255. It was then ‘subtracted’ from the original image by using Multiply images function. The cells were then marked manually, and the integrated density (IntDen) was measured.

3.2.2 Protein biochemistry

3.2.2.1 Protein isolation for SDS- polyacrylamide gel electrophoresis (SDS-PAGE)

After washing once with PBS, 1 mL ice-cold PBS was added, and cells were kept on ice for all subsequent steps. Cells were detached by cell scrapers and transferred into reaction tubes. After centrifugation at 2000 rpm for 5 min, the pellets were resuspended in cell lysis buffer and 10 sonication pulses were applied for homogenization of the lysates. The lysates were then transferred into liquid nitrogen. Cell lysates were stored at -20 °C for short-term and at -80 °C for long-term preservation. Protein concentrations were measured by bicinchoninic acid (BCA) assay according to manufacturer’s instructions. Protein lysates with appropriate amount of protein were mixed with 4x SDS-PAGE sample buffer or 4x ROTI-Load 1 to obtain 1x concentration. The samples were boiled at 95 °C for 5 min and stored at -20 °C prior to loading on the gels.

3.2.2.2 PNGase F and EndoH treatment of cell lysates

For the removal of N-linked glycosylation, treatment of cell lysates with the endoglycosidase EndoH or PNGasa F (denaturing reaction) using the supplemented material according to manufacturer´s instructions was performed.

3.2.2.3 SDS-PAGE and western blot

For the separation of protein samples according to their molecular weight, SDS-PAGE was used. A 5% acrylamide stacking gel and a running gel of 10-15%, depending on the size of proteins to be detected, were used. A pre-stained protein ladder was used for the comparison of the molecular weight of the separated proteins.

Table 12. Protocol for preparation of gels for SDS-PAGE

Component	**5% staking gel**	**10% running gel**	**12% running gel**	**15% running gel**
Total volume	2 mL	5 mL	5 mL	5 mL
Water	1.4 mL	1.9 mL	1.6 mL	1.1 mL
30% acrylamide	330 µL	1.7 mL	2 mL	2.5 mL
1.0 M Tris, pH 6.8	250 µL	-	-	-
1.5 M Tris, pH 8.8	-	1.3 mL	1.3 mL	1.3 mL
10% SDS	20 µL	50 µL	50 µL	50 µL
10% APS	20 µL	50 µL	50 µL	50 µL
TEMED	2 µL	3 µL	3 µL	3 µL

The electrophoresis was performed at 40 mA. After the SDS-PAGE, proteins were transferred to a nitrocellulose membrane. A sandwich consisting of three layers of Whatman blotting paper, membrane, gel, and three layers of blotting paper was prepared and soaked with transfer buffer. The sandwich was then placed into the semi-dry blotting system. Blotting was performed at 100 mA for 45 min to 1 h (depending on the protein size). Ponceau S staining was then applied for visualization of transferred total proteins.

For antibody binding, the membranes were shortly blocked for 5 min with 4% milk in TBS to avoid unspecific binding of the primary antibody, which was incubated o.n. at 4 °C or 1.5 h at RT. After the incubation, the membranes were washed 3 times for 6 min with TBS and incubated with horseradish peroxidase (HRP)-coupled secondary antibody diluted in 4% milk/TBS for 1h at RT. The membranes were 3 times washed with TBS for 7 min and the proteins bound to antibody-complexes were visualized by enhanced chemiluminescence (Lumi-Light or Lumi-Light Plus Western Blotting Substrate) using LAS-4000 western blot documentation system. Protein signal was quantified using Fiji software.

3.2.3 Molecular biology

3.2.3.1 Transformation of E. coli

For cloning procedures and plasmid preparation, chemically competent NEB® 5-alpha F'Iq Competent E. coli (C2992) were used. 1 µL of plasmid was added to 10 µL of competent E. coli bacterial solution. After 30 min of incubation on ice, the reaction mixture was exposed to heat shock of 42 °C for 70 sec. The mixture was subsequently cooled on ice for 2 min and 400 µL LB-medium were added. Following an incubation at 37 °C and 300 rpm for 1 h, the mixture of competent cells and LB-medium was centrifuged at 10,000 rpm and the pellet was plated LB agar plates containing 100 µg/mL kanamycin. The plates were cultivated o.n. at 37 °C. Single colonies were picked and liquid bacterial cultures were prepared by inoculation of 3.5 mL LB-medium containing 100 µg/mL kanamycin and incubation at 37 °C and 200 rpm overnight.

3.2.3.2 Isolation of plasmid DNA from E. coli

Isolation of plasmid DNA from small E. coli cultures

Plasmid DNA was isolated from 3.5 mL o.n. E. coli cultures. 1.5 mL of bacterial culture were harvested at 8000 rpm for 1 min. The pellet was resuspended in 200 µL of buffer P1. 200 µL buffer P2 was then added, and the samples were inverted 20 times and incubated for 5 min at RT. After the addition of 300 µL of buffer P3, the samples were again inverted 20 times and centrifuged for 10 min at 14,000 rpm. The supernatant was transferred into a new reaction tube, the DNA was precipitated with 0.7 volumes (500 µL)

of isopropanol and 20 min centrifugation at 14,000 rpm. The pellet was washed with 350 µL 70% ethanol, vortexed shortly and centrifuged for 10 min at 14,000 rpm. The supernatant was then removed, the DNA dried for 10 min at 37 °C and resuspended in 20 µL dH_2O.

Isolation of plasmid DNA from large E. coli cultures

To isolate the constructs, bacteria were first cultured in 100 ml LB-medium containing 100 µg/mL antibiotic incubated in 37°C at 180-200 rpm o.n. The DNA isolation from bacterial culture was done with Plasmid DNA purification kit NucleoBond® Xtra Midi, Macherey-Nagel according to the User manual January 2013, Rev.1. In the precipitation step (step 13) after addition of isopropanol and vortexing the content of the falcons the solution was distributed in four 2 ml tubes and centrifuged in a precooled centrifuge at 14,000 rpm for 30 min at 4°C. The supernatant was then removed, 300 µl of 70% ethanol was added to the transparent glass-like pellet and the tube was centrifuged at 13,200 rpm at room temperature for 5 min. The supernatant was removed, and the pellet was dried at 37°C for 10 min and then eluted in 40 µl nuclease free water. DNA concentration was measured by Nanodrop. The sequence of constructs was confirmed by the DNA sequencing. The plasmid DNA was then frozen and stored at -20°C for long time preservation.

3.2.3.3 DNA sequencing

In order to prepare the DNA for sequencing, 300 ng of DNA sample was mixed with 2 µL Big Dye 5x Buffer, 0.5 µL primer (10 pmol/µl) and 1 µL BigDye® Terminator v3.1 Ready Reaction Mix in a total volume of 10 µL. The following cycling program was applied for the reaction:

96 °C 1 min

96°C 10 sec
55 °C 10 sec
60 °C 4 min
] 24 cycles

For the purification of the product, it was mixed with 220 µL of 100% ethanol, 120 µL nuclease free water and 10 µL of 3 M sodium acetate (pH 4.6 to 4.8), vortexed and

incubated at RT for 15 min, followed by centrifugation for 15 min at 14,000 rpm. The supernatant was carefully discarded, and 300 µl of 70% ethanol was added, vortexed and centrifuged for 2 min at 14,000 rpm. After the supernatant was removed, the pellet was dried at 30 °C for 10 min (or 2 min at 60 °C). The pellet was then diluted in 10 µl Hi-Di Formamide.

3.2.4 Calcium Imaging

The cells were first incubated in Ca^{2+}-free buffer before the start of the imaging. Images were taken every three or five seconds. After taking 10 images per channel from the start of experiment (10 imaging cycles), ER-store depleting reagent dissolved in the Ca^{2+}-free buffer with the according concentration was added (*Figure 6*). 50 cycles after the start of experiment, 2 mM Ca^{2+}-containing buffer was added to the cells for a final concentration of 1 mM. The experiment continued for 50 more cycles after the addition of Ca^{2+} buffer. Individual cells were marked as regions of interest (ROI) and analyzed separately relative to the background. In case of FRET sensors, FRET to donor ratio was calculated. Background and bleed-through (BT) were corrected in the FRET/donor ratio:

$$\frac{FRET}{donor} = \frac{(FRET - background) - [(CFP - background) \times BT] - [(YFP - background) \times BT]}{CFP - background}$$

For intensiometric sensor CMV-R-GECO1, F_n/F_0 was calculated instead. For measurements with ratiometric pericam construct, emission ratio when excited by 505 nm and 420 nm was assessed.

For cell permeabilization and cytosol washout, 0.01% digitonin was used for 50 sec to 1 min. It was either done during image acquisition or prior to the start of imaging. After the completion of the digitonin incubation the whole medium was removed from the imaging chamber, cells were washed and Ca^{2+}-free buffer was added to the cells.

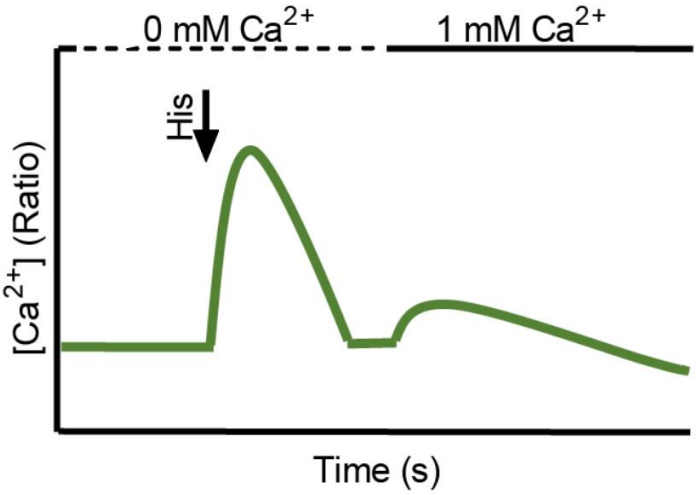

Figure 6. Experimental paradigm for Ca^{2+} imaging. Published also in Sargsyan et al. (2021).

The dissociation constant K_d value in living cells was determined based on the saturation protocol described for cytosolic GECIs from Park and Palmer (2015). Cells were washed with EGTA-free calibration buffer and incubated for 5-6 minutes in calibration buffer containing 3 mM EGTA and 5 µM ionomycin until the FRET signal decreased and reached its minimum, R_{free}. D3cpV-px expressing cells were additionally incubated in 0.01% digitonin, 3 mM EGTA and 5 µM ionomycin for 50 seconds then washed with EGTA-free calibration buffer. Cells were then washed and immediately exposed to different Ca^{2+} concentrations (once per experiment) that resulted in FRET increase, R_{final}. Buffers with different Ca^{2+} concentrations were made as described previously by mixing 10 mM EGTA and 10 mM Ca^{2+}-EGTA buffers with predefined proportions (Park and Palmer, 2015). The results were fit in one-site saturation model with Hill coefficient (as advised by the original designer of cytosolic D3cpV (Palmer et al., 2006; Park and Palmer, 2015)) using GraphPad Prism 9 software. Absolute levels of peroxisomal Ca^{2+} were assessed using the measured K_d value, the known properties of D3cpV and following the procedures of absolute Ca^{2+} concentration calculation described by Palmer and Tsien (2006).

3.2.5 Statistics

Statistical analysis was performed using GraphPad Prism 9 software by Student's unpaired t-test assuming normal distribution when comparing two groups, one-way ANOVA with Tukey's post hoc test for multiple comparisons when comparing more than two groups, or nested one-way ANOVA with Tukey's post hoc multiple comparisons test when analyzing nested data. If not others indicated, data are presented as Tukey's box plots: the box is limited by 25th and 75th percentiles. Data points larger than 75th percentile plus 1.5IQR (interquartile range) or smaller than 25th percentile minus 1.5IQR are presented as outliers. More extreme outliers are excluded from the graphical presentation. The whiskers cover all other data. Significance is assumed if the p-values are smaller than 0.05.

4 Results

4.1 Peroxisomal Ca^{2+} handling in non-excitable cells

4.1.1 Validation of peroxisomal Ca^{2+} sensors

Three different sensors for peroxisomal Ca^{2+} measurements were considered: D3cpV-px, D1cpV-px, pericam-px. All three sensors are ratiometric: they enable measurements in two wavelengths, and the ratio of intensities detected in these wavelengths correlates with the Ca^{2+} concentration and is independent of the expression level of the sensor (Pérez Koldenkova and Nagai, 2013; Sargsyan et al., 2021). The sensors cover dissociation constant (K_d) values from 0.6 µM to 60 µM (Pérez Koldenkova and Nagai, 2013) allowing rough estimation of peroxisomal Ca^{2+} concentration. The generation of the sensors and confirmation of their cellular localization with immunostaining were performed previously and are part of MD thesis of Uta Bickmeyer (for D3cpV-px) and master thesis of mine (for D1cpV-px and pericam-px) (also published in Sargsyan et al. (2021)).

To confirm the Ca^{2+}-responsiveness of the sensors, HeLa cells were transiently transfected with peroxisomally targeted GECI. Twenty-four hours after transfection, cells were permeabilized with 0.01% digitonin and the cytosol was washed out. Permeabilized cells were then exposed to 1 mM Ca^{2+} (*Figure 7*). As all three sensors have K_d values much lower than 1 mM, under these conditions the maximal response from the sensors is expected. Ca^{2+} addition resulted in drastic increase of FRET ratio in case of D3cpV-px and of 505/420 ratio in case of pericam-px. For both sensors, the detected signal increase was 1.5-fold. The increase of the signal is illustrated with false-colored images by a color look-up table (LUT) recorded before and after Ca^{2+} addition for each sensor (*Figure 7*) (Sargsyan et al., 2021). The same stimulation procedure resulted in 1.08-fold increase of FRET ratio for D1cpV-px (*Figure 7*). This much lower increase observed in case of D1cpV-px can be attributed to the properties of the sensor itself: even *in vitro* the dynamic range of D1 sensor is 1.7 (Greotti et al., 2016). Therefore, D1cpV-px was not used in the further analysis.

Next, the efficiency of D3cpV-px and pericam-px targeting to peroxisomes was studied. Drago et al. (2008) have reported high residual cytosolic signal from peroxisomal GECI due to non-efficient targeting and import of the sensor to peroxisomes. To examine the potential residual GECI signal from the cytosol in case of D3cpV-px and pericam-px, HeLa cells transfected with GECI were permeabilized with digitonin under the microscopic control (Sargsyan et al., 2021). Partial localization of sensors to the cytosol would result in signal decrease after the cytosol washout. We did not observe significant signal reductions after cytosol removal neither in cells expressing D3cpV-px nor in cells

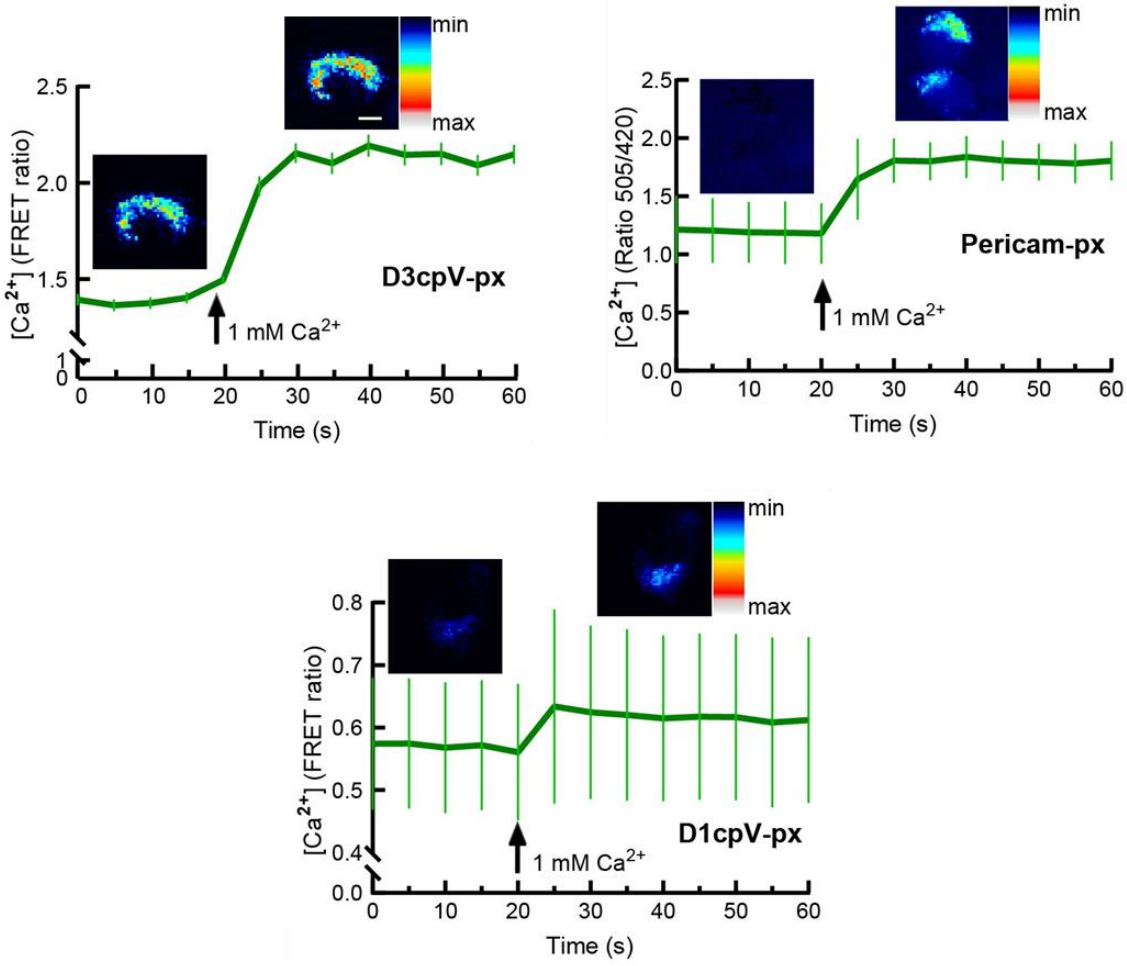

Figure 7. Peroxisomal GECI are Ca^{2+} sensitive. Addition of 1 mM Ca^{2+} to D3cpV-px, pericam-px, D1cpV-px results in ratio increase. False-colored look up tables (LUT) of HeLa cells before (left) and after (right) are shown on the corresponding parts of the curves. Data presented as mean ± standard error of the mean (SEM), n of cells from three independent experiments = 60 (D3cpV-px), 75 (pericam-px), 33 (D1cpV). Scale bar: 10 µm. Published also in Sargsyan et al. (2021).

expressing pericam-px, suggesting that the peroxisomal import of the described GECI is highly efficient (*Figure 8A*).

Further, to quantitatively confirm the localization of GECI to peroxisomes, D3cpV-px transfected HeLa cells were stained for peroxisomal enzyme catalase. The co-localization of D3cpV-px with catalase was compared to the co-localization of two peroxisomal markers, PMP70 and catalase, and showed comparable results (*Figure 8B*) (Sargsyan et al., 2021). This confirms the specificity of the used targeting signal for peroxisomes and further underlines the efficient signal detection from peroxisomes.

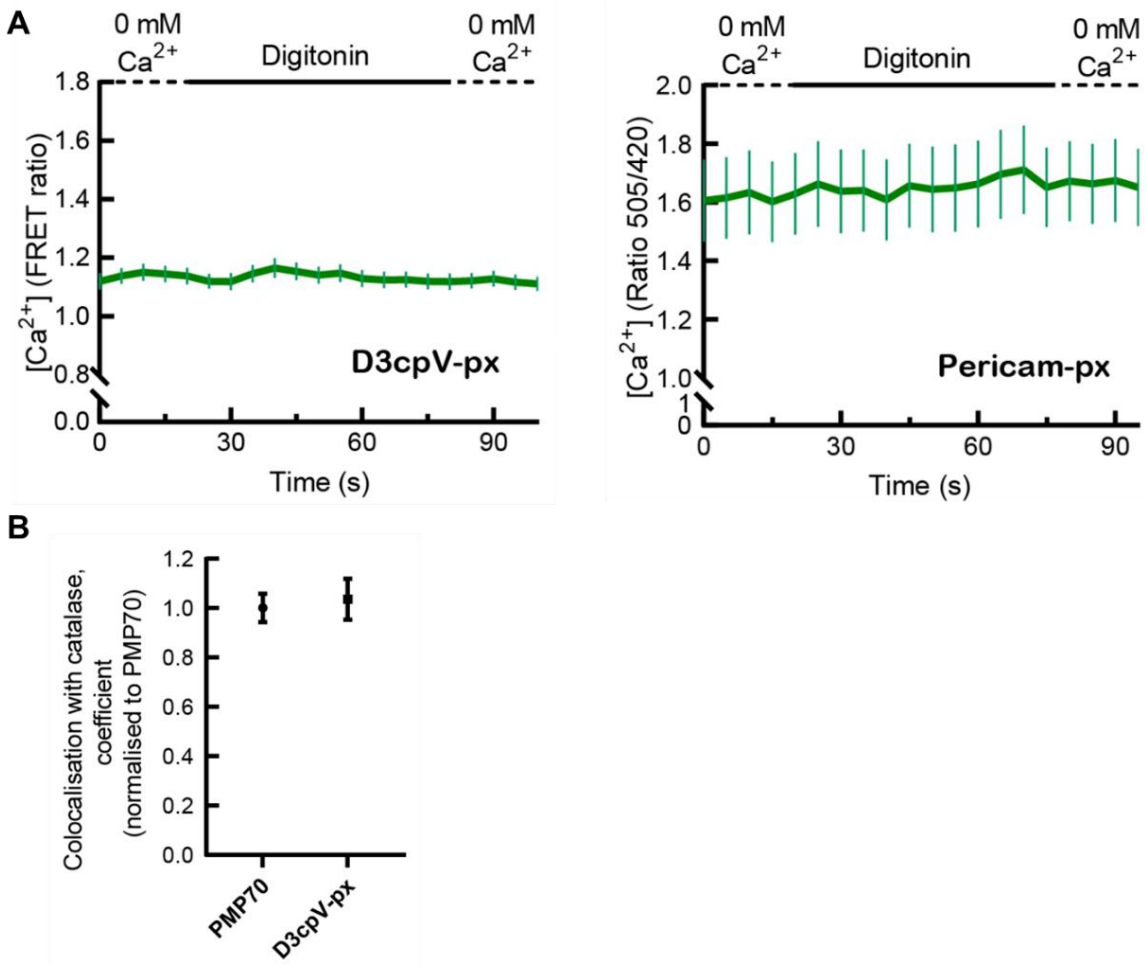

Figure 8. Peroxisomal GECI localization to peroxisomes is specific. **(A)** Measurements of D3cpV-px and pericam-px with cytosol washout do not detect signal decrease in HeLa cells. Number of cells n = 43 for D3cpV-px, = 45 for pericam-px. **(B)** Quantification of D3cpV-px co-localization with peroxisomes with Mander's co-localization coefficient normalized to PMP70 and catalase co-localization. n = 5. Data presented as mean ± SEM. Published also in Sargsyan et al. (2021).

4.1.2 pH changes and differences do not disturb peroxisomal Ca^{2+} measurements

Peroxisomal pH under physiological conditions is basic, between 7.0 and 8.0, and depending on the cell type, method used, or the research group reporting, even higher (Godinho and Schrader, 2017). Whether peroxisomal pH is also prone to changes depending on the metabolic state or cellular homeostasis is still unknown. The cytosolic pH, in contrast, is supposed to be more stable with a value of around 7.2 (Casey et al., 2010). Peroxisomal GECI contain YFP or its variants, which are known for their pH sensitivity (Young et al., 2010). The YFP component of the peroxisomal GECI may result in Ca^{2+}-independent pH sensitivity of GECI that may eventually disturb Ca^{2+} measurements. To test the range of pH at which the sensors show high stability, both in cytosol and peroxisomes, and to test if they can be used for comparison of these compartments, HeLa cells transfected with D3cpV or D3cpV-px were subjected to treatment with buffers with different pH (ranging from 7.1 to 8.0) in the presence of the proton ionophore nigericin (*Figure 9A*) (Sargsyan et al., 2021). These experiments were performed in the presence of EGTA so that the residual Ca^{2+} could be removed and only the pH changes would affect the results. As a control, cells were exposed to pH 4.0, which resulted in fast and abrupt decrease of acceptor signal due to its quenching. The GECI showed high stability of FRET ratio in the range tested. The specific modifications in D3cpV make its acceptor (YFP component cpVenus) more stable to pH than the conventional YFP (Palmer et al., 2006).

An experimental protocol for stepwise depletion of intracellular Ca^{2+} stores and SOCE to the cell through the plasma membrane (chapter 3.2.4, *Figure 6*) was developed and described for peroxisomal Ca^{2+} in the master thesis of mine and published in Sargsyan et al. (2021). This protocol is adapted from other cellular organelles (Zhao et al., 2011; Matsuda et al., 2013; Suzuki et al., 2014; Petrungaro et al., 2015).

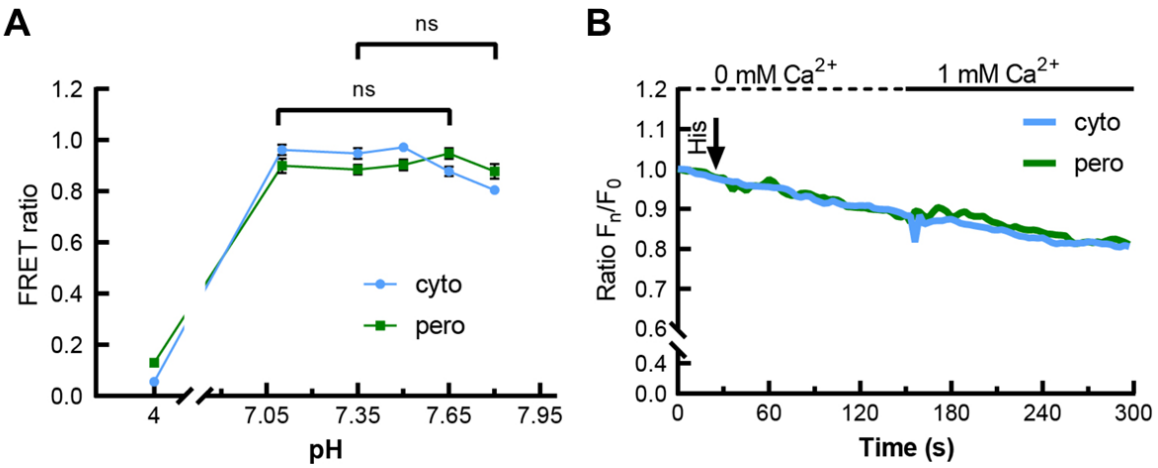

Figure 9. pH differences and changes do not affect GECI in the experimental setup. **(A)** FRET ratio measured at different pH values for D3cpV (cyto) and D3cpV-px (pero). Cells were incubated in different pH buffers containing 10 µM nigericin. Cyto and pero show comparable results at physiological pH values of cytosol and peroxisomes. pH 4 is used as control, the FRET ratio then decreases drastically due to the acceptor sensitivity. Cell numbers for cyto at pH 4 n = 51, 7.1 = 51, 7.35 = 51, 7.5 = 67, 7.65 = 48, 7.8 = 48; for pero at pH 4 n = 50, 7.1 = 50, 7.35 = 71, 7.5 = 71, 7.65 = 64, 7.8 = 64 from three independent experiments per condition. Data presented as mean ± SEM. **(B)** Effect of histamine treatment protocol on the acceptor. Neither cytosolic (cyto) nor peroxisomally (pero) targeted fluorophores undergo changes, except the fluorescence bleaching, suggesting that the pH changes during the experiment will not affect the measurement with GECIs. Data presented as mean, n = 44 (cyto), 44 (pero). Published also in Sargsyan et al. (2021).

Briefly, cell-surface localized G-protein coupled receptors are first activated by 100 µM histamine, which initiates the phospholipase C cascade. Inositol 1,4,5-trisphosphate (IP_3), the product of the cascade, binds to the IP_3 receptor on the ER membrane, triggering Ca^{2+} store release. After the signal from the initial histamine-induced response returns to basal, cells are exposed to a buffer containing 1 mM end-concentration of Ca^{2+}, leading to a second rise of intracellular Ca^{2+} (*Figure 6*).

To study whether this stimulation procedure affects the acceptor fluorophore to the extent that may disturb the measurements (e.g. due to pH variations during the experiment), the treatment protocol was first tested on HeLa cells expressing only the acceptor fluorophore (YFP and its variant) devoid of Ca^{2+}-binding sites (*Figure 9B*) (Sargsyan et al., 2021). We noticed mild YFP photobleaching over time. However, neither histamine nor 1 mM Ca^{2+}

affected the acceptor in a detectable way, suggesting that histamine treatment two-step protocol can be validly applied for analysis of Ca^{2+} handling.

4.1.3 Peroxisomal Ca^{2+} largely follows cytosolic Ca^{2+} but shows some fundamental differences

One of the main contentious points about peroxisomal Ca^{2+} in the literature is its relation and correlation with the cytosolic Ca^{2+} level (Drago et al., 2008; Lasorsa et al., 2008). Drago et al. (2008) suggest that peroxisomes strictly and passively follow cytosolic Ca^{2+} changes, whereas Lasorsa et al. (2008) propose an existence of high Ca^{2+} gradient between peroxisomes and cytosol under the resting conditions.

Therefore, we first explored cytosolic and peroxisomal Ca^{2+} responses using HeLa cells transiently expressing D3cpV or D3cpV-px (Sargsyan et al., 2021).

To compare the maximal response to Ca^{2+} from cytosol and peroxisomes, the Ca^{2+} ionophore ionomycin (Liu and Hermann, 1978) was used. Ionomycin maximally mobilizes Ca^{2+} ions from the intracellular stores and induces the PM-based uptake to the cell (Morgan and Jacob, 1994). Ionomycin treatment resulted in immediate and abrupt cytosolic Ca^{2+} increase. The peroxisomal Ca^{2+} started to increase also immediately after

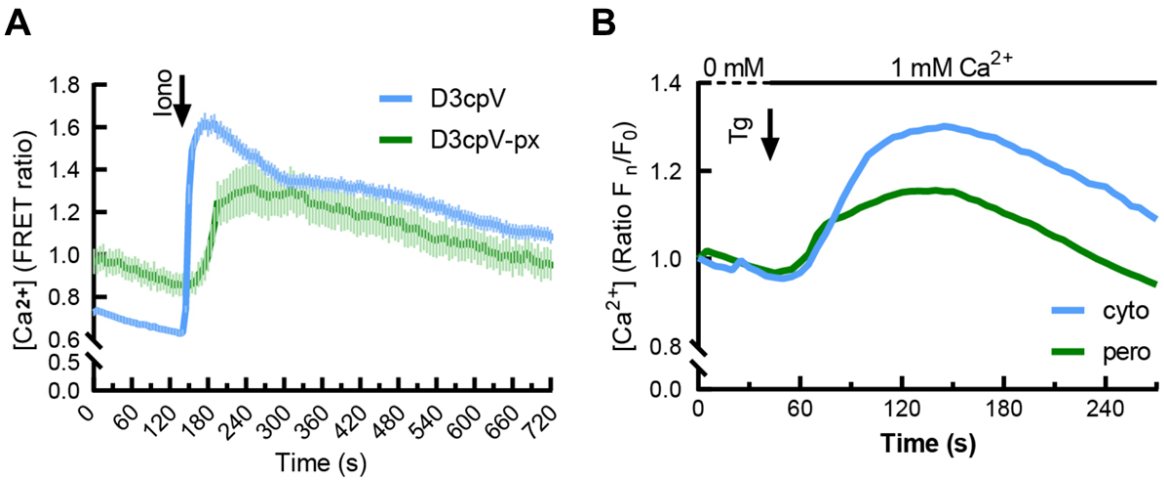

Figure 10. Comparison of peroxisomal and cytosolic Ca^{2+} handling. **(A)** Peroxisomal signal increases gradually after ionomycin (Iono) addition. Data presented as mean ± SEM, n = 16 cells for D3cpV and n = 9 cells for D3cpV-px. **(B)** Cytosolic and peroxisomal Ca^{2+} increase upon thapsigargin (Tg) treatment. The cytosolic increase is higher than the peroxisomal. Data presented as mean, n = 31 (cyto), 30 (pero). Published also in Sargsyan et al. (2021).

ionomycin addition, yet, much slower than the cytosolic response (*Figure 10A*) (Sargsyan et al., 2021). These results suggest the existence of a biological barrier between cytosol and peroxisomes and Ca^{2+} transfer mechanism other than diffusion. The slow but constant increase in peroxisomal Ca^{2+} when the cytosolic Ca^{2+} rises suggests also that the transfer mechanism may have limited transfer capacity and can be saturated.

After the peak, in the first 2 minutes the cytosolic signal decreased fast then the slope flattened so that the signal did not return to its starting basal but reached its half maximum (*Figure 10A*). The decrease of peroxisomal signal was more gradual and in 12 minutes returned to its starting values (Sargsyan et al., 2021).

To compare peroxisomal and cytosolic responses to slower and gradual increases of Ca^{2+} concentration, a milder stimulus with thapsigargin (Tg) was used (*Figure 10B*) (Sargsyan et al., 2021). Thapsigargin is a SERCA inhibitor, which in case of incubation over minutes to hours induces unfolded protein response and cell death (Sehgal et al., 2017). In the current experiment, only a short pulse of Tg was applied so that its long-term effects can be neglected. As SERCA is constantly taking Ca^{2+} back to the ER, its inhibition with Tg results in gradual accumulation of Ca^{2+} in the cytosol (Clapham, 2007). We detected gradual cytosolic and peroxisomal Ca^{2+} increase after Tg addition with a difference only in the maximum signals, suggesting that the ion transferring velocity of Ca^{2+} transfer mechanism on the peroxisomal membrane is not impaired in case of slow rise of Ca^{2+} concentration.

For a more direct kinetics comparison of cytosolic and peroxisomal Ca^{2+} handlings, a simultaneous measurement in these compartments of the same cells was performed (*Figure 11*) (Sargsyan et al., 2021). HeLa cells were co-transfected with peroxisomal D3cpV-px and cytosolic R-GECO1 sensors. R-GECO1 is a mApple-based intensiometric GECI (Zhao et al., 2011). The cells were treated according to the scheme presented in *Figure 6*. Both compartments responded with two peaks in the histamine-based two-step stimulation experiment. At each timepoint, the changes in cytosol and peroxisomes were concordant and no delay in the increasing parts of the slopes appeared (*Figure 11A*). The post-stimulation decline after the high histamine-induced peak was, however, more

prolonged and over 4-times slower in peroxisomes compared to cytosol in its linear part (*Figure 11B*). The observed slow but constant peroxisomal Ca^{2+} decline may speak for an existence of a gate from Ca^{2+} export from peroxisomes, which may be saturated under the conditions of the experiment.

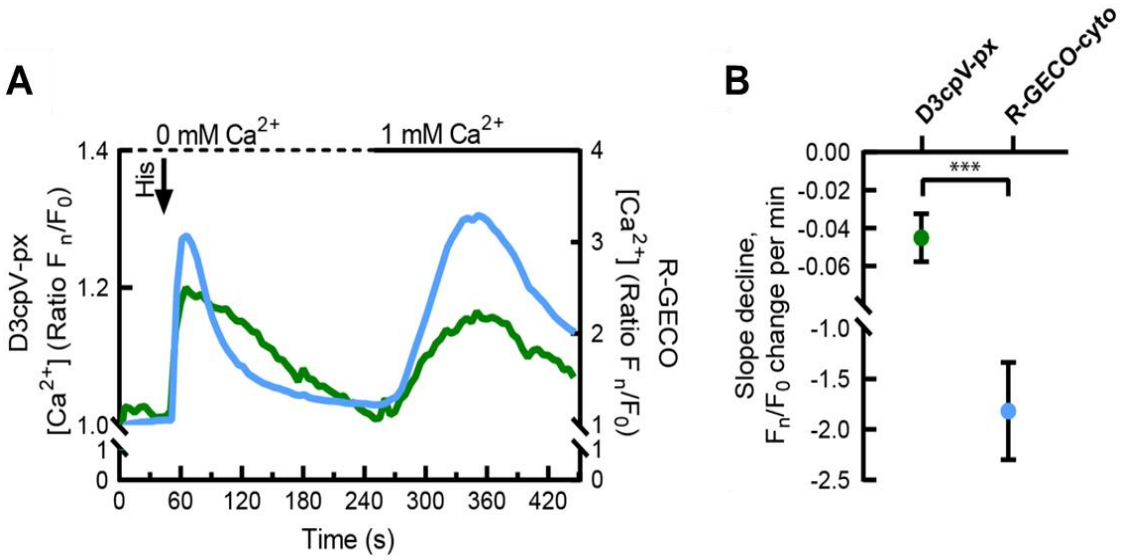

Figure 11. Simultaneous measurement of cytosolic (blue) and peroxisomal (green) Ca^{2+} reveal kinetic delay in decrease in peroxisomal signal. **(A)** Peroxisomal signal declines slower. Left y-axis: D3cpV-px (peroxisomal sensor). Right y-axis: R-GECO1 (cytosolic sensor), n = 35 cells from three experiments. **(B)** Decline of F_n/F_0 ratio per minute (min) in the linear part of the curves from (A) (from second 65 to 115). ***p < 0.001, Student's t-test. Published also in Sargsyan et al. (2021).

4.1.4 Absolute Ca^{2+} levels in peroxisomes

Previous studies on peroxisomal Ca^{2+} report extremely different Ca^{2+} concentrations in HeLa cells (Drago et al., 2008; Lasorsa et al., 2008). Drago et al. (2008) found peroxisomal Ca^{2+} levels to be similar to cytosolic levels in the steady state. At the same time, peroxisomal Ca^{2+} concentration is ~20-fold higher than in the cytosol according to Lasorsa et al. (2008).

Using the advantage of D3cpV sensor that FRET ratio correlates with Ca^{2+} concentration in µM, in this work we assessed absolute Ca^{2+} levels in peroxisomes.

Based on the FRET ratio data, calibration experiments of the FRET sensors on the imaging setup and previously determined constants, Ca^{2+} can be measured with D3cpV sensor and converted to absolute Ca^{2+} concentration (Palmer and Tsien, 2006). Here, the main focus is in peroxisomal Ca^{2+} levels under physiological and near-physiological conditions. Therefore, we treated HeLa cells transfected with D3cpV-px according to the histamine-based two-step protocol (*Figure 12A*) (Sargsyan et al., 2021). Two typical peaks were observed: a steep one after histamine addition and a more flattened one after extracellular Ca^{2+} addition.

For the calculation of absolute Ca^{2+} concentration of peroxisomes and also for the comparison of peroxisomal and cytosolic Ca^{2+} levels using the D3cpV-based sensors, an *in situ* K_d was measured in the current experimental settings based on the protocol described by Park and Palmer (2015) (*Figure 12B*). The K_d of D3cpV-px was 1.1 µM (Sargsyan et al., 2021). This is slightly higher than that of D3cpV. The basal peroxisomal Ca^{2+} levels are around 600 nM (*Figure 12C*). This is about 6 folds higher than the known cytosolic concentration (~100 nM, Paupe and Prudent, 2018). After histamine stimulation, Ca^{2+} rises in peroxisomes up to 2.4 µM.

Rarely, in some cells the basal peroxisomal Ca^{2+} was higher than 1 µM and in one cell also almost 3 µM. Some other few cells showed maximal Ca^{2+} increase over 6 µM. However, there was no correlation between the high basal value and maximal possible Ca^{2+} uptake (*Figure 12D*).

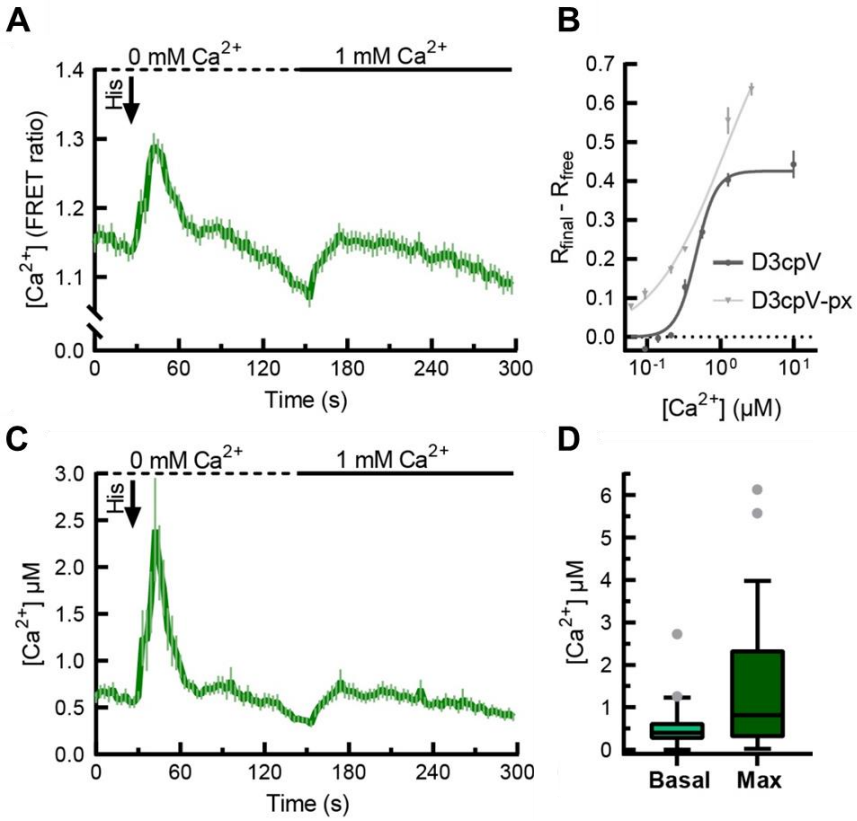

Figure 12. Absolute Ca^{2+} levels in peroxisomes range from 600 nM to 2.4 µM. **(A)** Measurement with D3cpV-px according to histamine-stimulation based design. n ≥ 50 cells from three experiments. **(B)** Absolute Ca^{2+} concentration curve calculated from the data in (A). **(C)** One-site binding model with Hill coefficient for D3cpV and D3cpV-px. The curve serves as basis for K_d calculation. **(D)** Basal and maximum (max) Ca^{2+} concentrations in peroxisomes in near-physiological states. **(A-C)** Data presented as mean ± SEM. **(D)** Data presented as Tukey's box plots. Published also in Sargsyan et al. (2021).

4.1.5 Peroxisomal Ca^{2+} shows limited similarities to mitochondrial Ca^{2+} handling

ER and PM are the main sources of intracellular Ca^{2+}. The main target organelle is mitochondria (Giorgi et al., 2018). Mitochondrial Ca^{2+} handling has been extensively studied from the perspective of its functional relevance and the molecular mechanism of Ca^{2+} transfer (De Stefani et al., 2011). Ca^{2+} regulates mitochondrial metabolism and oxidative phosphorylation, and is involved in cell death processes (Duchen, 2000; Williams et al., 2015). Since peroxisomes themselves take up Ca^{2+} when depleting intracellular stores, they are unlikely to be Ca^{2+} stores. This could mean that peroxisomes, like mitochondria, are a target organelle for intracellular Ca^{2+}.

To reveal possible similarities of mitochondrial and peroxisomal Ca^{2+} handling and directly compare peroxisomal, mitochondrial and cytosolic Ca^{2+} handlings we used the same GECI for the different compartments (Sargsyan et al., 2021). Cytosolic D3cpV, mitochondrial 4mtD3cpV and peroxisomal D3cpV-px were transfected in three sets of HeLa cells (*Figure 13*). For comparison of Ca^{2+} concentrations FRET ratios were measured. In all compartments, both, histamine treatment and exposure to Ca^{2+} containing buffer resulted in Ca^{2+} peaks (*Figure 13A*). Mitochondrial and peroxisomal basal Ca^{2+} levels were much higher than in the cytosol (*Figure 13B*). Histamine addition resulted in much higher peaks in cytosol and mitochondria (*Figure 13C*). This is in accordance with mitochondria being the main organellar target of Ca^{2+}. The rate of peroxisomal Ca^{2+} increase after histamine treatment was less than the half compared to cytosol and mitochondria, suggesting that peroxisomes under near-physiological stimuli such as histamine have limited capacity for Ca^{2+} uptake (*Figure 13D*). Peroxisomal Ca^{2+} increase after PM-based uptake to the cell was comparable to mitochondrial increase (*Figure 13E*). Altogether, these data suggest that peroxisomal Ca^{2+} handling may have limited similarities to mitochondrial Ca^{2+} handling.

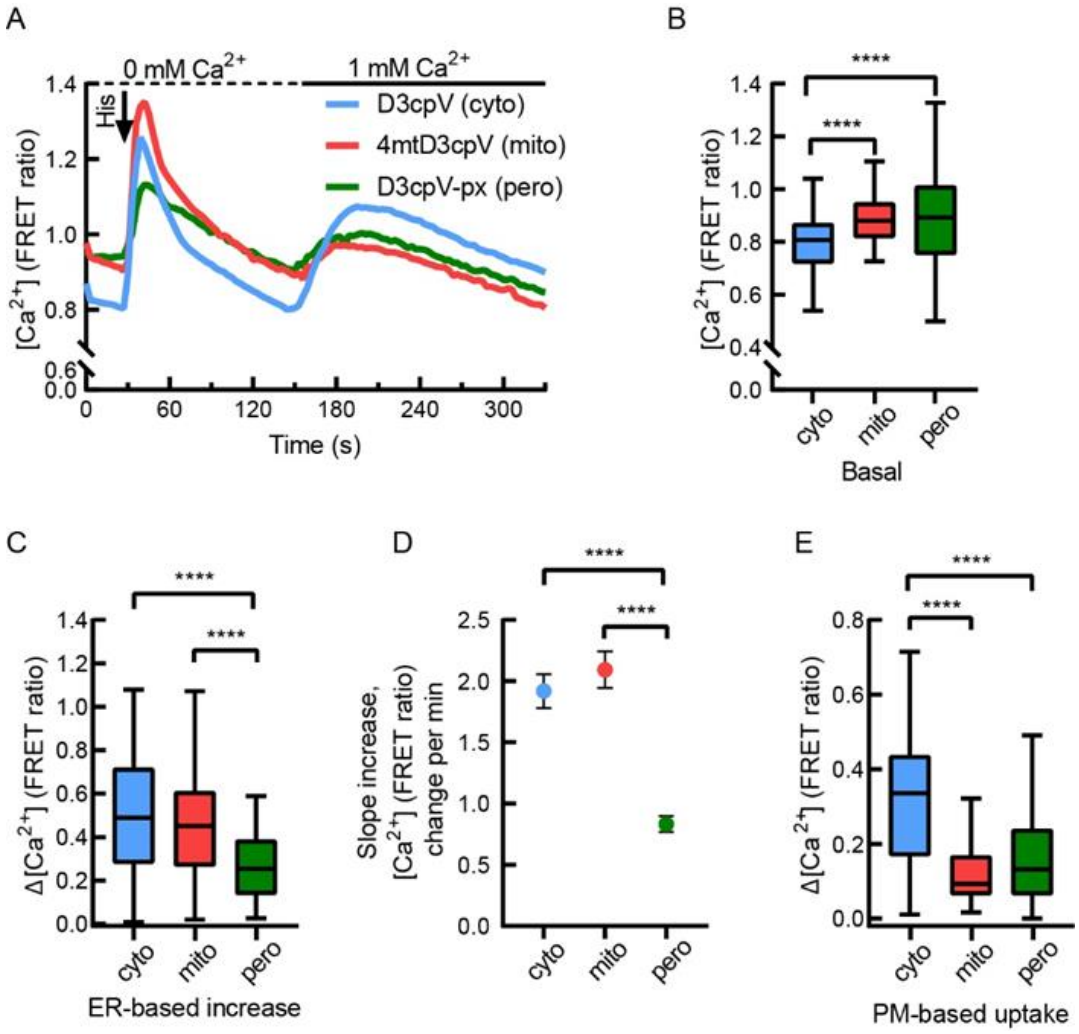

Figure 13. Peroxisomal Ca^{2+} has limited similarities with mitochondrial Ca^{2+} handling. **(A)** Cytosolic, mitochondrial and peroxisomal Ca^{2+} responses measured with consequent additions of histamine and extracellular Ca^{2+}. **(B)** Basal levels of Ca^{2+} in peroxisomes are similar to mitochondria. Analysis based on the data from (A). **(C)** Peroxisomal Ca^{2+} increase upon ER-store depletion is smaller than that of cytosol or mitochondria. Analysis based on the data from (A). **(D)** Peroxisomal signal is rising slower. Increase of FRET ratio per minute (min) in the linear part of the curves in (A) (from second 27 to 42). Data presented as mean ± SEM. **(E)** Peroxisomal Ca^{2+} increase upon PM-based cellular uptake of Ca^{2+} is comparable to mitochondria. Analysis based on the data from (A). **(B-E)** One-way ANOVA followed by Tukey's post hoc test. ****$p < 0.0001$, Cyto: cytosolic, mito: mitochondrial, pero: peroxisomal. n = 83 (cyto), = 116 (mito), = 117 (pero) cells from six independent experiments. **(B, C, E)** Data presented as Tukey's box plots. Published also in Sargsyan et al. (2021).

.

4.1.6 Peroxisomal LDHBx overexpression increases stimulated peroxisomal Ca^{2+} uptake

Ca^{2+} is involved in upregulation of the monocarboxylate transporters, which are responsible for lactate and pyruvate trafficking across membranes (Halestrap and Wilson, 2012). Their presence was also suggested on peroxisomal membrane where they may serve as essential players of the elusive peroxisomal lactate shuttle to enable β-oxidation (McClelland et al., 2003). Peroxisomal β-oxidation requires constant supply of NAD^+ (Wanders et al., 2015). This demand can be met by the re-oxidation of NADH through the LDHBx enzyme – a reaction that produces also lactate. Lactate is then exiting peroxisomes as a product of the reaction (McClelland et al., 2003).

To test if peroxisomal LDHBx activity may play a role in peroxisomal Ca^{2+} handling, HeLa cells were transfected with peroxisomal LDHBx (first stop codon is mutated to TGG, so that 100% readthrough happens) with an EBFP-tag, and D3cpV-px. The cells with positive EBFP signal were then subjected to the histamine-based two-step stimulation (*Figure 14A*). Mock transfected cells were used as control. Though there were no changes in the basal levels observed (*Figure 14B*), the ER-based (*Figure 14C*) and PM-based uptakes (*Figure 14D*) increased significantly in the LDHBx expressing sample. These results suggest that LDHBx activity may stimulate peroxisomal Ca^{2+} uptake.

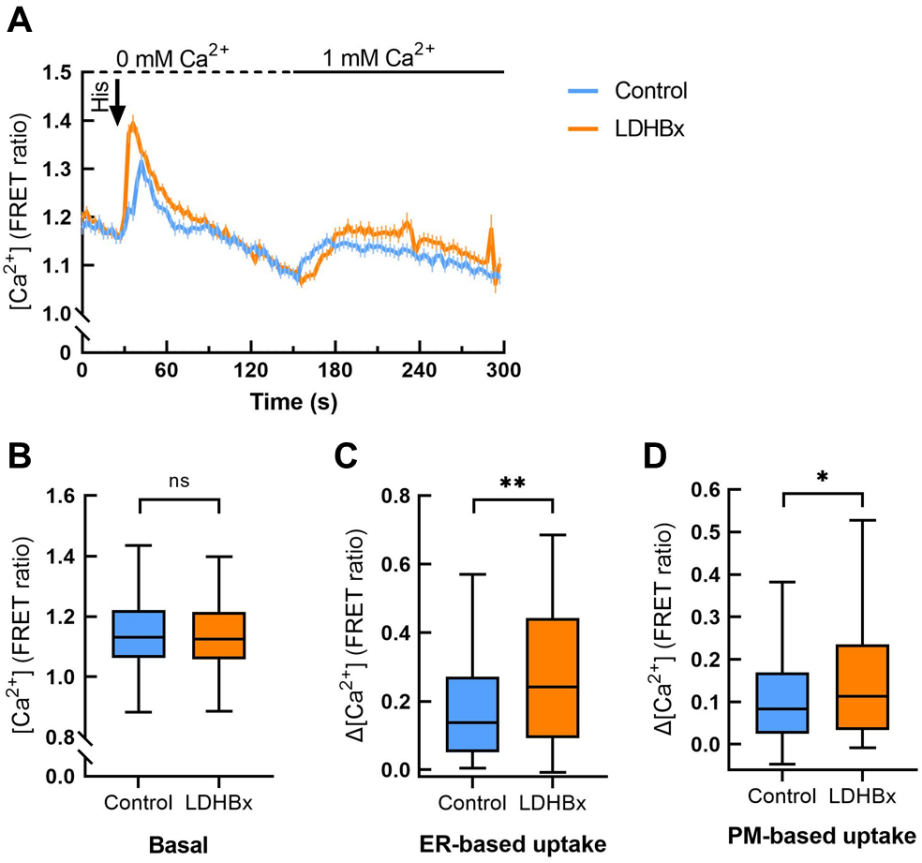

Figure 14. LDHBx overexpression (OE) increases peroxisomal Ca^{2+} uptake. **(A)** Comparison of peroxisomal LDHBx OE (LDHBx) cells with the mock transfected cells (control) in histamine stimulated Ca^{2+} measurement. Data presented as mean ± SEM. **(B)** Basal levels are not affected. Data analyzed based on (A). **(C)** LDHBx results in increased ER-based Ca^{2+} uptake compared to the control. Analysis based on (A). **(D)** PM-based uptake is significantly increased in LDHBx OE cells. Analysis based on data from (A). n = 116 (LDHBx), = 78 (control) from three (control) and four (LDHBx) experiments. * $p \leq 0.05$, ** $p \leq 0.01$, Student's t test. **(B-D)** Quantifications presented as Tukey's boxplot.

4.2 Peroxisomal Ca^{2+} handling in cardiomyocytes

4.2.1 Establishment of a protocol for peroxisomal Ca^{2+} measurements in CMs and Ca^{2+} measurements in CMs

Ca^{2+} handling in excitable cells, such as cardiomyocytes, differs from that of non-excitable cells. Although in cardiomyocytes the main sites are the ER/SR and the PM, the stimuli used to induce Ca^{2+} entry to the cell in reproducible manner cannot be the same (Chapman, 1979). To test whether Ca^{2+} can enter peroxisomes in cardiomyocytes three different stimuli were tested in iPSC-CMs. We used subsequent additions of 10 mM caffeine, 0.5 µM ryanodine, and 1 µM Tg in increasing concentrations of Ca^{2+} buffer (*Figure 15A*). Caffeine (Caf) reduces the threshold of RyR2 activation by Ca^{2+} and results in Ca^{2+} release from the ER (Kong et al., 2008). Ryanodine (Ry) may act as inhibitor or activator of RyR depending on its concentration (Van Petegem, 2012). At nanomolar concentrations, it keeps the RyR channel in an half-open state, at concentrations higher than 100 µM Ry acts as a RyR inhibitor (Van Petegem, 2012). Here, Ry is used for stimulation of Ca^{2+} accumulation in the cytoplasm. All three stimuli resulted in peroxisomal Ca^{2+} increase. Caf interacts, however, with several Ca^{2+} indicator dyes (Muschol et al., 1999) and a potential interaction with GECI could not be excluded. Hence, Caf was omitted from further analysis.

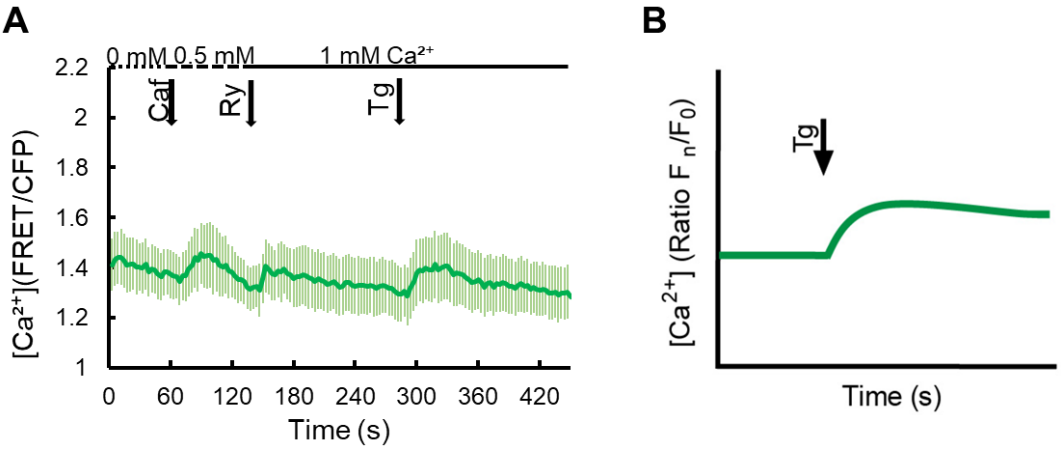

Figure 15. Experimental design for Ca^{2+} measurements in CMs **(A)** Peroxisomal calcium increases in iPSC-CMs upon caffeine (Caf), low-concentration ryanodine (Ry), and thapsigargin (Tg) stimulation. **(B)** One-step simplified protocol for Ca^{2+} measurements in CMs. Some of these data have been published in Sargsyan et al. (2021)

The peak after Ry was rather low. Further adjustments of its concentrations may result in contrary effects due to the dependence of Ry effect on its concentration. Therefore, the experimental paradigm was reduced to one-step stimulation of cells with Tg (*Figure 15B*). As SERCA is a ubiquitous pump that transports Ca^{2+} to the ER in all eukaryotic cells (Primeau et al., 2018), this protocol can be also applied when measuring peroxisomal Ca^{2+} in other excitable and non-excitable cells (Sargsyan et al., 2021).

The simplified one-step experiments were used to confirm cytosolic Ca^{2+} increase and study Ca^{2+} entry to peroxisomes in NRCMs and hiPSC-CMs by Uta Bickmeyer (thesis and Sargsyan et al. (2021)) (*Figure 16*). To exclude the effects of cell movements during addition of Tg and spontaneous contractions, cells were pre-treated with 2,3-butanedione monoxime (Gwathmey et al., 1991). After confirming that Tg addition with 1 mM Ca^{2+} results in cytosolic Ca^{2+} increase in the cells using cytosolic GECI, cells expressing peroxisomal D3cpV-px were treated with the same protocol. Both in NRCMs (*Figure 16A-C*) and hiPSC-CMs (*Figure 16D-F*) peroxisomal Ca^{2+} increases after Tg treatment, showing that peroxisomes in cardiomyocytes take up Ca^{2+} when cytosolic Ca^{2+} rises. These also suggest that peroxisomal Ca^{2+} may increase in the excitation process of the CMs when a drastic increase of cytosolic Ca^{2+} is observed.

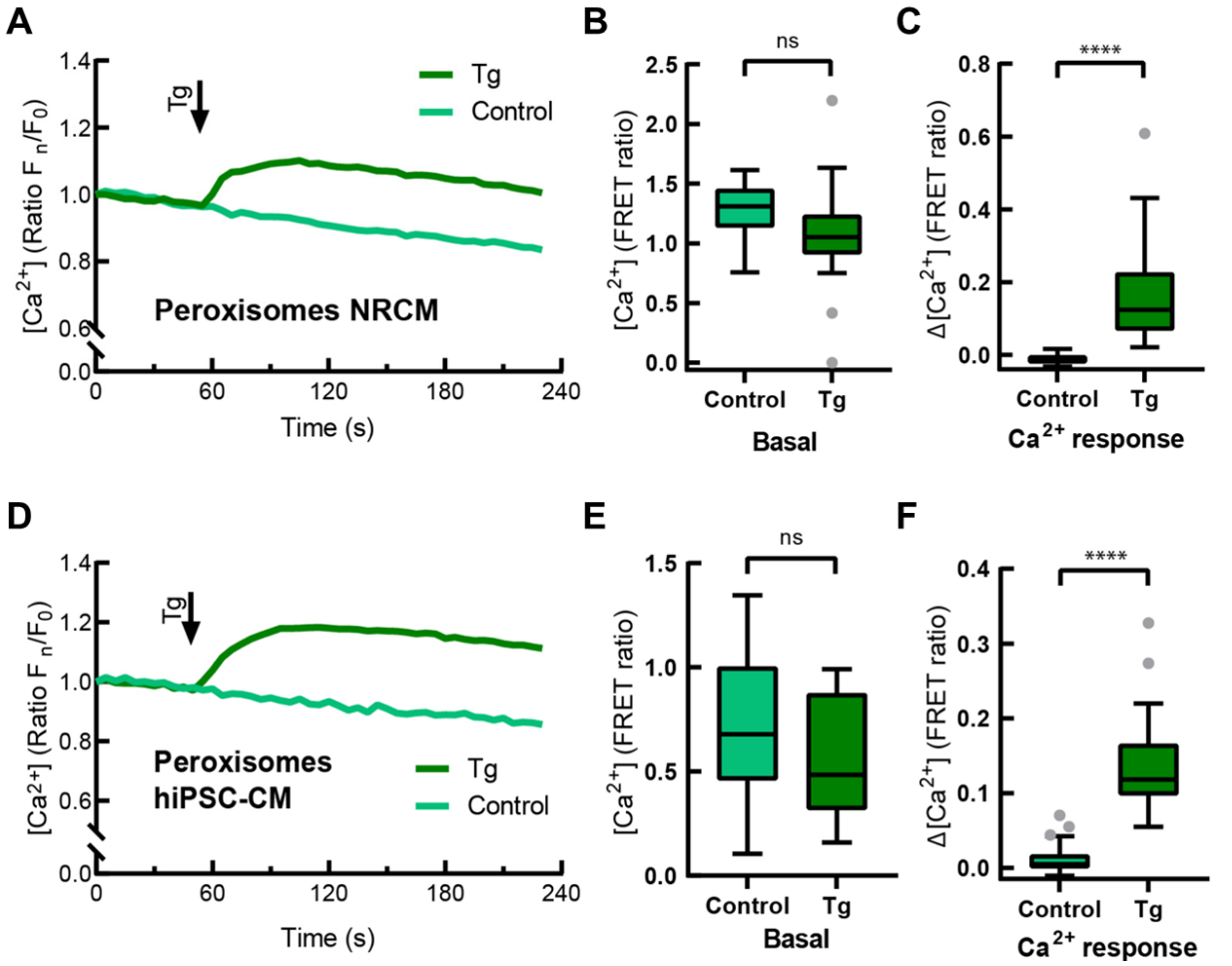

Figure 16. Peroxisomal Ca^{2+} increases in CMs upon Tg treatment. **(A)** Peroxisomal Ca^{2+} measurement in NRCMs following the one-step Tg treatment experimental design. Addition of Tg is compared to the addition of Tg-free buffer (control), n = 20 (Tg), 31 (control) from three experiments. **(B)** Basal levels of Ca^{2+} are not different before the treatment in (A). **(C)** Peroxisomal Ca^{2+} increases after Tg addition in (A). **(D)** Peroxisomal Ca^{2+} measurement in hiPSC-CMs with D3cpV-px following the experimental design in *Figure 15B* for excitable cells similarly performed as in (A). Addition of Tg is compared to the addition of Tg-free buffer (control). n = 26 (Tg), 33 (control) from three experiments. **(E)** Basal levels of Ca^{2+} are not different before the treatment in (D). **(F)** Peroxisomal Ca^{2+} increases after Tg addition in (D). **(A, D)** Data presented as means. Unpaired Student's t-test. ****p < 0.0001, Tukey's box plots. Some of these data are parts of MD thesis of Uta Bickmeyer and are published in Sargsyan et al. (2021).

4.2.2 Peroxisomal Ca^{2+} in NRCMs rises upon stimulation with Tg

NRCM and iPSC-CM experiments described in the previous section were performed on cells transfected with DNA plasmids using a chemical transfection method. The transfection efficiency was less than 20% and varied depending on the time of transfection and the age of the cells. To achieve higher transfection efficiency which would allow larger scale experiments and enable electrophysiological studies of the cells, viral transfection with D3cpV-px under cardiac troponin T promoter in AAV6 virus was used. In freshly isolated NRCMs the transfection efficiency was higher than 70%. The cells were then subjected to one-step addition of Tg in 1 mM Ca^{2+} buffer (*Figure 17*).

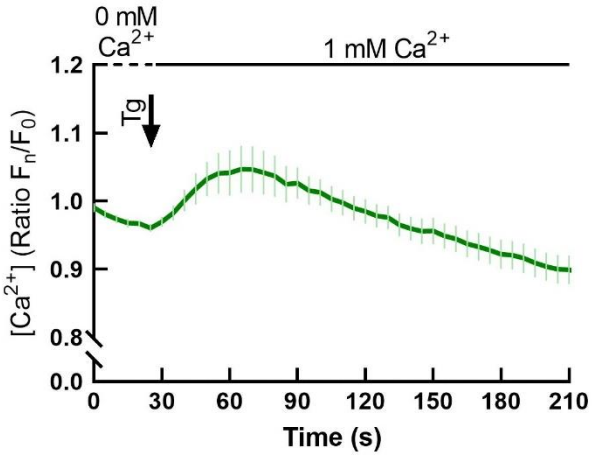

Figure 17. Peroxisomal Ca^{2+} in NRCM rises upon Tg treatment of cells. Peroxisomal Ca^{2+} measurement in NRCMs expressing AAV6-ssTnT-D3cpv-PTS1 following the one-step Tg treatment experimental design from *Figure 15B*. Number of cells n = 8 from three experiments. Data presented as mean ± SEM.

There was a notable bleaching of the acceptor fluorophore seen that results in the decreasing ratio. Still, after Tg treatment peroxisomal Ca^{2+} increased confirming that the AAV6 construct of GECI is Ca^{2+} sensitive and can be potentially used for more complex experiments after some adjustments of excitation parameters.

4.3 Analysis of peroxisome morphology and contacts

4.3.1 Peroxisomes occasionally contact RyR in hiPSC-CMs

The two-step protocol where ER and PM are stimulated subsequently gives information about the level of contribution of each component to peroxisomal Ca^{2+}. The one-step Tg treatment, in contrast, does not give information about the source of Ca^{2+} that enters peroxisomes.

To get the first insight whether the PM or the SR is the main source of peroxisomal Ca^{2+} in CMs, a series of stainings of peroxisomes and D3cpV-px with the LTCC and the RyR in hiPSC-CMs were performed (*Figure 18*) (Sargsyan et al., 2021). In several cases peroxisomes (stained with anti-Pex14 antibody) and peroxisomal GECI are in close proximity to the LTCC (*Figure 18A*). However, more often proximity of peroxisomes and D3cpV-px was found with RyR (*Figure 18B*). These suggests that the spatial position of peroxisomes in the cells may enable them to take up Ca^{2+} both from SR and PM, but, based on these findings, it can be speculated that the SR plays a more important role.

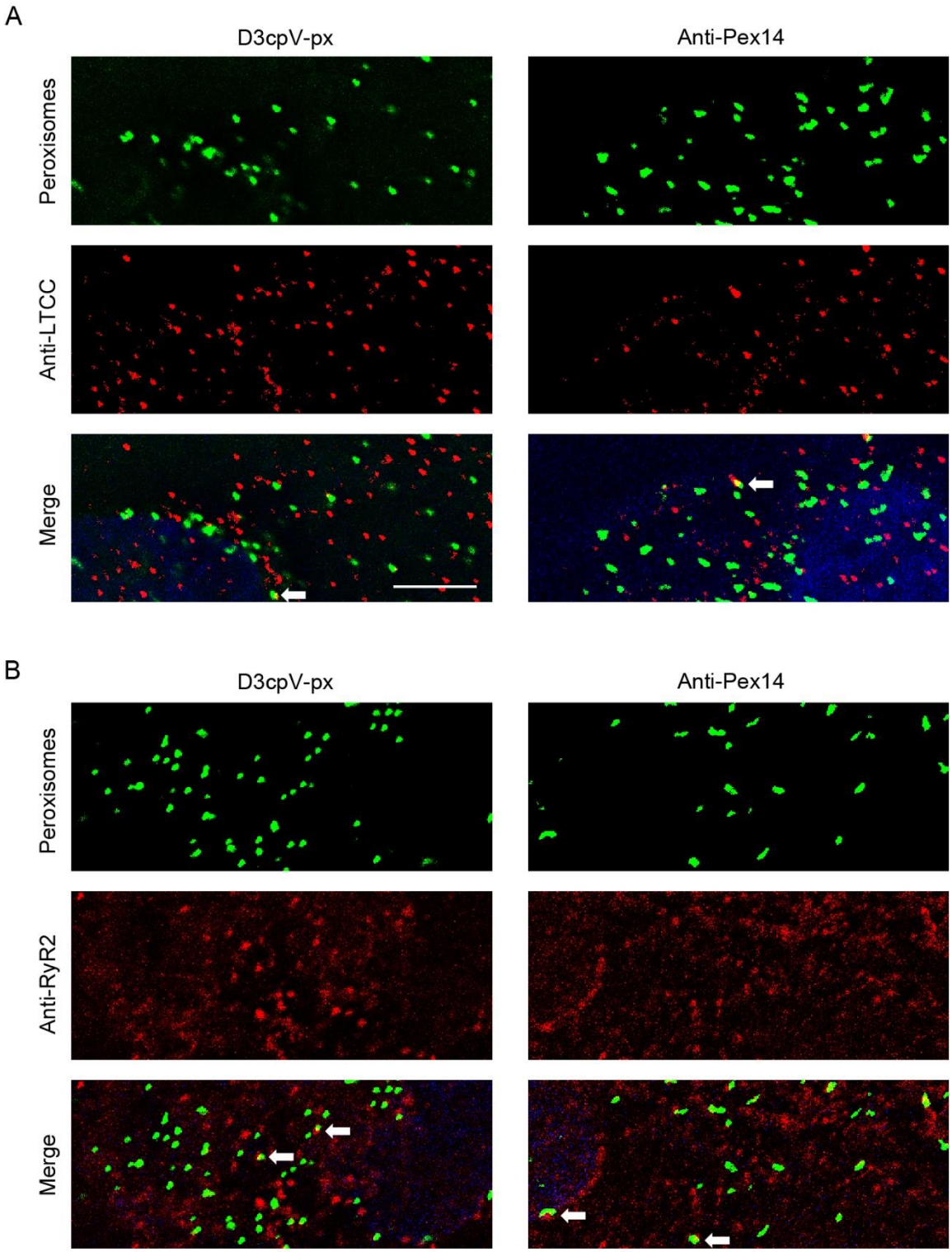

Figure 18. Relative localization of peroxisomes and Ca^{2+} channels in hiPSC-CMs. hiPSC-CMs were either transfected with D3cpV-px (left panels) or stained with anti-Pex14 (right panels) as a peroxisomal marker. **(A)** Representative images from staining of L-type Ca^{2+} channel (LTCC) show some proximity of peroxisomes and LTCC. **(B)** Representative images from staining of ryanodine receptor (RyR2) show more often contact of peroxisomes with the RyR2. Scale bar 5 µm. Published also in Sargsyan et al. (2021).

4.3.2 Large fraction of peroxisomes contacts RyR2 in isolated mice cardiomyocytes

Although hiPSC-CMs largely lack the sarcomere striation pattern typical for mature adult CM (Zuppinger et al., 2017), they are a potent research tool. The lack of the striation, however, may affect SR structure and organization (Zhang et al., 2013; Kim et al., 2015; Koivumäki et al., 2018). To deeper analyze the role of PM and SR proximity to peroxisomes in mature adult cardiomyocytes, peroxisomes and caveolin 3 (Cav3) or RyR2 were stained in freshly isolated mice cardiomyocytes (isolation and stainings contributed by Julia Hofhuis) (*Figure 19*). The images were taken with confocal microscope and the proximity was analyzed according to Valm et al. (2017). Around 80% of peroxisomes are

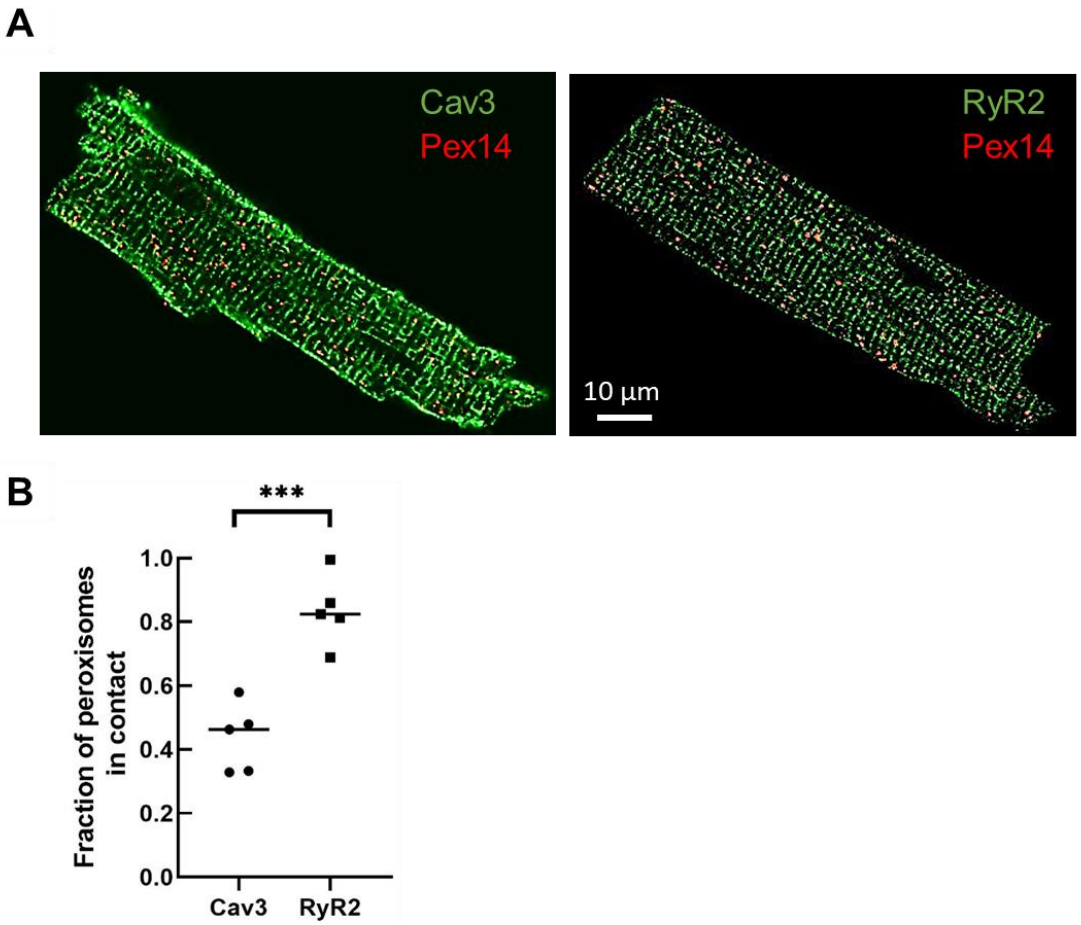

Figure 19. Peroxisomes in isolated heart CMs communicate more with RyR than with Cav3. **(A)** Representative images of immunostainings with anti-Pex14 and anti-Cav3 or anti-RyR2 antibodies. **(B)** Contact analysis according Valm et al., (2017). Data presented as mean ± SEM, ***p < 0.001. Student's t test.

contacting RyR2 (*Figure 19B*), suggesting that the intracellular Ca^{2+} stores may serve as a main contributor of peroxisomal Ca^{2+} in CMs.

Functional peroxisomes in wild type (WT) CMs appear elongated and clearly show a lumen when imaged with stimulated emission depletion (STED) microscopy. In case of the absence of peroxisomal protein import (Pex5-KO) peroxisomes appear rounded and no lumen can be detected using STED (*Figure 20*).

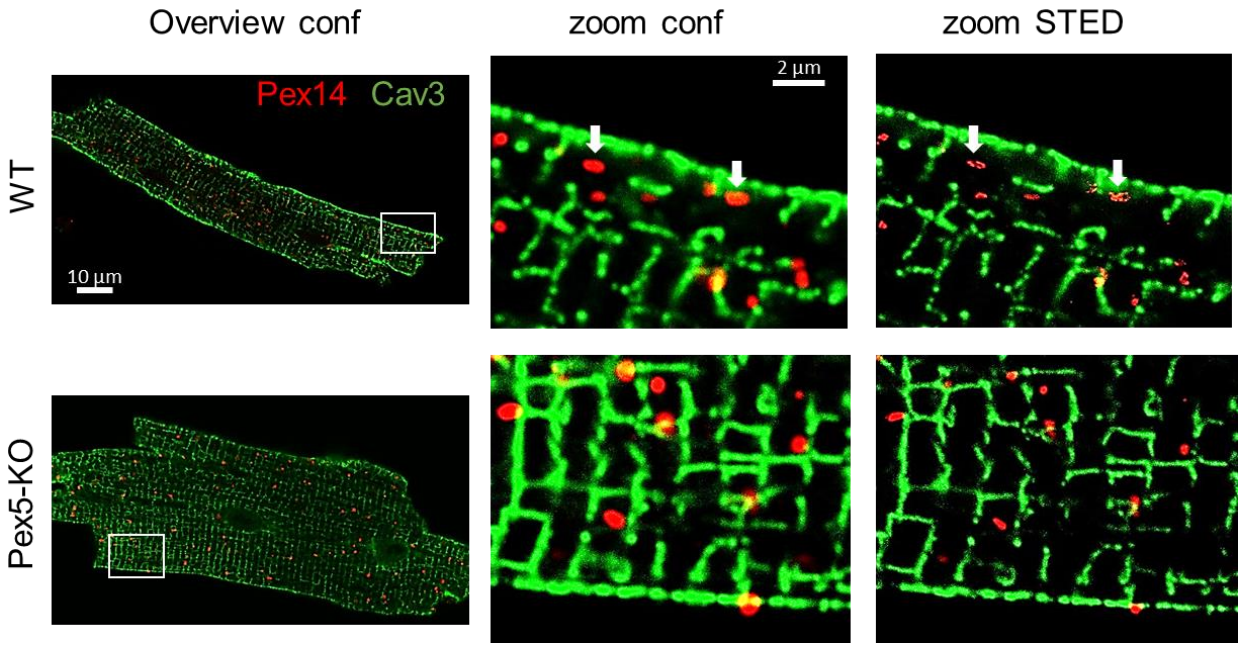

Figure 20. STED microscopy reveals fine structure of peroxisomes in CMs. Peroxisome lumen is seen only with STED microscope (white arrows), making the differences between WT and KO peroxisomes obvious. Representative images of immunostainings in wild type (WT) and peroxisome deficient (Pex5-KO) CMs stained with anti-Pex14 and anti-Cav3 antibodies. The white rectangles in the overview confocal (conf) images mark the fields shown in zoom.

Peroxisome morphology parameters size, solidity and roundness were analyzed based on the confocal and STED images and compared with each other (*Figure 21*). Peroxisomes were found to be less than half in size when imaged with STED (~0.07 µm² versus ~0.2 µm² with STED and confocal, respectively) (*Figure 21A*). Furthermore, when analyzed with STED, the solidity and roundness differed between WT and KO cells (*Figure 21B-C*), suggesting that fine peroxisome morphology can be better studied with STED

microscopy. The peroxisome morphology parameter analysis established and used for the fluorescent image analysis here can be applied in study of peroxisomes in any other tissue and cell type.

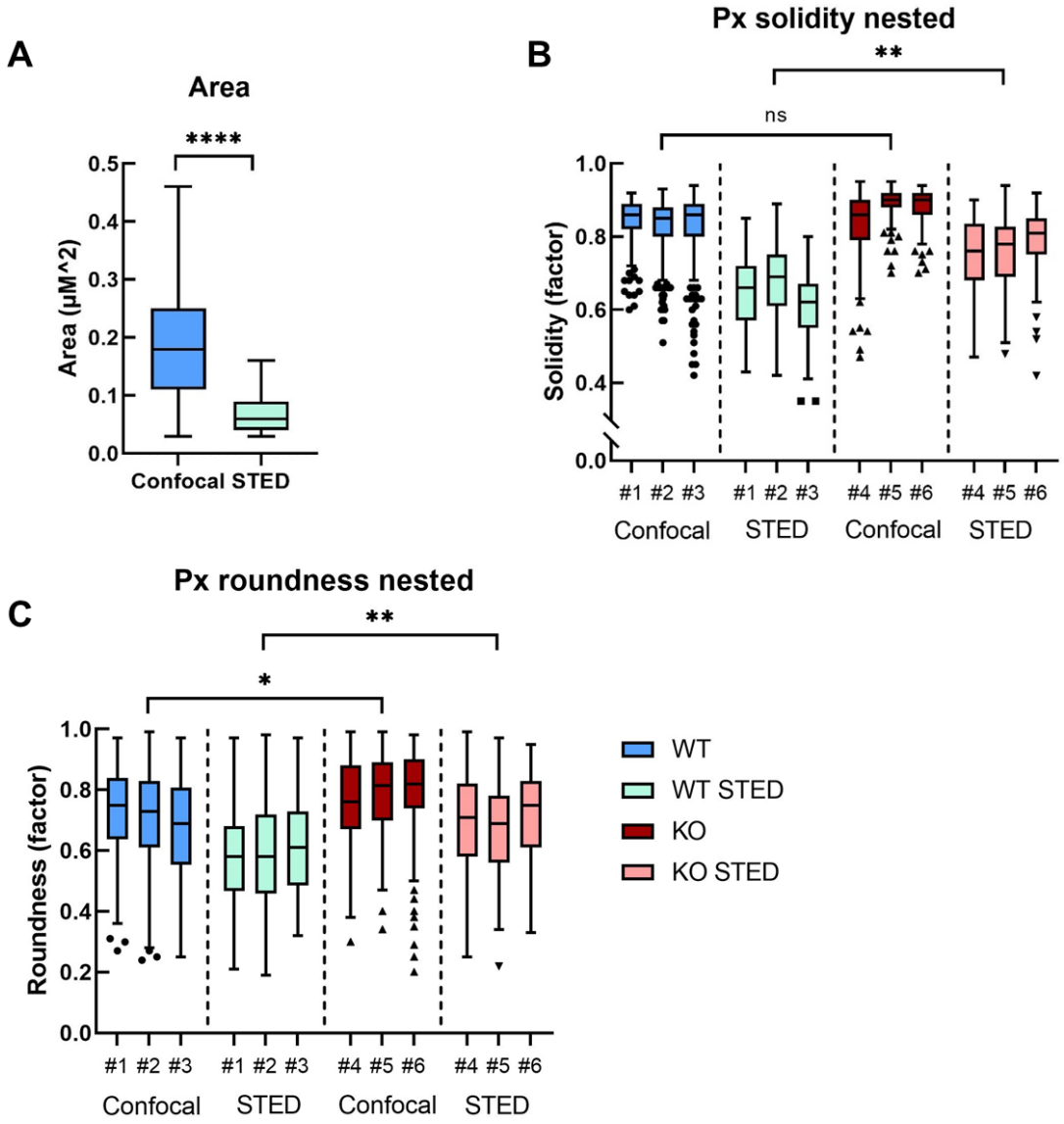

Figure 21. Super resolution microscopy (here STED) enables fine characterization of peroxisome morphology and its quantification. Data presented as Tukey's box plots. * $p \leq 0.05$, ** $p \leq 0.01$, **** $p \leq 0.0001$. **(A)** Student's T-test. **(B, C)** Nested ANOVA analysis.

4.3.3 *PEX10*-deficiency in patient fibroblasts results in prominent cellular mosaicism

Some pathogenic variants of *PEX10* are characterized with severe clinics and complete absence of functional peroxisomes in fibroblasts (Warren et al., 1998). Others result in milder presentation of the disease with later onset and mosaic cells with either normal or disturbed functional peroxisome number (Régal et al., 2010; Yamashita et al., 2017). Applying the methodology established and described in 4.3.2, the peroxisomal morphology and number for precise characterization of mosaicism are quantitatively analyzed. To that purpose, patient fibroblasts that show cellular mosaicism were used (*Figure 22*). In some cells catalase showed only punctate localization. In others, widespread homogeneous cytosolic catalase with sometimes concentrated punctate catalase was found. First, the residual cytosolic catalase was quantified on the images (*Figure 23A*). The results from the patient were compared to the control fibroblasts from a proband. The *PEX10* deficient fibroblasts have almost 70% more cytosolic catalase than the healthy control fibroblasts.

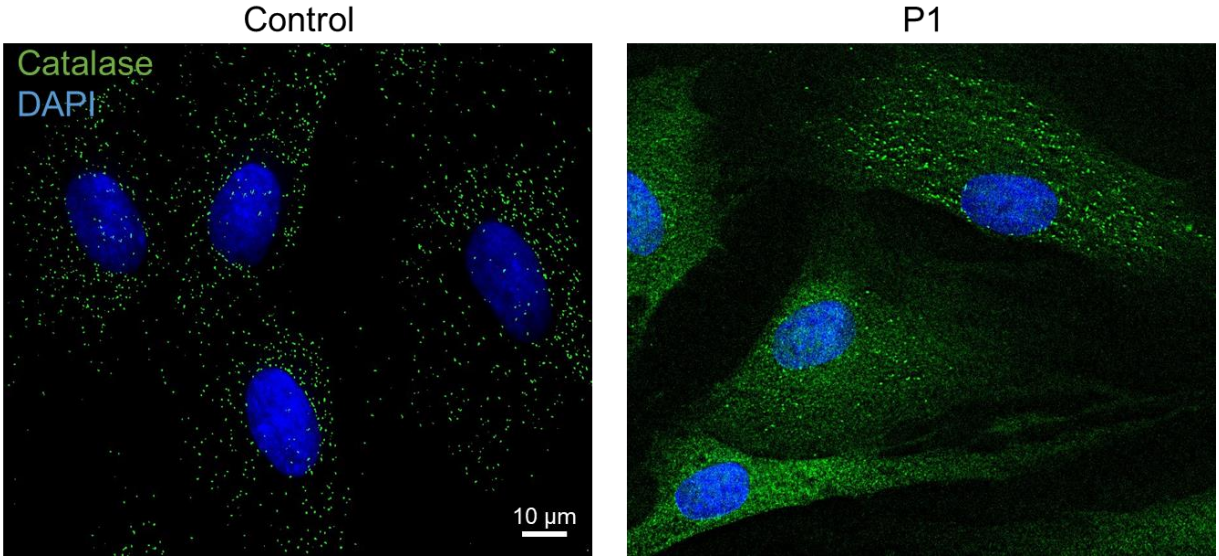

Figure 22. Patient fibroblasts present with cellular mosaicism. Representative control cells and patient cells (P1) immunostained with an anti-catalase antibody (green). Control fibroblasts show punctate catalase pattern. P1 fibroblasts show cellular mosaicism regarding catalase distribution with absence and presence of punctate catalase. Generally, more background cytosolic catalase signal is seen in P1.

Then, the functional peroxisome number and morphology were studied in patient and control fibroblasts (*Figure 23B-E*). Less peroxisomes were found in the patient cells (*Figure 23B*). The size of the existing peroxisomes was, however, unaffected (*Figure 23C*). Furthermore, patient peroxisomes are less round and appear more elongated (*Figure 23D-E*). The elongation of peroxisomes may be a sign of affected peroxisome division (Smith and Aitchison, 2013). On the other side, elongated shape of peroxisomes

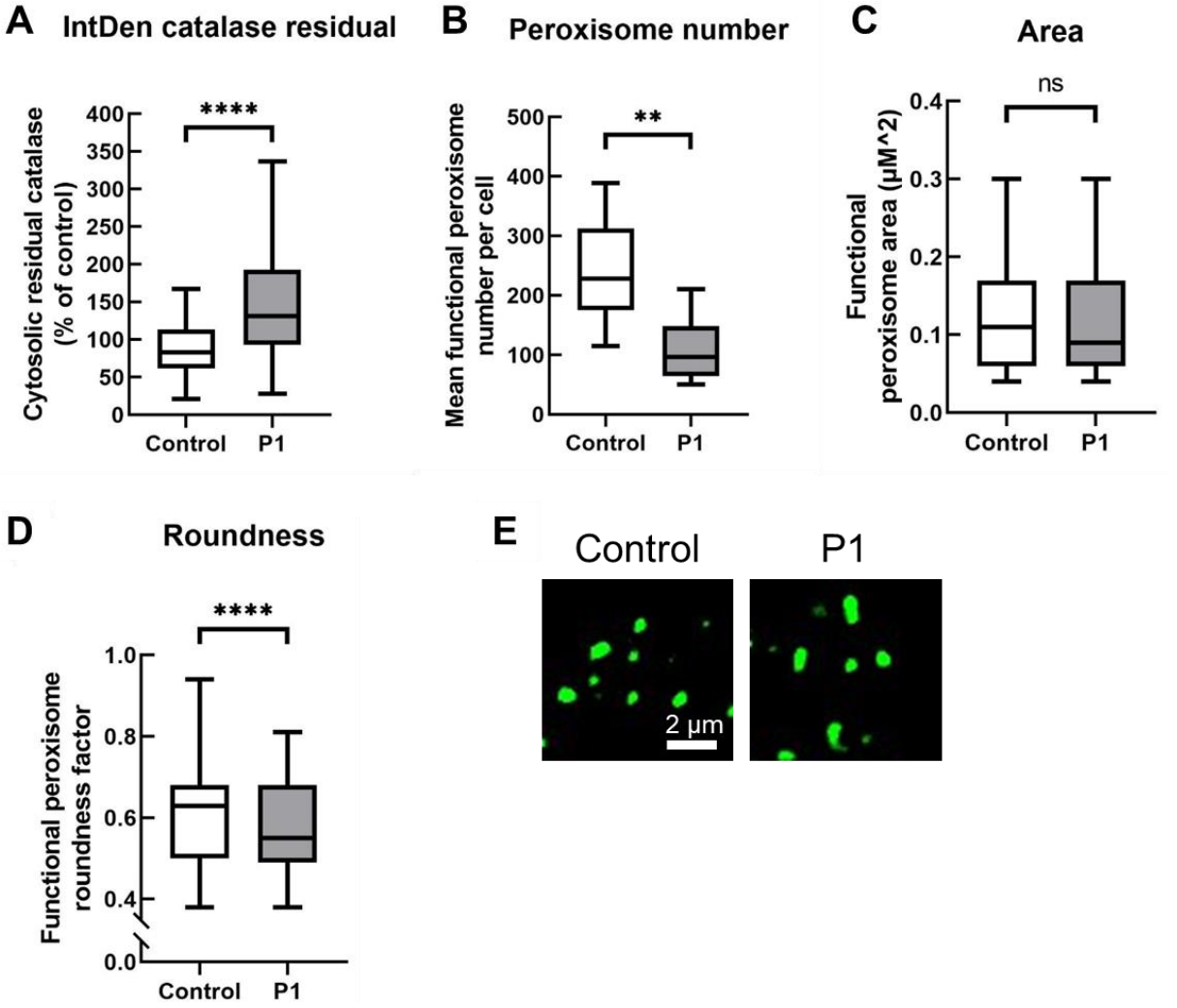

Figure 23. (A) Cytosolic residual catalase is much higher in patient (P1) cells than in the control. Number of cells analysed n = 103 (Control), = 85 (P1). **(B-E)** Catalase-positive peroxisome number and morphology analysis in control and P1 fibroblasts. **(B)** Functional peroxisome number per cell is reduced in P1 fibroblasts. **(C)** Peroxisome area (size) is not altered in P1 cells. **(D)** P1 peroxisomes are less round (more elongated) than the control peroxisomes. **(E)** Representative image of control and P1 peroxisomes. **(A-D)** Data presented as boxplots; whiskers cover values from 10th to 90th percentile. **p < 0.01, ****p < 0.0001, Student's t test.

without their size change can be a result of affected peroxisome-ER contacts (Costello et al., 2017a; Hua et al., 2017) which in turn may affect Ca^{2+} transport from the ER to peroxisome in case the MCS plays a role in this transport.

4.4 ER-peroxisome tethering through ACBD5 and its role in Ca^{2+} transport

4.4.1 ACBD5-deficient cells have abnormal peroxisomal Ca^{2+} handling

It is known from mitochondrial Ca^{2+} homeostasis that ER-mitochondria proximity and tethering are essential for efficient Ca^{2+} transfer from ER to mitochondria (Hirabayashi et al., 2017). Due to the proximity of peroxisomes to Ca^{2+}-handling sites in cardiomyocytes, ER-peroxisome tethering was assessed for Ca^{2+} trafficking to peroxisomes. To test this, HeLa cells lacking ACBD5 due to a mutation in *ACBD5* gene (Ferdinandusse et al., 2017) were subjected to peroxisomal Ca^{2+} measurement with D3cpV-px with histamine treatment (*Figure 24A*). Two cell lines generated with CRISPR system and bearing the same mutation, crACBD5-1 and crACBD5-5, were analyzed in comparison with their wild-type HeLa cells as control. The growth rate of crACBD5-5 was very low, and the growing pattern and phenotype of crACBD5-5 were different from crACBD5-1 and from control at the time of experiment, so a reliable comparison between crACBD5-5 and crACBD5-1 or crACBD5-5 and control did not seem possible. The results from all three cell lines are presented in *Figure 24*. There were no differences detected between the basal levels of the cells (*Figure 24B*). CrACBD5-1 showed lower ER-based increase compared to the control (*Figure 24C*), with the unaffected PM-based uptake (*Figure 24D*). The crACBD5-5 cell line behaved as the control after the histamine addition (*Figure 24C*), however, showed increased PM-based uptake upon extracellular Ca^{2+} accessibility (*Figure 24D*).

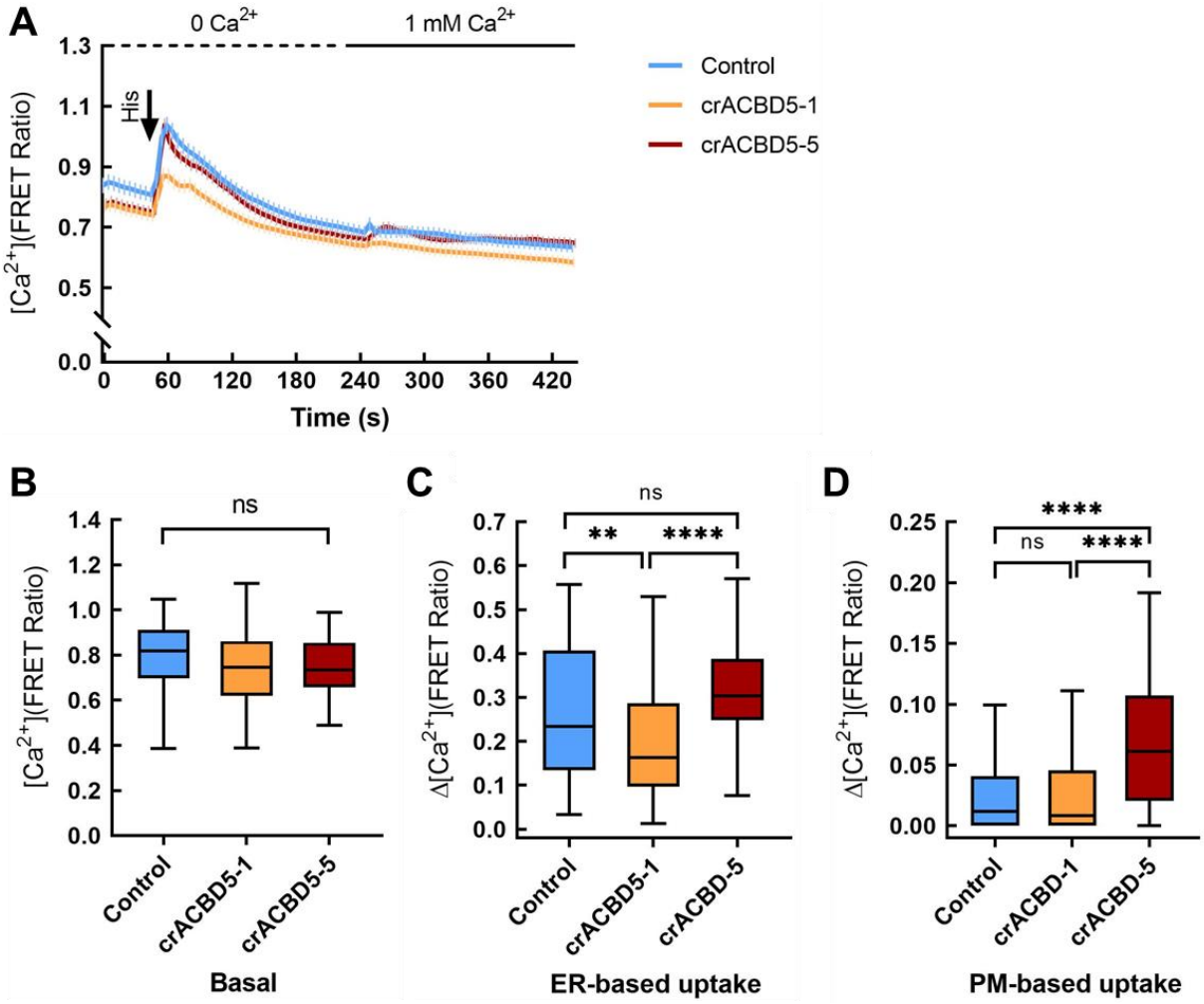

Figure 24. ACBD5 deficient cells show abnormal peroxisomal Ca^{2+} uptake. **(A)** Comparison of ACBD5-deficient crACBD5-1 and crACBD5-5 cell lines with the control in two-step Ca^{2+} measurements. Data presented as mean ± SEM. **(B)** Basal levels of peroxisomal Ca^{2+} are comparable in three cells lines. Analysis based on data from (A). **(C)** ER-based uptake is reduced in crACBD5-1, but normal in crACBD5-5. Data analysis based on (A). **(D)** PM-based uptake is normal in crACBD5-1 but increased in crACBD5-5 compared to control. Data analysis based on (A). n = 59 (control), = 67 (crACBD5-1), = 46 (crACBD5-5) cells from six experiments. **(B-D)** Data presented as Tukey's boxplots. **p < 0.01, ****p < 0.0001, one-way ANOVA followed by Tukey's post hoc test.

4.4.2 ACBD5 knockdown disturbs peroxisomal Ca^{2+} handling

To compare the effect of constitutive absence of ACBD5 with its short-term depletion, ACBD5 knockout in HeLa cells with siRNA was performed. The knockdown was confirmed by western blot 72 hours after transfection (*Figure 25A*) and quantified against Ponceau staining (*Figure 25B*). For the analysis of peroxisomal Ca^{2+} handling, cells were additionally transfected with D3cpV-px and 24 hours later the histamine-based two-step experiment was performed (*Figure 25C*). Upon knockdown (siACBD5) significant decrease of basal Ca^{2+} levels (*Figure 25D*) and PM-based uptake (*Figure 25F*) were detected. The ER-based uptake was reduced in siACBD5 compared to the control (siNT); however, the difference was not statistically significant (*Figure 25E*). Together, the results from ACBD5 knockout and knockdown suggest that ACBD5 may be important for normal peroxisomal Ca^{2+} handling.

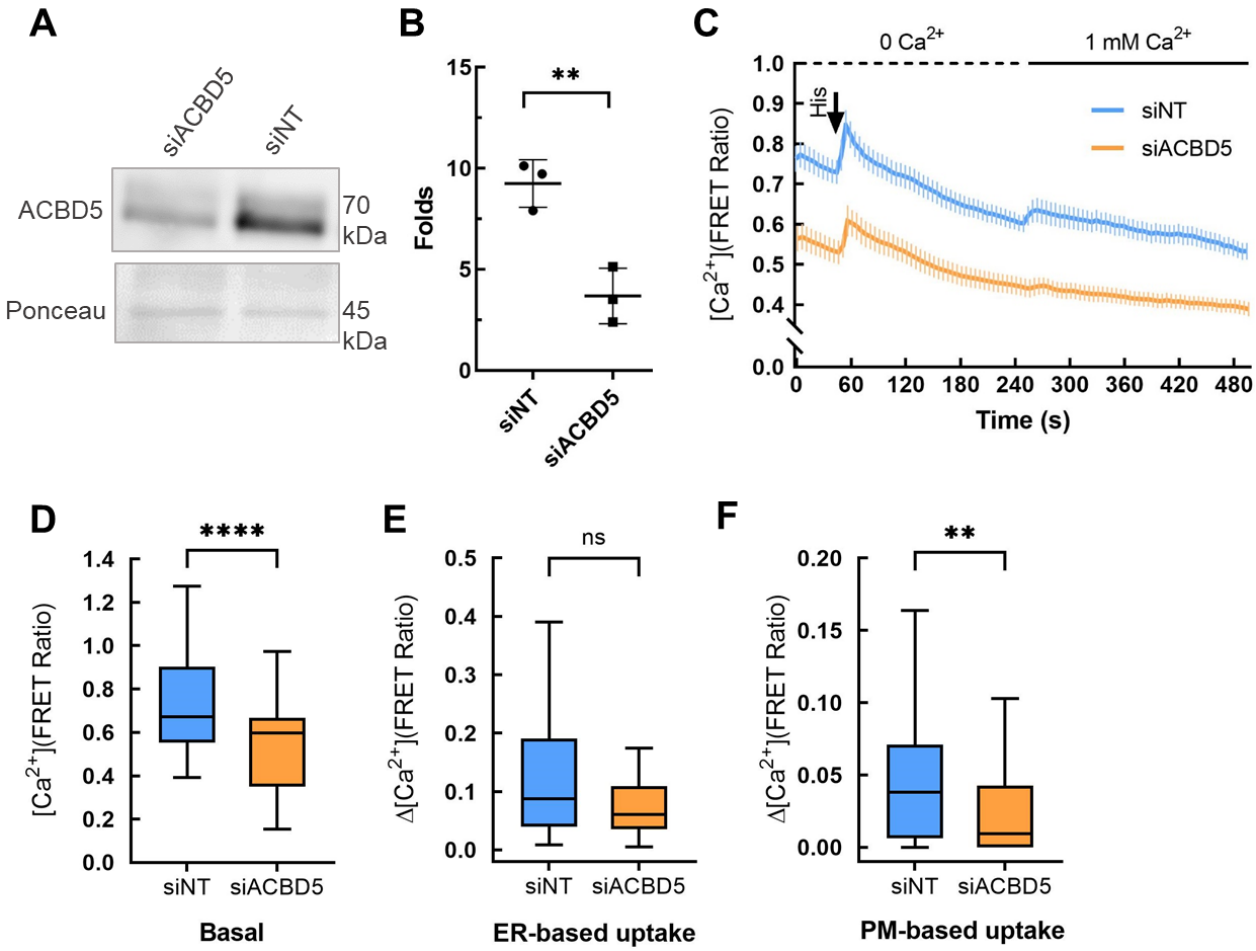

Figure 25. ACBD5 is important for effective peroxisomal Ca^{2+} handling. **(A)** A representative image from western blot showing ACBD5 knockdown. **(B)** Quantification of ACBD5 knockdown efficiency. Mean ± SEM, n = 3. **(C)** Comparison of ACBD5 knockdown cells (siACBD5) with the mock transfected cells (siNT) in histamine stimulated Ca^{2+} measurement. Data presented as mean ± SEM. **(D)** Basal levels are significantly lower in siACBD5 compared to siNT. Data analyzed based on (C). **(E)** SiACBD5 show a tendency for lower ER-based Ca^{2+} uptake compared to the control; however, no significant differences are detected. Analysis based on (C). **(E)** PM-based uptake is significantly reduced in siACBD5. Analysis based on data from (C). n = 44 (siACBD5), = 54 (siNT) from four experiments. ** $p \leq 0.01$, **** $p \leq 0.0001$ Student's t test. **(D-F)** Quantifications presented as Tukey's boxplot.

4.4.3 ACBD5 is targeted to peroxisomes without passing through the ER

Tethering of the ER to other cellular organelles through VAP (residing on the ER) binding to FFAT domain of their partner protein on the apposing membrane is a common mechanism by which MCS are made (Phillips and Voeltz, 2016). They are known to be involved in organelle biogenesis (Scorrano et al., 2019), however, little is known about the biogenesis of the contact sites themselves.

As a tail anchored peroxisomal membrane protein, ACBD5 can either be transferred to peroxisomes during peroxisome biogenesis from the ER or be directly inserted into already existing peroxisomal membrane (Kim and Hettema, 2015; Mayerhofer, 2016).To analyze the possible passage of ACBD5 through the ER (Pedrazzini et al., 2000; Buentzel and Thoms, 2017), ACBD5 with an opsin-tag for N-glycosylation was used in HeLa cells. The samples were then treated with deglycosylating enzymes PNGaseF or EndoH.

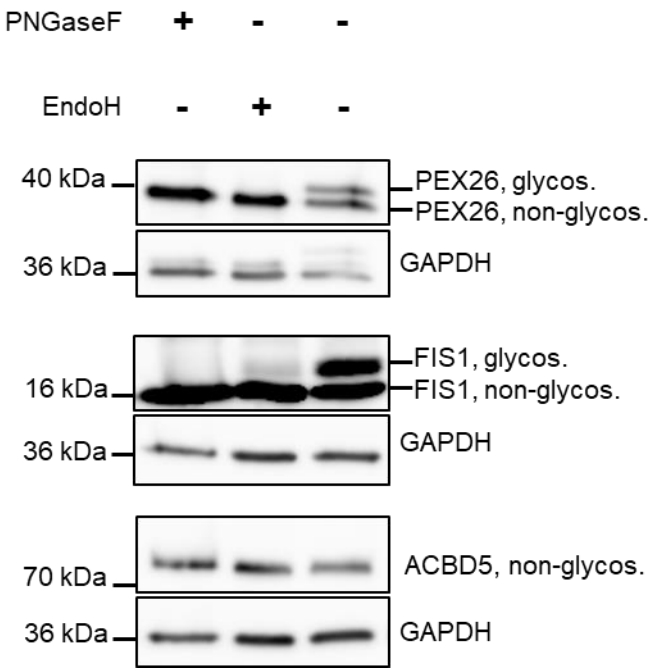

Figure 26. The tail-anchored protein ACBD5 does not pass through the ER. At the same time PEX26 and FIS1 get exposed to the ER. PEX26 and FIS1 proteins appear as double bands, representing glycosylated and non-glycosylated protein. ACBD5 is present only in non-glycosylated form. After PNGaseF and EndoH treatment only the non-glycosylated forms are detected. Western blot, anti-opsin anti-GAPDH antibodies used.

Previously known proteins with ER passage, PEX26 (Buentzel et al., 2015) and FIS1 (Ji et al., 2017), were used as controls (*Figure 26*). The untreated samples expressing PEX26 and FIS1 with opsin-tag showed double bands on the western blot with the upper band corresponding to the glycosylated form. Upon PNGaseF or EndoH treatment only the non-glycosylated (lower band) form remained. In case of ACBD5 only one band was detected in the mock-treated sample, suggesting that ACBD5 targets peroxisomes directly without passing through the ER.

4.4.4 ACBD5 is not a Ca^{2+} transporter

ACBD5 is known to be important for effective lipid transfer between the ER and peroxisomes (Costello et al., 2017a; Hua et al., 2017). Here, we aimed to test if ACBD5 may be directly involved in the transport of Ca^{2+} to peroxisomes. For that peroxisomal Ca^{2+} measurement with D3cpV-px in ACBD5 overexpressing HeLa cells was performed (*Figure 27*). ACBD5 overexpression resulted in an overall curve shift downwards (*Figure 27B*) with significant decrease in the basal Ca^{2+} levels (*Figure 27C*) and mild decrease in ER- and PM-based Ca^{2+} uptakes to peroxisomes (*Figure 27D* and *Figure 27E*). The reason for the decreased Ca^{2+} levels in peroxisomes with ACBD5 overexpression can be explained with the fact that ACBD5 overexpression promotes significant membrane expansion and elongation of peroxisomes (Hua et al., 2017). This may result in dilution of Ca^{2+} in the peroxisomal matrix and reduced measured Ca^{2+} concentration when the total amount of Ca^{2+} is rather unaffected.

Though the current experiment shows that ACBD5 is not a Ca^{2+} transporter itself, it does not contradict the role of ER-peroxisome tethering in the effective Ca^{2+} transfer to peroxisomes, as additional ACBD5 expression in the cells requires also its partner VAPB overexpression for the increase of ER-peroxisome interaction (Costello et al., 2017a).

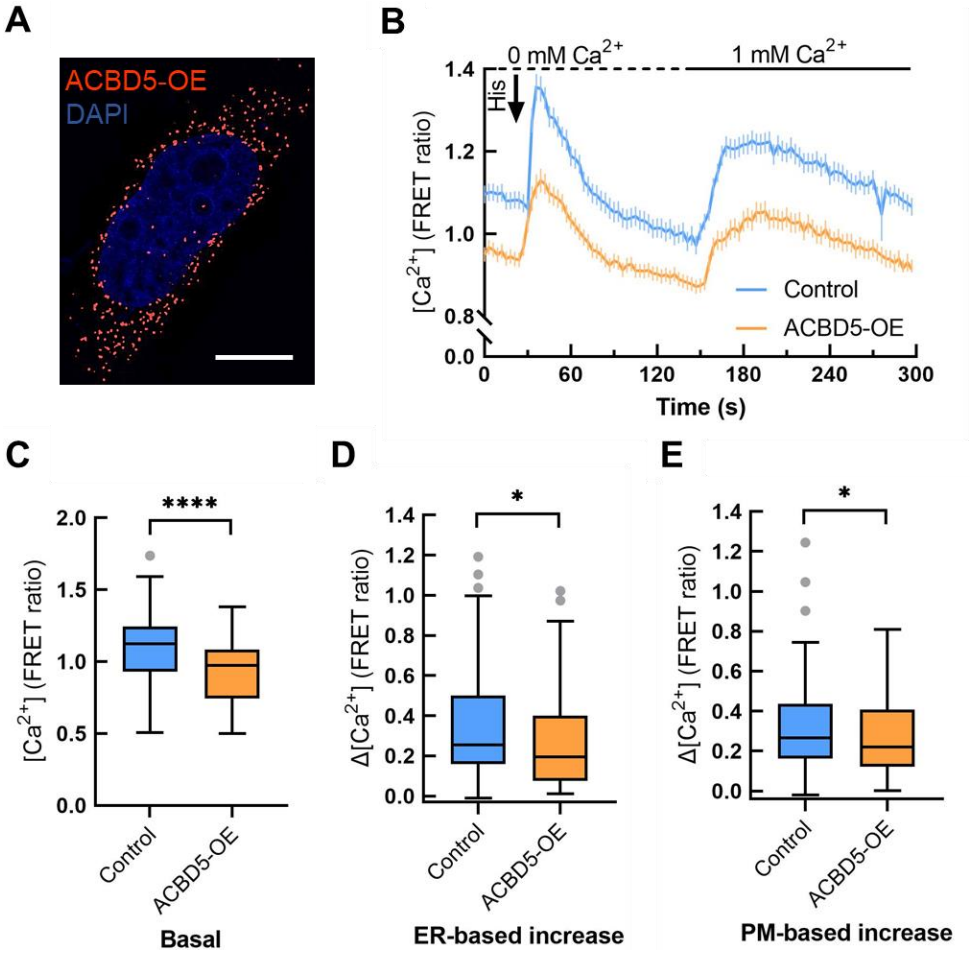

Figure 27. ACBD5 is unlikely peroxisomal Ca^{2+} transporter. **(A)** A representative image from a cell overexpressing ACBD5 construct (ACBD5-OE). **(B)** Comparison of ACBD5 overexpressing cells with mock transfected (control) cells. Data presented as mean ± SEM. **(C)** Basal levels are significantly lower in ACBD5-OE. Analysis based on the data from (B). **(D, E)** Mild decrease in ER- and PM-based uptakes is detected. Data analysis based on the data from (B). **(C-E)** Data presented as Tukey's box plots. Number of cells n = 110 (control), = 149 (ACBD5-OE). **** $p \leq 0.0001$, * $p \leq 0.05$, Student's t test.

4.5 Ca^{2+} transport mechanism to peroxisomes

4.5.1 PEX11 is likely not a Ca^{2+} channel

We first considered PEX11β (henceforth referred to as PEX11) as a peroxisomal Ca^{2+} channel. PEX11 from yeast was shown to have channel properties when inserted into artificial membranes (Mindthoff et al., 2016). To test the potential of PEX11 as peroxisomal Ca^{2+} channel, D3cpV-px was analyzed in combination with PEX11 overexpression.

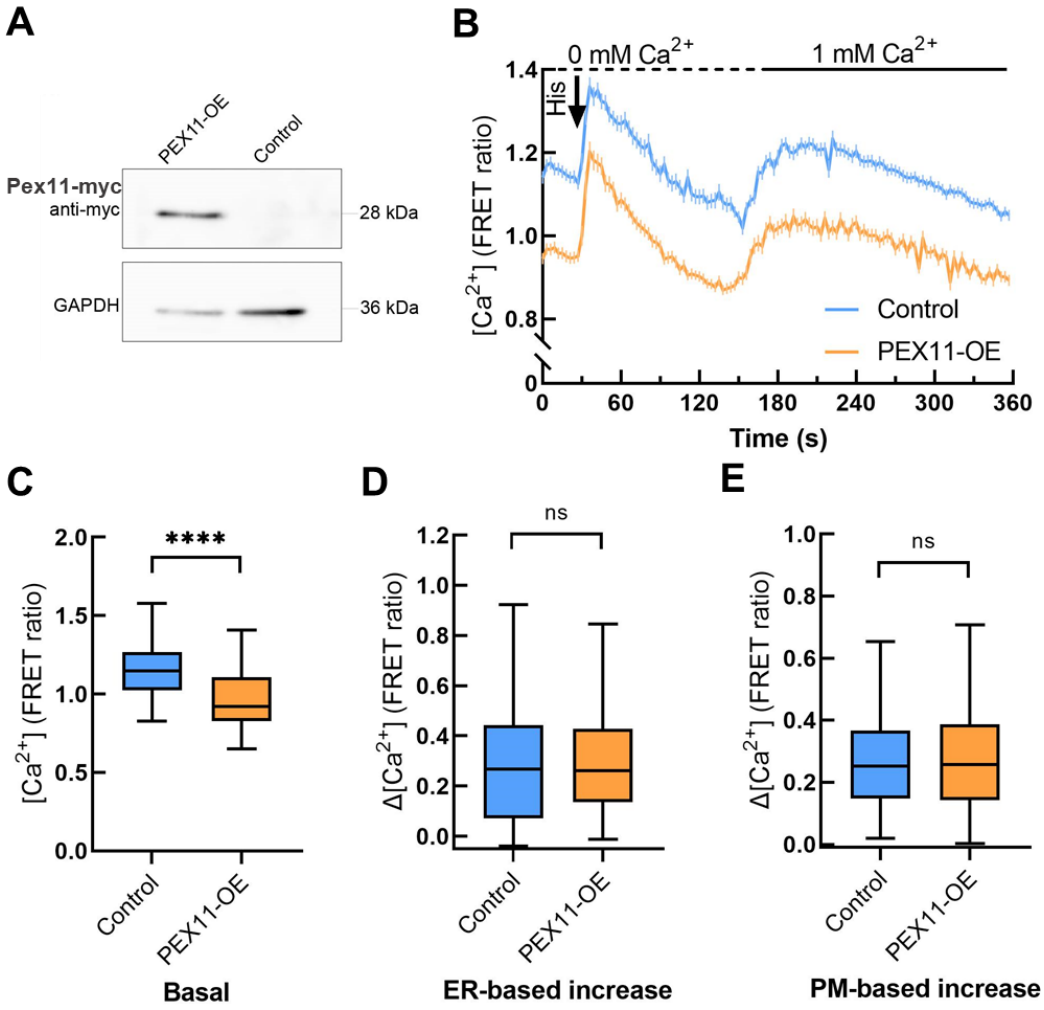

Figure 28. PEX11 is unlikely peroxisomal Ca^{2+} channel. **(A)** A representative image from western blot showing PEX11 overexpression (PEX11-OE), n = 3. **(B)** Comparison of PEX11 overexpressing cells with mock transfected cells. Data presented as mean ± SEM. **(C)** Basal levels are significantly lower in PEX11-OE. Analysis based on the data from (B). **(D, E)** No differences in ER- and PM-based uptakes are detected. Analysis based on the data from (B). **(C-E)** Data presented as Tukey's box plots. Number of cells n = 110 (control), = 149 (PEX11-OE). **** $p \leq 0.0001$, Student's t test.

For that purpose, HeLa cells were transfected with D3cpV-px and PEX11β-myc constructs. The overexpression was confirmed by western blot with anti-myc antibodies (*Figure 28A*).

In case of PEX11 overexpression, the Ca^{2+} change curve had the same shape as in the control, with the exception that it is shifted downwards (*Figure 28B*), so that significantly decreased basal Ca^{2+} levels were observed (*Figure 28C*).

There are neither differences in Ca^{2+} increase upon ER-store depletion (*Figure 28D*) nor in plasma membrane-based uptake seen (*Figure 28E*), suggesting that PEX11 is not a peroxisomal Ca^{2+} channel. The decrease of basal level may be explained by the ability of PEX11 to elongate peroxisomes (Koch et al., 2010), which would result in decreased overall intraorganellar Ca^{2+} concentration in case PEX11 is not a peroxisomal channel or does not activate additional Ca^{2+} entry to peroxisomes.

4.5.2 PXMP2 is a peroxisomal Ca^{2+} channel

The next Ca^{2+} channel candidate was PXMP2. Its ion channel-forming activity is known from studies with recombinant protein inserted in artificial lipid bilayer membranes (Rokka et al., 2009). To test whether PXMP2 is the mechanism of Ca^{2+} entry to peroxisomes, PXMP2 knockdown in HeLa cells with siRNA was performed (*Figure 29A*). The knockdown-efficiency was assessed with western blot 72 hours after transfection and was 80 - 90% (*Figure 29B*). PXMP2 knockdown resulted in general flattening of the peroxisomal Ca^{2+} curve measured with D3cpV-px in the two-step histamine treatment experiment (*Figure 29C*).

Significant decrease of basal Ca^{2+} levels (*Figure 29D*) together with decreased ER- and PM-based uptakes (*Figure 29E-F*) were observed, suggesting that PXMP2 is a Ca^{2+} channel.

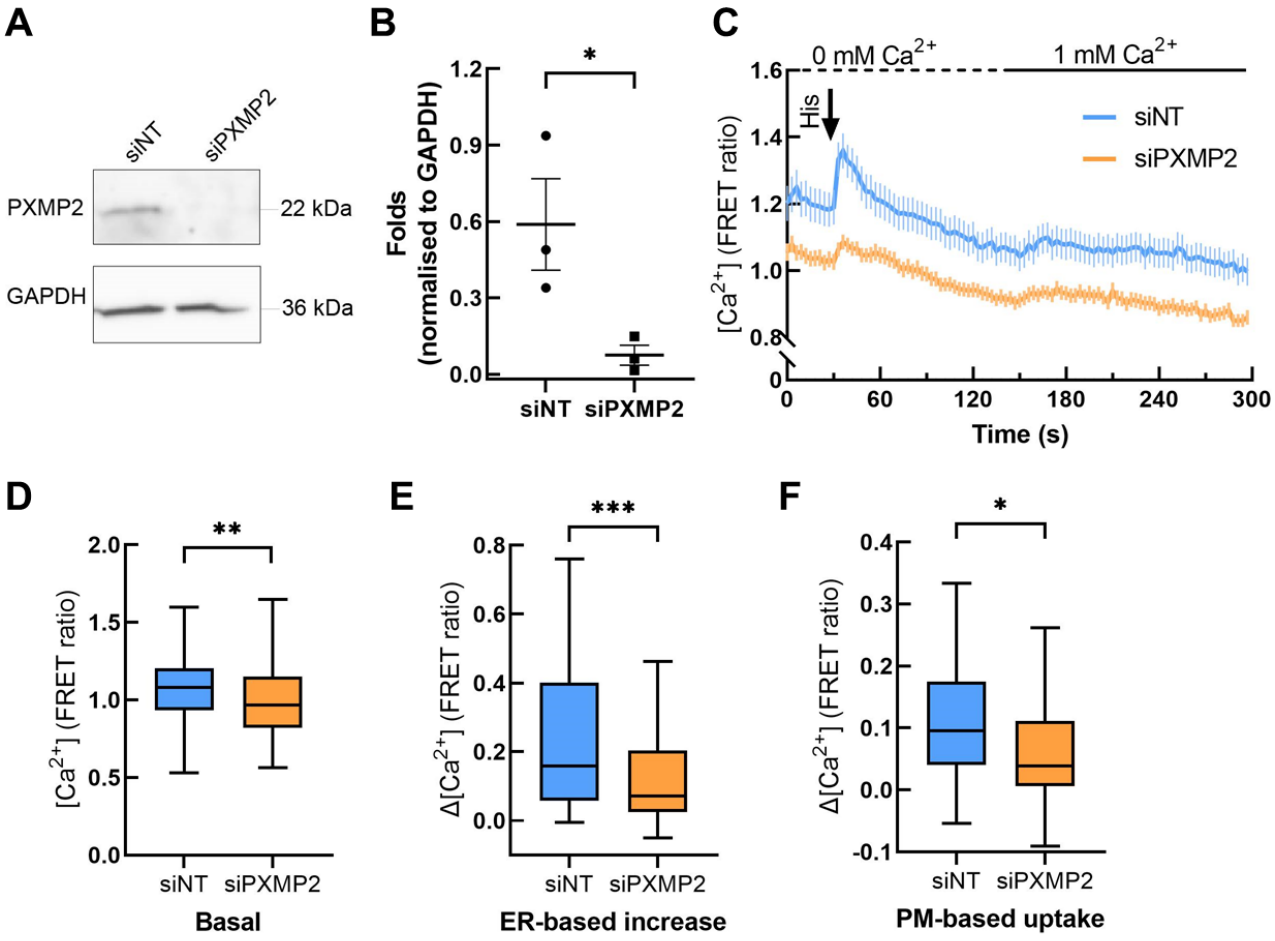

Figure 29. PXMP2 is a peroxisomal Ca^{2+} channel. **(A)** A representative image from western blot showing PXMP2 knockdown. **(B)** PXMP2 knockdown quantification after western blot. **(C)** Comparison of PXMP2 knockdown cells (siPXMP2) with the mock transfected cells (siNT). Number of cells n = 113 (siPXMP2), = 112 (siNT) from five independent experiments. **(D)** Basal, **(E)** ER-based increase and **(F)** PM-based uptake are significantly reduced in siPXMP2. Analysis based on the data from (C) **(B, C)** Data presented as mean ± SEM. **(D-F)** Data presented as Tukey's box plots. * $p \leq 0.01$, ** $p \leq 0.01$, *** $p \leq 0.001$, Student's t test.

4.5.3 PXMP2 knockdown does not affect cytosolic Ca^{2+} handling

In case PXMP2 plays a role in shaping total cellular Ca^{2+} homeostasis, its depletion may result in cellular Ca^{2+} overload. To test if PXMP2 may play a major role in regulation of Ca^{2+} homeostasis on the cellular level under standard conditions, cytosolic Ca^{2+} handling was analyzed in PXMP2 knockdown. HeLa cells expressing D3cpV were treated according to two-step histamine addition experiment design, which represents the most

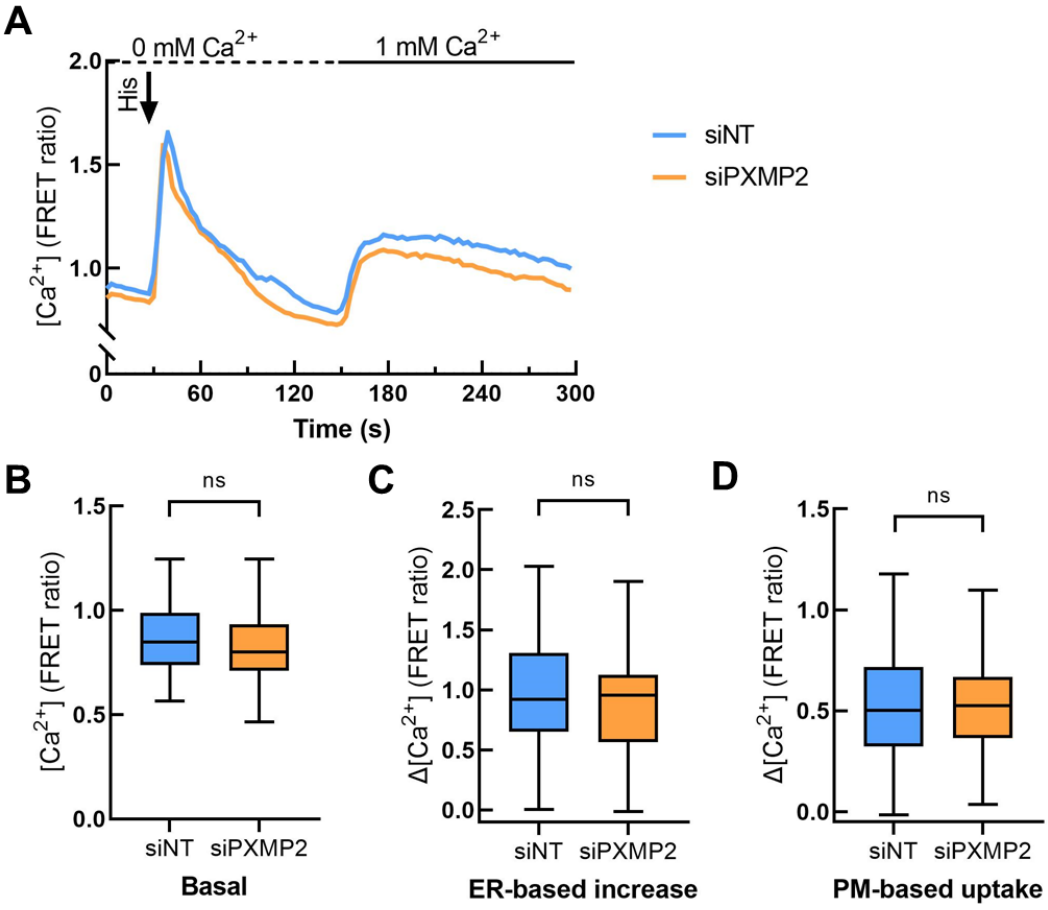

Figure 30. PXMP2 knockdown (siPXMP2) does not affect cytosolic Ca^{2+} handling. **(A)** Comparison of siPXMP2 with control (siNT) in two-step histamine-based stimulation experiment. Data presented as mean. **(B)** Basal, **(C)** ER-based increase and **(D)** PM-based uptake are not different between siPXMP2 and siNT. Analysis based on data from (A). Number of cells from three independent experiments n = 70 (siPXMP2), = 76 (siNT). Student's t test. Quantifications presented as Tukey's boxplot.

physiological stimulation (*Figure 30A*). There were no differences detected between basal (*Figure 30B*), ER-based Ca^{2+} increase (*Figure 30C*) or PM-based Ca^{2+} uptake (*Figure 30D*). These suggest that the role of PXMP2 in Ca^{2+} homeostasis under physiological conditions is most likely restricted to peroxisomes.

4.5.4 PXMP2 knockdown does not affect the levels of major peroxisomal proteins

To test the potential effects of PXMP2 downregulation for peroxisomes and cell in general, we analyzed the peroxisomal enzymes catalase (*Figure 31A*) and thiolase (ACAA1) (*Figure 31B*), and the membrane protein PMP70 levels (*Figure 31C*) by western blotting in PXMP2 knockdown. None of the analyzed proteins was affected, suggesting that major

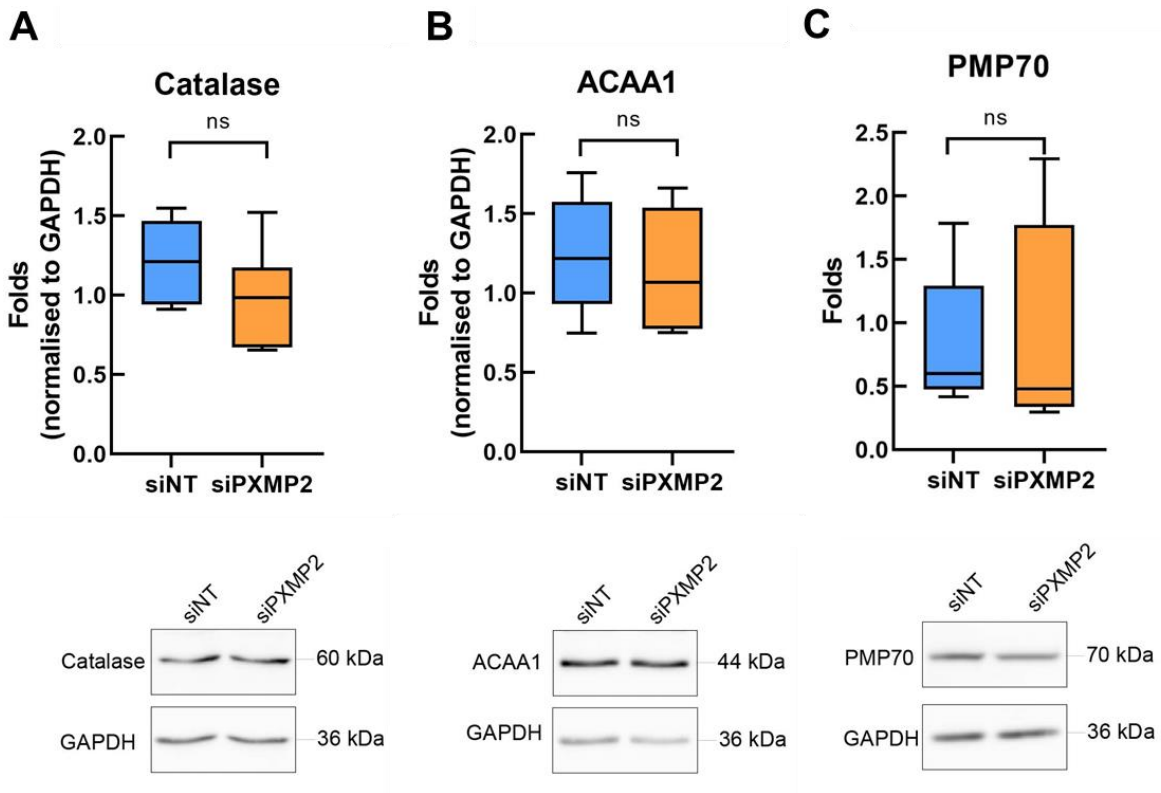

Figure 31. PXMP2 knockdown (siPXMP2) effects on peroxisomes. **(A)** Catalase, **(B)** thiolase (ACAA1) and **(C)** PMP70 levels are not affected in siPXMP2 compared to control. Upper panels present western blot quantifications, representative images from western blots are shown in the lower panels. The normalization is done to GAPDH in case of catalase and ACAA1, or to GAPDH and Ponceau-stained membrane in case of PMP70. n = 6, Student's t test. Quantifications presented as Tukey's boxplot.

peroxisomal functions are unaffected in the absence of PXMP2 under standard conditions.

4.5.5 ACBD5 and PXMP2 double knockdown decreases ER-based Ca^{2+} uptake to peroxisomes

After showing that ACBD5 may be important for the effective Ca^{2+} handling in peroxisomes and that PXMP2 is a peroxisomal Ca^{2+} channel, we aimed to test whether the combined knockdown of ACBD5 and PXMP2 may also affect peroxisomal Ca^{2+} handling (*Figure 32)*.

The knockdown was performed with simultaneous transfection of siRNAs and confirmed at the protein expression level 72 hours after transfection by western blot (*Figure 32A*). The knockdown efficiency of ACBD5 was overall higher than the efficiency in the single knockdown experiment (*Figure 32B*). Knockdown efficiency of PXMP2 was, however, lower compared to the single knockdown (*Figure 32C*). Though there was still increase upon both histamine and extracellular Ca^{2+} stimulation detected (*Figure 32D*), the responses to ER-store depletion (*Figure 32E*) and PM-based cellular Ca^{2+} increase (*Figure 32F*) were significantly decreased in the double knockdown compared to the control.

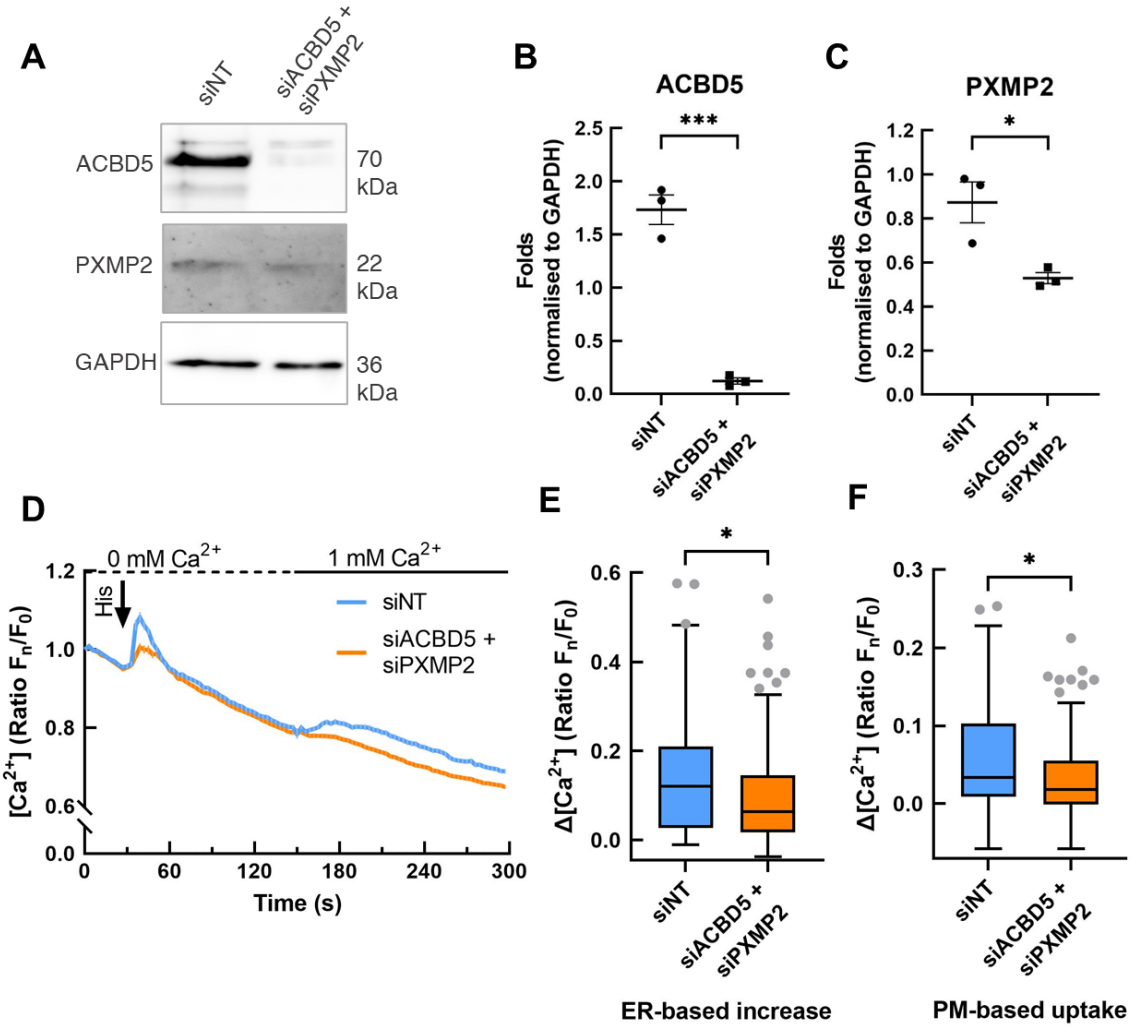

Figure 32. ACBD5 and PXMP2 double knockdown decreases stimulated peroxisomal Ca^{2+} uptake. **(A)** A representative image from western blot showing ACBD5 and PXMP2 knockdown. **(B)** Quantification of ACBD5 knockdown efficiency. **(C)** Quantification of PXMP2 knockdown efficiency. **(D)** Comparison of double knockdown cells (siACBD5 + siPXMP2) with the mock transfected cells (siNT) in histamine stimulated Ca^{2+} measurement. **(E)** The knockdown cells have significantly decreased ER-based Ca^{2+} uptake compared to the control. Analysis based on (D). **(F)** PM-based uptake is significantly reduced in the knockdown. Analysis based on data from (D). Number of cells n = 95 (siACBD5 + siPXMP2), = 112 (siNT) from seven (for siACBD5 + siPXMP2) and nine (for siNT) experiments. * $p \leq 0.05$, Student's t test. **(B-D)** Data presented as mean ± SEM. **(B, C)** n = 3. **(E-F)** Quantifications presented as Tukey's boxplot.

At the same time, the knockdown did not affect the cytosolic Ca^{2+} handling to noticeable degree (*Figure 33A*). No significant differences were detected between basal (*Figure 33B*) or ER-based Ca^{2+} increase (*Figure 33C*) in the cytosol, indicating that the role of ACBD5 and PXMP2 in Ca^{2+} handling is restricted to peroxisomes.

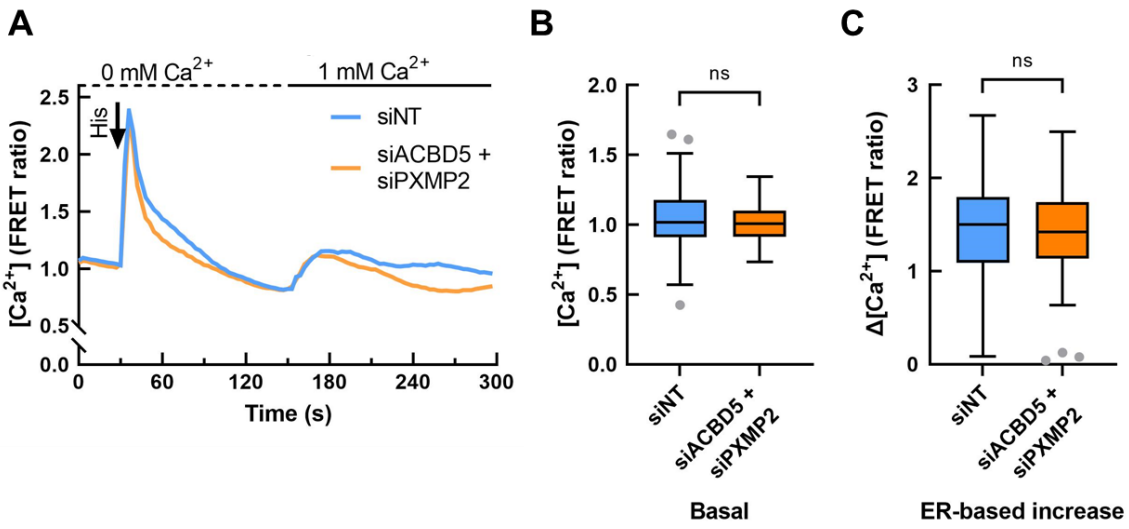

Figure 33. ACBD5 and PXMP2 double knockdown (siACBD5 + siPXMP2) does not affect cytosolic Ca^{2+} handling. **(A)** Comparison of siACBD5 + siPXMP2 with control (siNT) in two-step histamine-based stimulation experiment. Data presented as mean. **(B)** Basal and **(C)** ER-based increase are not different between siACBD5 + siPXMP2 and siNT. Analysis based on data from (A). Number of cells n = 53 (siACBD5 + siPXMP2), = 80 (siNT). Student's t test from six (for siNT) and five (for siACBD5 + siPXMP2) independent experiments. Quantifications presented as Tukey's boxplot.

5. Discussion

Peroxisomes are highly dynamic organelles capable of fast reaction to nutritional and environmental changes (Islinger et al., 2012). The multiple interconnections of peroxisomal and extraperoxisomal metabolic systems imply that peroxisomes may be involved in the regulation of cellular processes and be a part of signaling pathways (Islinger et al., 2012; Sargsyan and Thoms, 2020). To this extent, Ca^{2+} handling is an interesting aspect of focus especially when taking into account that Ca^{2+}-dependent transporters were reported to be present in peroxisomes (Weber et al., 1997) and considering the important role of Ca^{2+} in excitable cells.

5.1 Peroxisomal Ca^{2+} in non-excitable cells

The interest in peroxisomal Ca^{2+} is primarily attributed to plant research. Known from *Arabidopsis* Ca^{2+}-dependent protein kinase AtCPK1 is targeted to peroxisomes (Dammann et al., 2003). Additionally, in plants peroxisomal Ca^{2+} and CaM are essential for protein import and functionality of peroxisomal enzymes (Corpas and Barroso, 2018), including the nitric oxide (NO) synthase-like activity of plant peroxisomes (Corpas et al., 2004).

The first attempts to measure peroxisomal Ca^{2+} in mammalian cells were made by Drago et al. (2008) and Lasorsa et al. (2008). These studies brought up contradictions about the levels of Ca^{2+} in peroxisomes and the kinetics of peroxisomal Ca^{2+} handling. Based on an aequorin sensor, Lasorsa et al. (2008) conclude that peroxisomal Ca^{2+} concentration in steady state is around 20-fold higher than in the cytosol and can rise up to 70 µM in HeLa cells. On the other side, Drago et al. (2008) show that peroxisomal Ca^{2+} levels are similar to cytosolic Ca^{2+} and rise slowly when the concentration of the latter rises. The differences in the results and conclusions can be partially attributed to the different techniques and cell types used.

In the current study, three GECI that cover a broad Ca^{2+} sensibility range – K_d 0.6 µM, 1.7 µM and 60 µM – were used for comparison with the results of the two aforementioned papers (*Table 13*). D1cpV-px with the highest K_d had the lowest dynamic range and detected only minimal increase in FRET upon maximal possible stimulation. The response

of D3cpV-px (shown here) and pericam-px (published in Sargsyan et al. (2021)) were optimal and comparable, suggesting that peroxisomal Ca^{2+} levels are in the optimal detection range of these sensors. Pericam as a classical EYFP-based sensor may be pH-sensitive in an acidic environment (Nagai et al., 2001). Here, we did not detect signal changes of YFP variants that could be attributed to Ca^{2+}-independent changes of the sensor, suggesting that even measurements with supposedly more pH-sensitive pericam-px can be viewed as reliable.

The results of this work are based on the measurements with the same sensor as Drago et al. (2008), but with a stronger PTS-1 signal (D3cpV-px).

In the experiments with HeLa cells, we found basal peroxisomal Ca^{2+} levels with mean value of 600 nM and increase upon stimulation up to 2.4 µM. Noteworthy, some very rare cells had much higher basal peroxisomal Ca^{2+} levels of 1 µM or 3 µM (which would be 20-folds higher than the expected cytosolic level) and correspond to the findings of Lasorsa et al. (2008). Upon stimulation, again some rare cells showed extremely high increase of peroxisomal Ca^{2+} up to 6.5 µM and higher. The absence of correlation between the high maximal response and basal Ca^{2+} values speaks against the hypothesis that peroxisomes have a strictly limited Ca^{2+} uptake capacity and may mean rather that Ca^{2+} increase in peroxisomes is very much dependent on the cell state.

Table 13. Properties of peroxisomal and cytosolic GECIs (Sargsyan et al., 2021)

Cytosolic GECIs			**Peroxisomal GECIs**	
Name	**K_d (*in vitro*)**	**Dynamic range, D**	**Name**	**Maximal increase upon 1 mM Ca^{2+} addition in permeabilized cells**
D3cpV	0.6 µM [(1)]	5.0 [(1)]	D3cpV-px	1.50 x
D1cpV	60 µM [(2)]	1.7 [(3)]	D1cpV-px	1.08 x
Ratiometric-pericam	1.7 µM [(4)]	10.0 [(4)]	Pericam-px	1.50 x

References: [1] Palmer et al. (2006); [2] Palmer et al. (2004); [3] Greotti et al. (2016) [4] Nagai et al. (2001)

5.2 Peroxisomal Ca^{2+} in cardiomyocytes

The localization of peroxisomes close to the T-tubular system and SR has been shown decades ago (Hicks and Fahimi, 1977). The SR is the essential site of the excitation-contraction coupling and effective Ca^{2+} handling in muscle cells (Flucher et al., 1994). Using chemical stimulation, in this study it was demonstrated that Ca^{2+} enters peroxisomes upon intracellular Ca^{2+}-store depletion in NRCMs and hiPSC-CMs. As intracellular store depletion by the activation of RyR through Ca^{2+} from the LTCC (Ca^{2+}-induced Ca^{2+}-release) is the main source of Ca^{2+} increase in CMs in the excitation-contraction coupling (Bers and Perez-Reyes, 1999), it can be hypothesized that peroxisomes take up Ca^{2+} also on beat-to-beat manner in these cells. Indeed, we have now shown in Sargsyan et al. (2021) that upon field stimulation with 1 Hz frequency peroxisomes in NRCM take up Ca^{2+} in beat-to-beat manner.

In this work it is shown that peroxisomes in hiPSC-CMs localize more often in vicinity of ER protein RyR2 than to T-tubular system and LTCC. A systematic quantification of peroxisome proximity to ER protein RyR2 and T-tubular development factor Cav3 in adult mice isolated CMs further shows that over 80% of peroxisomes contact RyR2. It is known from monkey kidney fibroblast-like COS-7 cell line that over 90% of peroxisomes are in contact with the ER (Valm et al., 2017). The molecular mechanisms of ER-peroxisome contact are reported to be ACBD4/5-VAPB, and Miro1v4-VPS13D-VAP (Costello et al., 2017a, 2017b; Hua et al., 2017; Guillén-Samander et al., 2021). Whether there is a tissue specific difference of described MCS and which of the described membrane contact sites is the main for the CMs is, however, not known.

As peroxisomes take up SR originating Ca^{2+} and localize proximally to RyR receptors in CMs, it is plausible that peroxisomes may contribute or even be essential for normal excitation-contraction coupling. This hypothesis is supported partially by the fact that patients with mild forms of ZSS occasionally present with cardiac arrhythmias that become the cause of lethal outcome in those cases (Wanders and Komen, 2007). The reason of the arrhythmias can be the metabolic role of peroxisomes (Colasante et al., 2015), however, the direct contribution to efficient Ca^{2+} handling is another plausible reason.

5.3 Peroxisomal morphology

The methods developed in this work for the analysis of peroxisome morphology and contacts in cardiomyocytes can be applied for the detailed study of peroxisome morphology. The previous reports on peroxisome morphology in ZSS describe peroxisome ghosts as (typically) enlarged, empty and non-functional peroxisomal membranes in patient fibroblasts (Santos et al., 1988, 2000). In the current study we also found rounded peroxisomal ghosts in Pex5-KO CMs, concurrent with previous studies (Soliman et al., 2018). However, PEX10 deficient patient fibroblasts show less rounded peroxisomes in comparison to the healthy cells. Previous studies have also identified differences in peroxisome phenotypes in classical severe ZSS and patients having a defect in the RING complex (PEX2, PEX10 and PEX12) components (Soliman et al., 2018). In particular, the defects of RING complex result in more compact peroxisomes. In the patient fibroblasts analyzed here peroxisomal size was unaffected and comparable to that of control. Interestingly, the defects of RING complex protein PEX10 are typically associated with milder disease course (Régal et al., 2010; Yamashita et al., 2017). The reason of that could be partially conserved import of peroxisomal proteins. Indeed, in the patient cells analyzed here double as much catalase is present in the cytosol compared to the control but several cells with functional peroxisomes are present in one field.

High precision imaging with STED microscopy enables the study of the complexity of fine cellular structures (Saka and Rizzoli, 2012). Here, it revealed that peroxisomal ghosts are only peroxisomal membrane and do not have detectable space between the membrane components typical for the control healthy peroxisomes. This suggests that earlier as empty called peroxisomes with the increased size in ZSS are knotted peroxisomal membrane without lumen.

5.4 Peroxisomal channels and their functions

Several peroxisomal membrane proteins have been suggested as channels, pores and transport carriers based on studies on artificial membranes (Visser et al., 2002; Rokka et al., 2009; Agrimi et al., 2012; Mindthoff et al., 2016). The most prominent of them showing high and unspecific permeability for substrates with up to 300 Da size is PXMP2 (Rokka et al., 2009). However, the mice lacking PXMP2 did not have any phenotype except the

poor development of the mammary ducts (Vapola et al., 2014). The mild phenotype of PXMP2 deficiency could be attributed to the possible redundancy of peroxisomal channel and pore functions (Vapola et al., 2014; Chornyi et al., 2021): if one channel is no longer present another one can take up, at least partially, its function. This hypothesis, however, lacks support of any *in vivo* experimental evidence.

The study on H_2O_2 transfer across peroxisomal membrane in single cells using genetically encoded sensors showed that PXMP2 and PEX11β are not channels for hydrogen peroxide (Lismont et al., 2019). The question rises if H_2O_2 crosses peroxisomal membrane rather through the transporters such as PXMP4 or PEX34 and not through channels (Lismont et al., 2019) and puts under doubt the notion of redundancy and non-specificity of peroxisomal channels.

In the current work PXMP2 was identified as a Ca^{2+} channel. Its depletion almost abolished Ca^{2+}-increase in peroxisomes, implying that the function of Ca^{2+} transfer to peroxisomes is exclusive to PXMP2 at least in the short-term depletion of the channel with siRNA. Furthermore, PEX11β is not a Ca^{2+} channel. Consecutively, the current study is the first to identify a specific substrate for PXMP2 transport in living mammalian cells.

5.5 The role of peroxisomal Ca^{2+}

The question about the cellular function of peroxisomal Ca^{2+} is still open. The interplay of redox and Ca^{2+} signaling is well described in mitochondria (Petrungaro et al., 2015). Yet, no peroxisomal processes or enzymes, except of some plant catalases (Yang and Poovaiah, 2002), are so far known to depend on or require Ca^{2+}. Weber et al. (1997) suggested the presence of Ca^{2+}-dependent mitochondrial solute carriers also on peroxisomes. They would serve along with peroxisomal malate dehydrogenase and LDHBx as crucial components of malate and lactate shuttles across peroxisomal membrane for reduction equivalent reoxidation (McClelland et al., 2003). LDHBx overexpression in this thesis resulted in increased Ca^{2+} uptake to peroxisomes. Though not being a direct proof of the existence of Ca^{2+}-dependent solute carriers on peroxisomes, these results support other pieces of evidence from the literature about the existence of lactate shuttle across peroxisomal membrane.

Miro1v4, another peroxisomal membrane protein, has two EF-hands which are essential for Miro-VPS13D interaction (Guillén-Samander et al., 2021). Experiments did not find Ca^{2+}-dependent interaction of Miro-VPS13D for mitochondria, still no experimental data is available for this interaction on the peroxisomes (Guillén-Samander et al., 2021).

In mitochondria Ca^{2+} regulates metabolic processes, reversely metabolic processes regulate Ca^{2+} uptake to mitochondria (Nemani et al., 2018). Though no specific peroxisomal enzyme is yet known to be Ca^{2+}-regulated in peroxisomes, Ca^{2+} channel blockers nifedipine and diltiazem suppress peroxisomal fatty acid oxidation enzymes and peroxisome proliferation (Watanabe and Suga, 1988).

The role of peroxisomal Ca^{2+} should not be, however, necessarily the regulation of peroxisomal processes. Drago et al. (2008) have suggested that peroxisomes may serve as additional cytosolic buffer. This idea is supported by the fact that peroxisomal Ca^{2+} rises after ER-store depletion in mitochondrial calcium uniporter (MCU) knockdown beyond its initial maximum (Sargsyan et al., 2021). This gives a hint that in some cases of cellular Ca^{2+} overload peroxisomes may take up more Ca^{2+} than under near-physiological standard conditions, therefore serving as an extra buffer for Ca^{2+} overload. As the protective effect of peroxisomal Ca^{2+} uptake may be necessary only in some special cases, this may explain why PXMP2 lacking mice do not have any specific phenotype without challenges (Vapola et al., 2014).

Based on the findings of this study that the Ca^{2+} concentration in the peroxisome is higher than in the cytosol, it could be that peroxisomes may also serve as additional Ca^{2+} source for the cytosol in extreme situations. The buffering function of peroxisomes may be protective in some cases of arrhythmia when Ca^{2+} sparks occur. On the other hand, the absence of peroxisomes in this manner may contribute to pathogenesis and strengthen the presentation of provoked arrhythmia.

5.6 Model of peroxisomal Ca^{2+} handling

The current study revealed that PXMP2 is a peroxisomal Ca^{2+} channel. As its knockdown did neither affect major peroxisomal enzymes, the membrane protein PMP70 levels, nor the morphology of peroxisomes to the noticeable level, PXMP2 can be a potential

pharmacological target for regulation of peroxisomal Ca^{2+} levels. Another interesting aspect is that tethering of peroxisomes to the ER through ACBD5 was shown to be important for effective peroxisomal Ca^{2+} handling.

In this study the basal peroxisomal Ca^{2+} levels were found to be higher than cytosolic levels. This could be explained by coexisting proton gradient across the membrane and direct or indirect H^+/Ca^{2+} exchange. The correlation of Cl^- and Ca^{2+} transports across membranes has been analyzed in lysosomal ion homeostasis (Astaburuaga et al., 2019). The stable pH values and absence of acidification detected in the current measurements, however, speak against H^+/Ca^{2+} or Cl^-/Ca^{2+} exchange across the peroxisomal membrane.

Ca^{2+} gradient on the two sides of the membrane can be supported by ATP-dependent uptake mechanism, such as SERCA on the ER membrane (Clapham, 2007). Alternatively, locally high Ca^{2+} concentration at the microdomain of the ion entry site can give an artificial impression of concentration differences on the two sides of the membrane. This mechanism is known from the mitochondrial Ca^{2+} handling and ER-mitochondria contact sites (Petrungaro et al., 2015; Liu and Zhu, 2017). ER tethering to mitochondria at MAMs comprises IP_3R on the ER side, molecular chaperone glucose-regulated protein 75, and voltage-dependent anion channel (VDAC) on outer mitochondrial membrane, which in turn interacts with MCU complex on the inner mitochondrial membrane (Liu and Zhu, 2017). The molecular scaffold of this MCS includes tethers that are not Ca^{2+} channels themselves but are essential for effective Ca^{2+} transfer to the mitochondria (Hirabayashi et al., 2017; Liu and Zhu, 2017). Following the model known from the ER-mitochondria MCS in the role of Ca^{2+} handling, here a model of ER-peroxisome MCS and channels is suggested for peroxisomal Ca^{2+} handling.

VAPB on the ER tethers peroxisomes with the ACBD5 (and ACBD4). This MCS components are proximally localized to IP_3R channel (in non-excitable cells) or RyR2 (in CMs) on the ER and PXMP2 on the peroxisomes (*Figure 34*).

The proximity and possible interaction of VAPB, PXMP2 and ACBD5 in one complex is supported by their simultaneous identification in proteomic analysis of peroxisomal enriched fractions in Nycodenz density gradient centrifugation (Gronemeyer et al., 2013; Zhou et al., 2015). Additionally SERCA isoform 2 is also enriched in the peroxisomal fraction (Gronemeyer et al., 2013; Zhou et al., 2015).

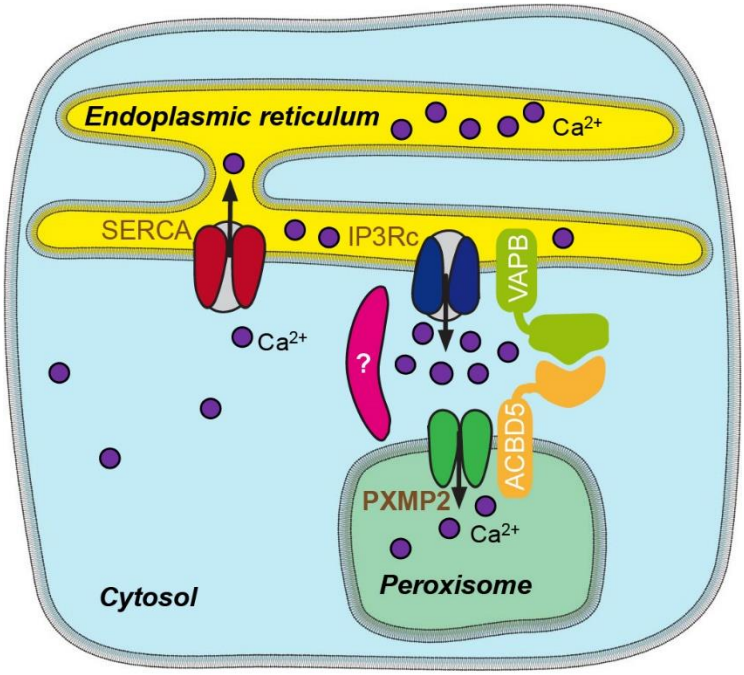

Figure 34. Peroxisomal Ca^{2+} entry in non-excitable cells. ER Ca^{2+} release triggers Ca^{2+} entry into the peroxisome. In this hypothetical model, ER-peroxisome tethering through ACBD5, VAPB and other yet unknown components (the question mark in the schematic) shield a Ca^{2+} microdomain with locally concentrated Ca^{2+}. As a result, Ca^{2+} entry to peroxisomes through PXMP2 channel follows the local gradient. IP3Rc: IP_3 receptor calcium release channel of the ER. Modified from Sargsyan et al. (2021).

The idea of cooperative contributions of PXMP2 and ACBD5 in Ca^{2+} transfer is further supported by their high expression in the heart compared to other organs in humans. The gene expression profile of *PXMP2* in humans shows the highest expression in the liver, and the second highest in the heart (Cardoso-Moreira et al., 2019). The high expression in the liver is in accordance with the high peroxisome number in this organ (Islinger et al., 2010). A similar expression profile is found for ACBD5 (Cardoso-Moreira et al., 2019).

The molecular interaction of the proteins included in the presented model, however, needs a further experimental confirmation. Additional components of the ER-peroxisome Ca^{2+} transfer interface may exist as well. Further aspect of future research is the role of PXMP2 in the heart and peroxisomal Ca^{2+} in arrhythmias.

Taking into account the high abundance of peroxisomes in hepatocytes and their exceptional role in the development and maintenance of normal neuronal function (Islinger et al., 2010; Berger et al., 2016), the study of peroxisomal Ca^{2+} in hepatocytes and neurons may be of special interest.

5.7 Conclusion

The work described here identified the Ca^{2+} transport mechanism to peroxisomes and the crucial role of ER-peroxisome MCS through ACBD5 in this process. Whether the MCS components directly interact with the PXMP2 channel on the peroxisomes or with Ca^{2+} channels on the ER is a matter of future research. Biologically important, peroxisomes in cardiomyocytes take up Ca^{2+}. Finally, the experiments and analysis of peroxisomal Ca^{2+} handling presented here for CMs and morphological characterization of peroxisomes can be applied for virtually any cell type.

Bibliography

Abbe, E. (1873). Beiträge zur Theorie des Mikroskops und der mikroskopischen Wahrnehmung. *Archiv f. mikrosk. Anatomie* 9, 413–468. doi:10.1007/BF02956173.

Abu-Safieh, L., Alrashed, M., Anazi, S., Alkuraya, H., Khan, A. O., Al-Owain, M., et al. (2013). Autozygome-guided exome sequencing in retinal dystrophy patients reveals pathogenetic mutations and novel candidate disease genes. *Genome research* 23, 236–247. doi:10.1101/gr.144105.112.

Agrimi, G., Russo, A., Scarcia, P., and Palmieri, F. (2012). The human gene SLC25A17 encodes a peroxisomal transporter of coenzyme A, FAD and NAD+. *Biochem J* 443, 241–247. doi:10.1042/BJ20111420.

Aranovich, A., Hua, R., Rutenberg, A. D., and Kim, P. K. (2014). PEX16 contributes to peroxisome maintenance by constantly trafficking PEX3 via the ER. *J Cell Sci* 127, 3675–3686. doi:10.1242/jcs.146282.

Astaburuaga, R., Quintanar Haro, O. D., Stauber, T., and Relógio, A. (2019). A Mathematical Model of Lysosomal Ion Homeostasis Points to Differential Effects of Cl- Transport in Ca2+ Dynamics. *Cells* 8, E1263. doi:10.3390/cells8101263.

Bachar-Wikstrom, E., Curman, P., Ahanian, T., Leong, I. U. S., Larsson, H., Cederlöf, M., et al. (2020). Darier disease is associated with heart failure: a cross-sectional case-control and population based study. *Sci Rep* 10, 6886. doi:10.1038/s41598-020-63832-9.

Baes, M., Gressens, P., Baumgart, E., Carmeliet, P., Casteels, M., Fransen, M., et al. (1997). A mouse model for Zellweger syndrome. *Nat Genet* 17, 49–57. doi:10.1038/ng0997-49.

Baes, M., and Van Veldhoven, P. P. (2006). Generalised and conditional inactivation of Pex genes in mice. *Biochim Biophys Acta* 1763, 1785–1793. doi:10.1016/j.bbamcr.2006.08.018.

Balijepalli, R. C., Foell, J. D., Hall, D. D., Hell, J. W., and Kamp, T. J. (2006). Localization of cardiac L-type Ca(2+) channels to a caveolar macromolecular signaling complex is required for beta(2)-adrenergic regulation. *Proc Natl Acad Sci U S A* 103, 7500–7505. doi:10.1073/pnas.0503465103.

Bartlett, M., Nasiri, N., Pressman, R., Bademci, G., and Forghani, I. (2021). First reported adult patient with retinal dystrophy and leukodystrophy caused by a novel ACBD5 variant: A case report and review of literature. *Am J Med Genet A* 185, 1236–1241. doi:10.1002/ajmg.a.62073.

Baumgart, E., Fahimi, H. D., Stich, A., and Völkl, A. (1996). L-lactate dehydrogenase A4- and A3B isoforms are bona fide peroxisomal enzymes in rat liver. Evidence for

involvement in intraperoxisomal NADH reoxidation. *J Biol Chem* 271, 3846–3855. doi:10.1074/jbc.271.7.3846.

Baumgart, E., Vanhorebeek, I., Grabenbauer, M., Borgers, M., Declercq, P. E., Fahimi, H. D., et al. (2001). Mitochondrial alterations caused by defective peroxisomal biogenesis in a mouse model for Zellweger syndrome (PEX5 knockout mouse). *Am J Pathol* 159, 1477–1494. doi:10.1016/S0002-9440(10)62534-5.

Berger, J., Dorninger, F., Forss-Petter, S., and Kunze, M. (2016). Peroxisomes in brain development and function. *Biochimica et biophysica acta* 1863, 934–955. doi:10.1016/j.bbamcr.2015.12.005.

Berridge, M. J., Lipp, P., and Bootman, M. D. (2000). The versatility and universality of calcium signalling. *Nature Reviews Molecular Cell Biology* 1, 11–21. doi:10.1038/35036035.

Bers, D. M., and Perez-Reyes, E. (1999). Ca channels in cardiac myocytes: structure and function in Ca influx and intracellular Ca release. *Cardiovasc Res* 42, 339–360. doi:10.1016/s0008-6363(99)00038-3.

Betzig, E., Patterson, G. H., Sougrat, R., Lindwasser, O. W., Olenych, S., Bonifacino, J. S., et al. (2006). Imaging intracellular fluorescent proteins at nanometer resolution. *Science* 313, 1642–1645. doi:10.1126/science.1127344.

Bootman, M. D., Berridge, M. J., and Roderick, H. L. (2002). Calcium signalling: more messengers, more channels, more complexity. *Curr Biol* 12, R563-565. doi:10.1016/s0960-9822(02)01055-2.

Borchert, T., Hübscher, D., Guessoum, C. I., Lam, T.-D. D., Ghadri, J. R., Schellinger, I. N., et al. (2017). Catecholamine-Dependent β-Adrenergic Signaling in a Pluripotent Stem Cell Model of Takotsubo Cardiomyopathy. *J Am Coll Cardiol* 70, 975–991. doi:10.1016/j.jacc.2017.06.061.

Braverman, N. E., Raymond, G. V., Rizzo, W. B., Moser, A. B., Wilkinson, M. E., Stone, E. M., et al. (2016). Peroxisome biogenesis disorders in the Zellweger spectrum: An overview of current diagnosis, clinical manifestations, and treatment guidelines. *Mol Genet Metab* 117, 313–321. doi:10.1016/j.ymgme.2015.12.009.

Brown, D. A., Perry, J. B., Allen, M. E., Sabbah, H. N., Stauffer, B. L., Shaikh, S. R., et al. (2017). Mitochondrial function as a therapeutic target in heart failure. *Nat Rev Cardiol* 14, 238–250. doi:10.1038/nrcardio.2016.203.

Bryant, S. M., Kong, C. H. T., Watson, J. J., Gadeberg, H. C., Roth, D. M., Patel, H. H., et al. (2018). Caveolin-3 KO disrupts t-tubule structure and decreases t-tubular ICa density in mouse ventricular myocytes. *Am J Physiol Heart Circ Physiol* 315, H1101–H1111. doi:10.1152/ajpheart.00209.2018.

Buentzel, J., and Thoms, S. (2017). The Use of Glycosylation Tags as Reporters for Protein Entry into the Endoplasmic Reticulum in Yeast and Mammalian Cells. *Methods Mol Biol* 1595, 221–232. doi:10.1007/978-1-4939-6937-1_21.

Buentzel, J., Vilardi, F., Lotz-Havla, A., Gärtner, J., and Thoms, S. (2015). Conserved targeting information in mammalian and fungal peroxisomal tail-anchored proteins. *Sci Rep* 5, 17420. doi:10.1038/srep17420.

Cardoso-Moreira, M., Halbert, J., Valloton, D., Velten, B., Chen, C., Shao, Y., et al. (2019). Gene expression across mammalian organ development. *Nature* 571, 505–509. doi:10.1038/s41586-019-1338-5.

Casey, J. R., Grinstein, S., and Orlowski, J. (2010). Sensors and regulators of intracellular pH. *Nature Reviews Molecular Cell Biology* 11, 50–61. doi:10.1038/nrm2820.

Catteruccia, M., Sanna, T., Santorelli, F. M., Tessa, A., Di Giacopo, R., Sauchelli, D., et al. (2009). Rippling muscle disease and cardiomyopathy associated with a mutation in the CAV3 gene. *Neuromuscul Disord* 19, 779–783. doi:10.1016/j.nmd.2009.08.015.

Chapman, R. A. (1979). Excitation-contraction coupling in cardiac muscle. *Prog Biophys Mol Biol* 35, 1–52. doi:10.1016/0079-6107(80)90002-4.

Chornyi, S., IJlst, L., van Roermund, C. W. T., Wanders, R. J. A., and Waterham, H. R. (2021). Peroxisomal Metabolite and Cofactor Transport in Humans. *Front Cell Dev Biol* 8, 613892. doi:10.3389/fcell.2020.613892.

Clapham, D. E. (2007). Calcium signaling. *Cell* 131, 1047–1058. doi:10.1016/j.cell.2007.11.028.

Colasante, C., Chen, J., Ahlemeyer, B., and Baumgart-Vogt, E. (2015). Peroxisomes in cardiomyocytes and the peroxisome / peroxisome proliferator-activated receptor-loop. *Thromb Haemost* 113, 452–463. doi:10.1160/TH14-06-0497.

Corpas, F. J., and Barroso, J. B. (2018). Calmodulin antagonist affects peroxisomal functionality by disrupting both peroxisomal Ca2+ and protein import. *J Cell Sci* 131, jcs201467. doi:10.1242/jcs.201467.

Corpas, F. J., Barroso, J. B., Carreras, A., Quirós, M., León, A. M., Romero-Puertas, M. C., et al. (2004). Cellular and subcellular localization of endogenous nitric oxide in young and senescent pea plants. *Plant Physiol* 136, 2722–2733. doi:10.1104/pp.104.042812.

Costello, J. L., Castro, I. G., Hacker, C., Schrader, T. A., Metz, J., Zeuschner, D., et al. (2017a). ACBD5 and VAPB mediate membrane associations between peroxisomes and the ER. *The Journal of cell biology* 216, 331–342. doi:10.1083/jcb.201607055.

Costello, J. L., Castro, I. G., Schrader, T. A., Islinger, M., and Schrader, M. (2017b). Peroxisomal ACBD4 interacts with VAPB and promotes ER-peroxisome associations. *Cell cycle (Georgetown, Tex.)* 16, 1039–1045. doi:10.1080/15384101.2017.1314422.

Dammann, C., Ichida, A., Hong, B., Romanowsky, S. M., Hrabak, E. M., Harmon, A. C., et al. (2003). Subcellular targeting of nine calcium-dependent protein kinase isoforms from Arabidopsis. *Plant Physiol* 132, 1840–1848. doi:10.1104/pp.103.020008.

Darwisch, W., von Spangenberg, M., Lehmann, J., Singin, Ö., Deubert, G., Kühl, S., et al. (2020). Cerebellar and hepatic alterations in ACBD5-deficient mice are associated with unexpected, distinct alterations in cellular lipid homeostasis. *Commun Biol* 3, 713. doi:10.1038/s42003-020-01442-x.

De Stefani, D., Raffaello, A., Teardo, E., Szabò, I., and Rizzuto, R. (2011). A forty-kilodalton protein of the inner membrane is the mitochondrial calcium uniporter. *Nature* 476, 336–340. doi:10.1038/nature10230.

Drago, I., Giacomello, M., Pizzo, P., and Pozzan, T. (2008). Calcium dynamics in the peroxisomal lumen of living cells. *J Biol Chem* 283, 14384–14390. doi:10.1074/jbc.M800600200.

Duchen, M. R. (2000). Mitochondria and calcium: from cell signalling to cell death. *J Physiol* 529, 57–68. doi:10.1111/j.1469-7793.2000.00057.x.

Ebberink, M. S., Koster, J., Visser, G., Spronsen, F. van, Stolte-Dijkstra, I., Smit, G. P. A., et al. (2012). A novel defect of peroxisome division due to a homozygous non-sense mutation in the PEX11β gene. *J Med Genet* 49, 307–313. doi:10.1136/jmedgenet-2012-100778.

Ebberink, M. S., Mooijer, P. A. W., Gootjes, J., Koster, J., Wanders, R. J. A., and Waterham, H. R. (2011). Genetic classification and mutational spectrum of more than 600 patients with a Zellweger syndrome spectrum disorder. *Hum. Mutat.* 32, 59–69. doi:10.1002/humu.21388.

Farhana, A., and Lappin, S. L. (2021). “Biochemistry, Lactate Dehydrogenase,” in *StatPearls* (Treasure Island (FL): StatPearls Publishing). Available at: http://www.ncbi.nlm.nih.gov/books/NBK557536/ [Accessed May 12, 2021].

Ferdinandusse, S., Falkenberg, K. D., Koster, J., Mooyer, P. A., Jones, R., van Roermund, C. W. T., et al. (2017). ACBD5 deficiency causes a defect in peroxisomal very long-chain fatty acid metabolism. *Journal of medical genetics* 54, 330–337. doi:10.1136/jmedgenet-2016-104132.

Flucher, B. E., Andrews, S. B., and Daniels, M. P. (1994). Molecular organization of transverse tubule/sarcoplasmic reticulum junctions during development of

excitation-contraction coupling in skeletal muscle. *MBoC* 5, 1105–1118. doi:10.1091/mbc.5.10.1105.

Fransen, M., Brees, C., Baumgart, E., Vanhooren, J. C., Baes, M., Mannaerts, G. P., et al. (1995). Identification and characterization of the putative human peroxisomal C-terminal targeting signal import receptor. *J Biol Chem* 270, 7731–7736. doi:10.1074/jbc.270.13.7731.

Gibhardt, C. S., Zimmermann, K. M., Zhang, X., Belousov, V. V., and Bogeski, I. (2016). Imaging calcium and redox signals using genetically encoded fluorescent indicators. *Cell Calcium* 60, 55–64. doi:10.1016/j.ceca.2016.04.008.

Giorgi, C., Marchi, S., and Pinton, P. (2018). The machineries, regulation and cellular functions of mitochondrial calcium. *Nat Rev Mol Cell Biol* 19, 713–730. doi:10.1038/s41580-018-0052-8.

Godinho, L. F., and Schrader, M. (2017). Determination of Peroxisomal pH in Living Mammalian Cells Using pHRed. *Methods Mol Biol* 1595, 181–189. doi:10.1007/978-1-4939-6937-1_16.

Greotti, E., Wong, A., Pozzan, T., Pendin, D., and Pizzo, P. (2016). Characterization of the ER-Targeted Low Affinity Ca(2+) Probe D4ER. *Sensors (Basel)* 16. doi:10.3390/s16091419.

Grings, M., Tonin, A. M., Knebel, L. A., Zanatta, A., Moura, A. P., Filho, C. S. D., et al. (2012). Phytanic acid disturbs mitochondrial homeostasis in heart of young rats: a possible pathomechanism of cardiomyopathy in Refsum disease. *Mol Cell Biochem* 366, 335–343. doi:10.1007/s11010-012-1311-1.

Gronemeyer, T., Wiese, S., Ofman, R., Bunse, C., Pawlas, M., Hayen, H., et al. (2013). The proteome of human liver peroxisomes: identification of five new peroxisomal constituents by a label-free quantitative proteomics survey. *PLoS One* 8, e57395. doi:10.1371/journal.pone.0057395.

Guillén-Samander, A., Leonzino, M., Hanna, M. G., Tang, N., Shen, H., and De Camilli, P. (2021). VPS13D bridges the ER to mitochondria and peroxisomes via Miro. *J Cell Biol* 220. doi:10.1083/jcb.202010004.

Gwathmey, J. K., Hajjar, R. J., and Solaro, R. J. (1991). Contractile deactivation and uncoupling of crossbridges. Effects of 2,3-butanedione monoxime on mammalian myocardium. *Circ Res* 69, 1280–1292. doi:10.1161/01.res.69.5.1280.

Halestrap, A. P., and Wilson, M. C. (2012). The monocarboxylate transporter family—Role and regulation. *IUBMB Life* 64, 109–119. doi:10.1002/iub.572.

Hauck, B., Chen, L., and Xiao, W. (2003). Generation and characterization of chimeric recombinant AAV vectors. *Mol Ther* 7, 419–425. doi:10.1016/s1525-0016(03)00012-1.

Hell, S. W., and Wichmann, J. (1994). Breaking the diffraction resolution limit by stimulated emission: stimulated-emission-depletion fluorescence microscopy. *Opt Lett* 19, 780–782. doi:10.1364/ol.19.000780.

Hess, S. T., Girirajan, T. P. K., and Mason, M. D. (2006). Ultra-high resolution imaging by fluorescence photoactivation localization microscopy. *Biophys J* 91, 4258–4272. doi:10.1529/biophysj.106.091116.

Hicks, L., and Fahimi, H. D. (1977). Peroxisomes (microbodies) in the myocardium of rodents and primates. A comparative Ultrastructural cytochemical study. *Cell Tissue Res* 175, 467–481. doi:10.1007/BF00222413.

Hirabayashi, Y., Kwon, S.-K., Paek, H., Pernice, W. M., Paul, M. A., Lee, J., et al. (2017). ER-mitochondria tethering by PDZD8 regulates Ca2+ dynamics in mammalian neurons. *Science* 358, 623–630. doi:10.1126/science.aan6009.

Hoepfner, D., Schildknegt, D., Braakman, I., Philippsen, P., and Tabak, H. F. (2005). Contribution of the endoplasmic reticulum to peroxisome formation. *Cell* 122, 85–95. doi:10.1016/j.cell.2005.04.025.

Hua, R., Cheng, D., Coyaud, É., Freeman, S., Di Pietro, E., Wang, Y., et al. (2017). VAPs and ACBD5 tether peroxisomes to the ER for peroxisome maintenance and lipid homeostasis. *J Cell Biol* 216, 367–377. doi:10.1083/jcb.201608128.

Huang, B., Babcock, H., and Zhuang, X. (2010). Breaking the diffraction barrier: super-resolution imaging of cells. *Cell* 143, 1047–1058. doi:10.1016/j.cell.2010.12.002.

Huss, J. M., and Kelly, D. P. (2005). Mitochondrial energy metabolism in heart failure: a question of balance. *J Clin Invest* 115, 547–555. doi:10.1172/JCI24405.

Islinger, M., Cardoso, M. J. R., and Schrader, M. (2010). Be different--the diversity of peroxisomes in the animal kingdom. *Biochim Biophys Acta* 1803, 881–897. doi:10.1016/j.bbamcr.2010.03.013.

Islinger, M., Grille, S., Fahimi, H. D., and Schrader, M. (2012). The peroxisome: an update on mysteries. *Histochem Cell Biol* 137, 547–574. doi:10.1007/s00418-012-0941-4.

Ji, W.-K., Chakrabarti, R., Fan, X., Schoenfeld, L., Strack, S., and Higgs, H. N. (2017). Receptor-mediated Drp1 oligomerization on endoplasmic reticulum. *J Cell Biol* 216, 4123–4139. doi:10.1083/jcb.201610057.

Kaestner, L., Scholz, A., Tian, Q., Ruppenthal, S., Tabellion, W., Wiesen, K., et al. (2014). Genetically encoded Ca2+ indicators in cardiac myocytes. *Circ Res* 114, 1623–1639. doi:10.1161/CIRCRESAHA.114.303475.

Kamp, T. J., and Hell, J. W. (2000). Regulation of cardiac L-type calcium channels by protein kinase A and protein kinase C. *Circ Res* 87, 1095–1102. doi:10.1161/01.res.87.12.1095.

Karnati, S., and Baumgart-Vogt, E. (2008). Peroxisomes in mouse and human lung: their involvement in pulmonary lipid metabolism. *Histochem Cell Biol* 130, 719–740. doi:10.1007/s00418-008-0462-3.

Kim, J. J., Yang, L., Lin, B., Zhu, X., Sun, B., Kaplan, A. D., et al. (2015). Mechanism of automaticity in cardiomyocytes derived from human induced pluripotent stem cells. *J Mol Cell Cardiol* 81, 81–93. doi:10.1016/j.yjmcc.2015.01.013.

Kim, P. K., and Hettema, E. H. (2015). Multiple pathways for protein transport to peroxisomes. *Journal of molecular biology* 427, 1176–1190. doi:10.1016/j.jmb.2015.02.005.

Kim, P. K., Mullen, R. T., Schumann, U., and Lippincott-Schwartz, J. (2006). The origin and maintenance of mammalian peroxisomes involves a de novo PEX16-dependent pathway from the ER. *J Cell Biol* 173, 521–532. doi:10.1083/jcb.200601036.

Kimura, T., Ferran, B., Tsukahara, Y., Shang, Q., Desai, S., Fedoce, A., et al. (2019). Production of adeno-associated virus vectors for in vitro and in vivo applications. *Sci Rep* 9, 13601. doi:10.1038/s41598-019-49624-w.

Klar, T. A., and Hell, S. W. (1999). Subdiffraction resolution in far-field fluorescence microscopy. *Opt Lett* 24, 954–956. doi:10.1364/ol.24.000954.

Klosowiak, J. L., Focia, P. J., Chakravarthy, S., Landahl, E. C., Freymann, D. M., and Rice, S. E. (2013). Structural coupling of the EF hand and C-terminal GTPase domains in the mitochondrial protein Miro. *EMBO Rep* 14, 968–974. doi:10.1038/embor.2013.151.

Klouwer, F. C. C., Berendse, K., Ferdinandusse, S., Wanders, R. J. A., Engelen, M., and Poll-The, B. T. (2015). Zellweger spectrum disorders: clinical overview and management approach. *Orphanet J Rare Dis* 10, 151. doi:10.1186/s13023-015-0368-9.

Koch, J., Pranjic, K., Huber, A., Ellinger, A., Hartig, A., Kragler, F., et al. (2010). PEX11 family members are membrane elongation factors that coordinate peroxisome proliferation and maintenance. *J Cell Sci* 123, 3389–3400. doi:10.1242/jcs.064907.

Kohl, T., Westphal, V., Hell, S. W., and Lehnart, S. E. (2013). Superresolution microscopy in heart - cardiac nanoscopy. *J Mol Cell Cardiol* 58, 13–21. doi:10.1016/j.yjmcc.2012.11.016.

Koivumäki, J. T., Naumenko, N., Tuomainen, T., Takalo, J., Oksanen, M., Puttonen, K. A., et al. (2018). Structural Immaturity of Human iPSC-Derived Cardiomyocytes: In Silico Investigation of Effects on Function and Disease Modeling. *Front Physiol* 9, 80. doi:10.3389/fphys.2018.00080.

Kong, H., Jones, P. P., Koop, A., Zhang, L., Duff, H. J., and Chen, S. R. W. (2008). Caffeine induces Ca2+ release by reducing the threshold for luminal Ca2+ activation of the ryanodine receptor. *Biochem J* 414, 441–452. doi:10.1042/BJ20080489.

Lasorsa, F. M., Pinton, P., Palmieri, L., Scarcia, P., Rottensteiner, H., Rizzuto, R., et al. (2008). Peroxisomes as Novel Players in Cell Calcium Homeostasis. *J Biol Chem* 283, 15300–15308. doi:10.1074/jbc.M800648200.

Lian, X., Zhang, J., Azarin, S. M., Zhu, K., Hazeltine, L. B., Bao, X., et al. (2013). Directed cardiomyocyte differentiation from human pluripotent stem cells by modulating Wnt/β-catenin signaling under fully defined conditions. *Nature Protocols* 8, 162–175. doi:10.1038/nprot.2012.150.

Lismont, C., Koster, J., Provost, S., Baes, M., Van Veldhoven, P. P., Waterham, H. R., et al. (2019). Deciphering the potential involvement of PXMP2 and PEX11B in hydrogen peroxide permeation across the peroxisomal membrane reveals a role for PEX11B in protein sorting. *Biochimica et Biophysica Acta (BBA) - Biomembranes* 1861, 182991. doi:10.1016/j.bbamem.2019.05.013.

Liu, C., and Hermann, T. E. (1978). Characterization of ionomycin as a calcium ionophore. *J Biol Chem* 253, 5892–5894.

Liu, Y., and Zhu, X. (2017). Endoplasmic reticulum-mitochondria tethering in neurodegenerative diseases. *Transl Neurodegener* 6, 21. doi:10.1186/s40035-017-0092-6.

Loewen, C. J. R., Roy, A., and Levine, T. P. (2003). A conserved ER targeting motif in three families of lipid binding proteins and in Opi1p binds VAP. *EMBO J* 22, 2025–2035. doi:10.1093/emboj/cdg201.

Matsuda, T., Horikawa, K., Saito, K., and Nagai, T. (2013). Highlighted Ca 2+ imaging with a genetically encoded 'caged' indicator. *Sci Rep* 3, 1–4. doi:10.1038/srep01398.

Mayerhofer, P. U. (2016). Targeting and insertion of peroxisomal membrane proteins: ER trafficking versus direct delivery to peroxisomes. *Biochim Biophys Acta* 1863, 870–880. doi:10.1016/j.bbamcr.2015.09.021.

McClelland, G. B., Khanna, S., González, G. F., Butz, C. E., and Brooks, G. A. (2003). Peroxisomal membrane monocarboxylate transporters: evidence for a redox shuttle system? *Biochem Biophys Res Commun* 304, 130–135. doi:10.1016/s0006-291x(03)00550-3.

McCue, H. V., Wardyn, J. D., Burgoyne, R. D., and Haynes, L. P. (2013). Generation and characterization of a lysosomally targeted, genetically encoded Ca(2+)-sensor. *Biochem J* 449, 449–457. doi:10.1042/BJ20120898.

Mindthoff, S., Grunau, S., Steinfort, L. L., Girzalsky, W., Hiltunen, J. K., Erdmann, R., et al. (2016). Peroxisomal Pex11 is a pore-forming protein homologous to TRPM channels. *Biochim. Biophys. Acta* 1863, 271–283. doi:10.1016/j.bbamcr.2015.11.013.

Morgan, A. J., and Jacob, R. (1994). Ionomycin enhances Ca2+ influx by stimulating store-regulated cation entry and not by a direct action at the plasma membrane. *Biochem J* 300 (Pt 3), 665–672. doi:10.1042/bj3000665.

Müller, O. J., Leuchs, B., Pleger, S. T., Grimm, D., Franz, W.-M., Katus, H. A., et al. (2006). Improved cardiac gene transfer by transcriptional and transductional targeting of adeno-associated viral vectors. *Cardiovasc Res* 70, 70–78. doi:10.1016/j.cardiores.2005.12.017.

Muschol, M., Dasgupta, B. R., and Salzberg, B. M. (1999). Caffeine interaction with fluorescent calcium indicator dyes. *Biophys J* 77, 577–586. doi:10.1016/S0006-3495(99)76914-6.

Nagai, T., Sawano, A., Park, E. S., and Miyawaki, A. (2001). Circularly permuted green fluorescent proteins engineered to sense Ca2+. *Proc Natl Acad Sci U S A* 98, 3197–3202. doi:10.1073/pnas.051636098.

Nemani, N., Shanmughapriya, S., and Madesh, M. (2018). Molecular regulation of MCU: Implications in physiology and disease. *Cell Calcium* 74, 86–93. doi:10.1016/j.ceca.2018.06.006.

Palmer, A. E., Giacomello, M., Kortemme, T., Hires, S. A., Lev-Ram, V., Baker, D., et al. (2006). Ca2+ Indicators Based on Computationally Redesigned Calmodulin-Peptide Pairs. *Chemistry & Biology* 13, 521–530. doi:10.1016/j.chembiol.2006.03.007.

Palmer, A. E., Jin, C., Reed, J. C., and Tsien, R. Y. (2004). Bcl-2-mediated alterations in endoplasmic reticulum Ca2+ analyzed with an improved genetically encoded fluorescent sensor. *Proc Natl Acad Sci U S A* 101, 17404–17409. doi:10.1073/pnas.0408030101.

Palmer, A. E., and Tsien, R. Y. (2006). Measuring calcium signaling using genetically targetable fluorescent indicators. *Nat Protoc* 1, 1057–1065. doi:10.1038/nprot.2006.172.

Park, J. G., and Palmer, A. E. (2015). Measuring the in situ Kd of a genetically encoded Ca2+ sensor. *Cold Spring Harb Protoc* 2015, pdb.prot076554. doi:10.1101/pdb.prot076554.

Parton, R. G. (2018). Caveolae: Structure, Function, and Relationship to Disease. *Annu Rev Cell Dev Biol* 34, 111–136. doi:10.1146/annurev-cellbio-100617-062737.

Paupe, V., and Prudent, J. (2018). New insights into the role of mitochondrial calcium homeostasis in cell migration. *Biochem Biophys Res Commun* 500, 75–86. doi:10.1016/j.bbrc.2017.05.039.

Pedrazzini, E., Villa, A., Longhi, R., Bulbarelli, A., and Borgese, N. (2000). Mechanism of residence of cytochrome b(5), a tail-anchored protein, in the endoplasmic reticulum. *J Cell Biol* 148, 899–914. doi:10.1083/jcb.148.5.899.

Pérez Koldenkova, V., and Nagai, T. (2013). Genetically encoded Ca(2+) indicators: properties and evaluation. *Biochim Biophys Acta* 1833, 1787–1797. doi:10.1016/j.bbamcr.2013.01.011.

Petrungaro, C., Zimmermann, K. M., Küttner, V., Fischer, M., Dengjel, J., Bogeski, I., et al. (2015). The Ca(2+)-Dependent Release of the Mia40-Induced MICU1-MICU2 Dimer from MCU Regulates Mitochondrial Ca(2+) Uptake. *Cell Metab.* 22, 721–733. doi:10.1016/j.cmet.2015.08.019.

Phillips, M. J., and Voeltz, G. K. (2016). Structure and function of ER membrane contact sites with other organelles. *Nature Reviews Molecular Cell Biology* 17, 69. doi:10.1038/nrm.2015.8.

Platta, H. W., Brinkmeier, R., Reidick, C., Galiani, S., Clausen, M. P., and Eggeling, C. (2016). Regulation of peroxisomal matrix protein import by ubiquitination. *Biochimica et Biophysica Acta (BBA) - Molecular Cell Research* 1863, 838–849. doi:10.1016/j.bbamcr.2015.09.010.

Pozzan, T., and Rudolf, R. (2009). Measurements of mitochondrial calcium in vivo. *Biochim Biophys Acta* 1787, 1317–1323. doi:10.1016/j.bbabio.2008.11.012.

Primeau, J. O., Armanious, G. P., Fisher, M. E., and Young, H. S. (2018). The SarcoEndoplasmic Reticulum Calcium ATPase. *Subcell Biochem* 87, 229–258. doi:10.1007/978-981-10-7757-9_8.

Prondzynski, M., Lemoine, M. D., Zech, A. T., Horváth, A., Di Mauro, V., Koivumäki, J. T., et al. (2019). Disease modeling of a mutation in α-actinin 2 guides clinical therapy in hypertrophic cardiomyopathy. *EMBO Mol Med* 11, e11115. doi:10.15252/emmm.201911115.

Raffaello, A., Mammucari, C., Gherardi, G., and Rizzuto, R. (2016). Calcium at the Center of Cell Signaling: Interplay between Endoplasmic Reticulum, Mitochondria, and Lysosomes. *Trends Biochem Sci* 41, 1035–1049. doi:10.1016/j.tibs.2016.09.001.

Rapti, K., Stillitano, F., Karakikes, I., Nonnenmacher, M., Weber, T., Hulot, J.-S., et al. (2015). Effectiveness of gene delivery systems for pluripotent and differentiated cells. *Mol Ther Methods Clin Dev* 2, 14067. doi:10.1038/mtm.2014.67.

Reddy, J. K., and Hashimoto, T. (2001). Peroxisomal beta-oxidation and peroxisome proliferator-activated receptor alpha: an adaptive metabolic system. *Annu Rev Nutr* 21, 193–230. doi:10.1146/annurev.nutr.21.1.193.

Régal, L., Ebberink, M. S., Goemans, N., Wanders, R. J. A., De Meirleir, L., Jaeken, J., et al. (2010). Mutations in PEX10 are a cause of autosomal recessive ataxia. *Ann Neurol* 68, 259–263. doi:10.1002/ana.22035.

Rehling, P., Marzioch, M., Niesen, F., Wittke, E., Veenhuis, M., and Kunau, W. H. (1996). The import receptor for the peroxisomal targeting signal 2 (PTS2) in Saccharomyces cerevisiae is encoded by the PAS7 gene. *EMBO J* 15, 2901–2913.

Rokka, A., Antonenkov, V. D., Soininen, R., Immonen, H. L., Pirilä, P. L., Bergmann, U., et al. (2009). Pxmp2 is a channel-forming protein in Mammalian peroxisomal membrane. *PLoS ONE* 4, e5090. doi:10.1371/journal.pone.0005090.

Rust, M. J., Bates, M., and Zhuang, X. (2006). Sub-diffraction-limit imaging by stochastic optical reconstruction microscopy (STORM). *Nat Methods* 3, 793–795. doi:10.1038/nmeth929.

Sacksteder, K. A., Jones, J. M., South, S. T., Li, X., Liu, Y., and Gould, S. J. (2000). PEX19 binds multiple peroxisomal membrane proteins, is predominantly cytoplasmic, and is required for peroxisome membrane synthesis. *J Cell Biol* 148, 931–944. doi:10.1083/jcb.148.5.931.

Saka, S., and Rizzoli, S. O. (2012). Super-resolution imaging prompts re-thinking of cell biology mechanisms: selected cases using stimulated emission depletion microscopy. *Bioessays* 34, 386–395. doi:10.1002/bies.201100080.

Sandow, A. (1952). Excitation-contraction coupling in muscular response. *Yale J Biol Med* 25, 176–201.

Santos, M. J., Henderson, S. C., Moser, A. B., Moser, H. W., and Lazarow, P. B. (2000). Peroxisomal ghosts are intracellular structures distinct from lysosomal compartments in Zellweger syndrome: a confocal laser scanning microscopy study. *Biol Cell* 92, 85–94. doi:10.1016/s0248-4900(00)89016-4.

Santos, M. J., Imanaka, T., Shio, H., Small, G. M., and Lazarow, P. B. (1988). Peroxisomal membrane ghosts in Zellweger syndrome--aberrant organelle assembly. *Science* 239, 1536–1538. doi:10.1126/science.3281254.

Sargsyan, Y., Bickmeyer, U., Gibhardt, C. S., Streckfuss-Bömeke, K., Bogeski, I., and Thoms, S. (2021). Peroxisomes contribute to intracellular calcium dynamics in cardiomyocytes and non-excitable cells. *Life Sci Alliance* 4, e202000987. doi:10.26508/lsa.202000987.

Sargsyan, Y., and Thoms, S. (2020). Staying in Healthy Contact: How Peroxisomes Interact with Other Cell Organelles. *Trends Mol Med* 26, 201–214. doi:10.1016/j.molmed.2019.09.012.

Schermelleh, L., Ferrand, A., Huser, T., Eggeling, C., Sauer, M., Biehlmaier, O., et al. (2019). Super-resolution microscopy demystified. *Nat Cell Biol* 21, 72–84. doi:10.1038/s41556-018-0251-8.

Schindelin, J., Arganda-Carreras, I., Frise, E., Kaynig, V., Longair, M., Pietzsch, T., et al. (2012). Fiji: an open-source platform for biological-image analysis. *Nat Methods* 9, 676–682. doi:10.1038/nmeth.2019.

Schnitzbauer, J., Strauss, M. T., Schlichthaerle, T., Schueder, F., and Jungmann, R. (2017). Super-resolution microscopy with DNA-PAINT. *Nature Protocols* 12, 1198–1228. doi:10.1038/nprot.2017.024.

Schueren, F., Lingner, T., George, R., Hofhuis, J., Dickel, C., Gärtner, J., et al. (2014). Peroxisomal lactate dehydrogenase is generated by translational readthrough in mammals. *Elife* 3, e03640. doi:10.7554/eLife.03640.

Scorrano, L., De Matteis, M. A., Emr, S., Giordano, F., Hajnóczky, G., Kornmann, B., et al. (2019). Coming together to define membrane contact sites. *Nature Communications* 10, 1287. doi:10.1038/s41467-019-09253-3.

Sehgal, P., Szalai, P., Olesen, C., Praetorius, H. A., Nissen, P., Christensen, S. B., et al. (2017). Inhibition of the sarco/endoplasmic reticulum (ER) Ca2+-ATPase by thapsigargin analogs induces cell death via ER Ca2+ depletion and the unfolded protein response. *J Biol Chem* 292, 19656–19673. doi:10.1074/jbc.M117.796920.

Shimozawa, N., Zhang, Z., Imamura, A., Suzuki, Y., Fujiki, Y., Tsukamoto, T., et al. (2000). Molecular Mechanism of Detectable Catalase-Containing Particles, Peroxisomes, in Fibroblasts from a PEX2-Defective Patient. *Biochemical and Biophysical Research Communications* 268, 31–35. doi:10.1006/bbrc.1999.2082.

Smith, J. J., and Aitchison, J. D. (2013). Peroxisomes take shape. *Nat Rev Mol Cell Biol* 14, 803–817. doi:10.1038/nrm3700.

Soliman, K., Göttfert, F., Rosewich, H., Thoms, S., and Gärtner, J. (2018). Super-resolution imaging reveals the sub-diffraction phenotype of Zellweger Syndrome ghosts and wild-type peroxisomes. *Scientific Reports* 8, 7809. doi:10.1038/s41598-018-24119-2.

Steinberg, S. J., Dodt, G., Raymond, G. V., Braverman, N. E., Moser, A. B., and Moser, H. W. (2006). Peroxisome biogenesis disorders. *Biochim Biophys Acta* 1763, 1733–1748. doi:10.1016/j.bbamcr.2006.09.010.

Steinberg, S. J., Raymond, G. V., Braverman, N. E., and Moser, A. B. (1993). “Zellweger Spectrum Disorder,” in *GeneReviews®*, eds. M. P. Adam, H. H. Ardinger, R. A.

Pagon, S. E. Wallace, L. J. Bean, G. Mirzaa, et al. (Seattle (WA): University of Washington, Seattle). Available at: http://www.ncbi.nlm.nih.gov/books/NBK1448/ [Accessed April 26, 2021].

Suzuki, J., Kanemaru, K., Ishii, K., Ohkura, M., Okubo, Y., and Iino, M. (2014). Imaging intraorganellar Ca 2+ at subcellular resolution using CEPIA. *Nat Commun* 5, 1–13. doi:10.1038/ncomms5153.

Takahashi, K., Tanabe, K., Ohnuki, M., Narita, M., Ichisaka, T., Tomoda, K., et al. (2007). Induction of pluripotent stem cells from adult human fibroblasts by defined factors. *Cell* 131, 861–872. doi:10.1016/j.cell.2007.11.019.

Thomas, N. L., George, C. H., and Lai, F. A. (2006). Role of ryanodine receptor mutations in cardiac pathology: more questions than answers? *Biochem Soc Trans* 34, 913–918. doi:10.1042/BST0340913.

Thoms, S., and Erdmann, R. (2005). Dynamin-related proteins and Pex11 proteins in peroxisome division and proliferation. *FEBS J.* 272, 5169–5181. doi:10.1111/j.1742-4658.2005.04939.x.

Titorenko, V. I., and Rachubinski, R. A. (2001). Dynamics of peroxisome assembly and function. *Trends Cell Biol* 11, 22–29. doi:10.1016/s0962-8924(00)01865-1.

Tohyama, S., Hattori, F., Sano, M., Hishiki, T., Nagahata, Y., Matsuura, T., et al. (2013). Distinct metabolic flow enables large-scale purification of mouse and human pluripotent stem cell-derived cardiomyocytes. *Cell Stem Cell* 12, 127–137. doi:10.1016/j.stem.2012.09.013.

Torres, S. E., Gallagher, C. M., Plate, L., Gupta, M., Liem, C. R., Guo, X., et al. (2019). Ceapins block the unfolded protein response sensor ATF6α by inducing a neomorphic inter-organelle tether. *eLife* 8, e46595. doi:10.7554/eLife.46595.

Valm, A. M., Cohen, S., Legant, W. R., Melunis, J., Hershberg, U., Wait, E., et al. (2017). Applying systems-level spectral imaging and analysis to reveal the organelle interactome. *Nature* 546, 162–167. doi:10.1038/nature22369.

Van Petegem, F. (2012). Ryanodine receptors: structure and function. *J Biol Chem* 287, 31624–31632. doi:10.1074/jbc.R112.349068.

Vance, J. E. (2014). MAM (mitochondria-associated membranes) in mammalian cells: lipids and beyond. *Biochim Biophys Acta* 1841, 595–609. doi:10.1016/j.bbalip.2013.11.014.

Vapola, M. H., Rokka, A., Sormunen, R. T., Alhonen, L., Schmitz, W., Conzelmann, E., et al. (2014). Peroxisomal membrane channel Pxmp2 in the mammary fat pad is essential for stromal lipid homeostasis and for development of mammary gland epithelium in mice. *Dev Biol* 391, 66–80. doi:10.1016/j.ydbio.2014.03.022.

Vatta, M., Ackerman, M. J., Ye, B., Makielski, J. C., Ughanze, E. E., Taylor, E. W., et al. (2006). Mutant caveolin-3 induces persistent late sodium current and is associated with long-QT syndrome. *Circulation* 114, 2104–2112. doi:10.1161/CIRCULATIONAHA.106.635268.

Ventura-Clapier, R., Garnier, A., and Veksler, V. (2004). Energy metabolism in heart failure. *J Physiol* 555, 1–13. doi:10.1113/jphysiol.2003.055095.

Visser, W. F., van Roermund, C. W. T., Waterham, H. R., and Wanders, R. J. A. (2002). Identification of human PMP34 as a peroxisomal ATP transporter. *Biochem Biophys Res Commun* 299, 494–497. doi:10.1016/s0006-291x(02)02663-3.

Wagner, E., Lauterbach, M. A., Kohl, T., Westphal, V., Williams, G. S. B., Steinbrecher, J. H., et al. (2012). Stimulated emission depletion live-cell super-resolution imaging shows proliferative remodeling of T-tubule membrane structures after myocardial infarction. *Circ Res* 111, 402–414. doi:10.1161/CIRCRESAHA.112.274530.

Wanders, R. J. A., and Komen, J. C. (2007). Peroxisomes, Refsum's disease and the alpha- and omega-oxidation of phytanic acid. *Biochem Soc Trans* 35, 865–869. doi:10.1042/BST0350865.

Wanders, R. J. A., and Waterham, H. R. (2006). Biochemistry of mammalian peroxisomes revisited. *Annu Rev Biochem* 75, 295–332. doi:10.1146/annurev.biochem.74.082803.133329.

Wanders, R. J. A., Waterham, H. R., and Ferdinandusse, S. (2015). Metabolic Interplay between Peroxisomes and Other Subcellular Organelles Including Mitochondria and the Endoplasmic Reticulum. *Frontiers in cell and developmental biology* 3, 83. doi:10.3389/fcell.2015.00083.

Wang, H., Sheehan, R. P., Palmer, A. C., Everley, R. A., Boswell, S. A., Ron-Harel, N., et al. (2019). Adaptation of Human iPSC-Derived Cardiomyocytes to Tyrosine Kinase Inhibitors Reduces Acute Cardiotoxicity via Metabolic Reprogramming. *Cell Syst* 8, 412-426.e7. doi:10.1016/j.cels.2019.03.009.

Warren, D. S., Morrell, J. C., Moser, H. W., Valle, D., and Gould, S. J. (1998). Identification of PEX10, the gene defective in complementation group 7 of the peroxisome-biogenesis disorders. *Am J Hum Genet* 63, 347–359. doi:10.1086/301963.

Watanabe, T., and Suga, T. (1988). Suppression of clofibrate-induced peroxisome proliferation in rat liver by nicardipine, a calcium antagonist. *FEBS Lett* 232, 293–297. doi:10.1016/0014-5793(88)80756-7.

Waterham, H. R., Ferdinandusse, S., and Wanders, R. J. A. (2016). Human disorders of peroxisome metabolism and biogenesis. *Biochim Biophys Acta* 1863, 922–933. doi:10.1016/j.bbamcr.2015.11.015.

Weber, F. E., Minestrini, G., Dyer, J. H., Werder, M., Boffelli, D., Compassi, S., et al. (1997). Molecular cloning of a peroxisomal Ca2+-dependent member of the mitochondrial carrier superfamily. *Proc Natl Acad Sci U S A* 94, 8509–8514. doi:10.1073/pnas.94.16.8509.

Werfel, S., Jungmann, A., Lehmann, L., Ksienzyk, J., Bekeredjian, R., Kaya, Z., et al. (2014). Rapid and highly efficient inducible cardiac gene knockout in adult mice using AAV-mediated expression of Cre recombinase. *Cardiovasc Res* 104, 15–23. doi:10.1093/cvr/cvu174.

Whitaker, M. (2010). Genetically encoded probes for measurement of intracellular calcium. *Methods Cell Biol* 99, 153–182. doi:10.1016/B978-0-12-374841-6.00006-2.

Williams, G. S. B., Boyman, L., and Lederer, W. J. (2015). Mitochondrial calcium and the regulation of metabolism in the heart. *J Mol Cell Cardiol* 78, 35–45. doi:10.1016/j.yjmcc.2014.10.019.

Xiao, J., Luo, J., Hu, A., Xiao, T., Li, M., Kong, Z., et al. (2019). Cholesterol transport through the peroxisome-ER membrane contacts tethered by PI(4,5)P2 and extended synaptotagmins. *Sci China Life Sci*, 1–19. doi:10.1007/s11427-019-9569-9.

Yagita, Y., Shinohara, K., Abe, Y., Nakagawa, K., Al-Owain, M., Alkuraya, F. S., et al. (2017). Deficiency of a Retinal Dystrophy Protein, Acyl-CoA Binding Domain-containing 5 (ACBD5), Impairs Peroxisomal beta-Oxidation of Very-long-chain Fatty Acids. *The Journal of biological chemistry* 292, 691–705. doi:10.1074/jbc.M116.760090.

Yamashita, T., Mitsui, J., Shimozawa, N., Takashima, S., Umemura, H., Sato, K., et al. (2017). Ataxic form of autosomal recessive PEX10-related peroxisome biogenesis disorders with a novel compound heterozygous gene mutation and characteristic clinical phenotype. *J Neurol Sci* 375, 424–429. doi:10.1016/j.jns.2017.02.058.

Yang, T., and Poovaiah, B. W. (2002). Hydrogen peroxide homeostasis: Activation of plant catalase by calcium/calmodulin. *Proc Natl Acad Sci U S A* 99, 4097–4102. doi:10.1073/pnas.052564899.

Yoshida, Y., and Yamanaka, S. (2011). iPS cells: a source of cardiac regeneration. *J Mol Cell Cardiol* 50, 327–332. doi:10.1016/j.yjmcc.2010.10.026.

Young, B., Wightman, R., Blanvillain, R., Purcel, S. B., and Gallois, P. (2010). pH-sensitivity of YFP provides an intracellular indicator of programmed cell death. *Plant Methods* 6, 27. doi:10.1186/1746-4811-6-27.

Yu, J., Vodyanik, M. A., Smuga-Otto, K., Antosiewicz-Bourget, J., Frane, J. L., Tian, S., et al. (2007). Induced pluripotent stem cell lines derived from human somatic cells. *Science* 318, 1917–1920. doi:10.1126/science.1151526.

Zhang, G. Q., Wei, H., Lu, J., Wong, P., and Shim, W. (2013). Identification and characterization of calcium sparks in cardiomyocytes derived from human induced pluripotent stem cells. *PLoS One* 8, e55266. doi:10.1371/journal.pone.0055266.

Zhao, Y., Araki, S., Wu, J., Teramoto, T., Chang, Y.-F., Nakano, M., et al. (2011). An expanded palette of genetically encoded Ca^{2+} indicators. *Science* 333, 1888–1891. doi:10.1126/science.1208592.

Zhou, M.-T., Qin, Y., Li, M., Chen, C., Chen, X., Shu, H.-B., et al. (2015). Quantitative Proteomics Reveals the Roles of Peroxisome-associated Proteins in Antiviral Innate Immune Responses. *Mol Cell Proteomics* 14, 2535–2549. doi:10.1074/mcp.M115.048413.

Zuppinger, C., Gibbons, G., Dutta-Passecker, P., Segiser, A., Most, H., and Suter, T. M. (2017). Characterization of cytoskeleton features and maturation status of cultured human iPSC-derived cardiomyocytes. *Eur J Histochem* 61, 2763. doi:10.4081/ejh.2017.2763.

Acknowledgements

I am sincerely thankful to Prof. Dr. Sven Thoms for the opportunity to work on this interesting project, for his excellent supervision, encouragement and support throughout my PhD.

I would like to thank Prof. Jutta Gärtner for the chance to work in the department of pediatrics at UMG.

I thank the members of my thesis committee, PD Dr. Laura Zelarayan and Prof. Dr. Silvio Rizzoli for helpful ideas and support.

I would like to thank Prof. Dr. Katrin Streckfuß-Bömeke for the excellent collaboration and providing the hiPSC-CMs, and Prof. Dr. Ivan Bogeski for extensive collaboration. Further, I am thankful to Prof. Dr. Ronald Wanders, Prof. Dr. Hans Waterham and Prof. Dr. Markus Islinger for fruitful discussions and ACBD5 cell lines.

I thank Dr. Roman Tsukanov and Dr. Nazar Oleksiievets for productive collaboration and giving deep insights in the super resolution microscopy. I am especially grateful to Dr. Tsukanov for building the perfusion system for live-cell imaging.

I appreciate very much the help of Anna Grönke, Effrosyni Kapsali, Uta Bickmeyer and Juhi V.

My special thanks to all members of the pediatrics lab technicians, students, postdocs and other colleges for creating a pleasant and supporting atmosphere.

Further, I would like to thank my family and friends for their patience and support.

Last but not least, I would like to thank German Academic Exchange Service (DAAD) for the financial support. My work would not have been possible without DAAD.

Publications

Oleksiievets, N., Sargsyan, Y., Thiele, J. C., Mougios, N., Sograte-Idrissi, S., Nevskyi, O., Gregor, I., Opazo, F., Thoms, S., Enderlein, J., Tsukanov, R. (2022). Fluorescence lifetime DNA-PAINT for multiplexed super-resolution imaging of cells. *Commun Biol.* 5, 38. doi: 10.1038/s42003-021-02976-4

Sargsyan, Y., Bickmeyer, U., Gibhardt, C. S., Streckfuss-Bömeke, K., Bogeski, I., and Thoms, S. (2021). Peroxisomes contribute to intracellular calcium dynamics in cardiomyocytes and non-excitable cells. *Life Sci Alliance* 4, e202000987. doi:10.26508/lsa.202000987.

Schilff, M., Sargsyan, Y., Hofhuis, J., and Thoms, S. (2021). Stop Codon Context-Specific Induction of Translational Readthrough. *Biomolecules* 11, 1006. doi:10.3390/biom11071006.

Sargsyan, Y., and Thoms, S. (2020). Staying in Healthy Contact: How Peroxisomes Interact with Other Cell Organelles. *Trends Mol Med* 26, 201–214. doi:10.1016/j.molmed.2019.09.012.